TRAPPING LIGHT IN SYNTHETICALLY-DESIGNED NANOWIRE GEOMETRIC SUPERLATTICES

Seokhyoung Kim

A dissertation submitted to the faculty of the University of North Carolina at Chapel Hill in partial fulfillment of the requirements for the degree of Doctor of Philosophy in the Department of Chemistry.

Chapel Hill
2019

Approval by:

James F. Cahoon

Scott C. Warren

Joanna M. Atkin

Wei You

Yosuke Kanai

ABSTRACT

Seokhyoung Kim: Trapping Light in Synthetically-Designed Nanowire Geometric Superlattices
(Under the direction of James F. Cahoon)

Semiconductor nanowires (NWs) are ideal building blocks for constructing nanophotonic devices due to their strong interaction with light and ability to tune electromagnetic resonances through geometry. The NW diameter provides a subwavelength geometry that satisfies the Mie scattering conditions, and the extended axial dimension allows for lossless waveguiding as well as Fabry-Perot cavity oscillation for truncated NWs. In addition to the cylindrical geometry, modulation of permittivity along the NW axis is a key control parameter that gives rise to tailorable nanophotonic properties. Due to the subwavelength nature of NWs, permittivity modulation can be effectively achieved in single-crystalline nanowires by modulating diameter instead of altering the material. Diameter-modulated NWs, namely NW geometric superlattices (GSLs), therefore serve as a structural nanophotonic entity that exhibits unique interactions with light.

Here, we demonstrate synthesis of vertical epitaxial silicon NWs with complex morphologies via dopant-encoded vapor-liquid-solid (VLS) growth and chemical etching. Addition of a surface-stabilizer at higher temperature and partial pressure conditions is the key to growing epitaxial NWs that exhibit conformal and smooth etching both in acidic and basic etch solutions. We study optical properties of horizontally-oriented single NW GSLs under global plane wave illumination. NW GSLs support a unique coupling between a Mie resonance and a bound guided state (BGS) at a select wavelength determined by the pitch of the GSL. We demonstrate tunable, narrow-band guiding of light through Mie-BGS coupling for the first time in the NW geometry under normally incident light. Using NW GSLs with different geometric parameters, we then describe the formation of an optical bound state in the continuum (BIC) using numerical calculations and theoretical modeling. Accidental decoupling from radiation continua gives rise to bound states, to which the access is controlled by geometric tuning. We experimentally observe the presence of a BIC that manifests as a disappearance of a characteristic Fano resonance in scattering spectra. The findings shown in this work demonstrate precise control of light waves in confined NW geometries, which can enable high-quality-factor (high-Q) optical operations and advanced nanophotonic applications.

To my loving wife Jungmin. Thanks for being with me through this adventure.

ACKNOWLEDGEMENTS

First, and most of all, I would like to thank my family, especially my parents S.C. Kim, S.O. Shin and sister H.Y Kim, for their love and support they have given me throughout my life. I do still remember countless conversations I exchanged with my dad in my childhood walking out at night. That encouragement and inspiration from his words undoubtedly formed the rigid path to this end. All the accomplishments in this long journey were made possible on top of my mom's sacrificial care and support. Perhaps the startline of the graduate school that I stepped on was the shoulders of these two giants.

Words can't describe how thankful I am to my loving wife Jungmin. Throughout the journey she has sat with me, written and read, laughed and struggled, and finally gone through all the challenges together. My dissertation would have not been possible without her support and understanding. Her presence turned every moment of my life in Chapel Hill into pure joy. She is the best wife, a true friend, wonderful mom and, of course, great scholar. Our proudest and most precious production during the graduate school, baby Jane, made our lives much richer and memorable.

I also can't thank enough my doctoral advisor, Professor James. F. Cahoon, for his guidance and support throughout my dissertation research. He has not only taught me the sciences and research but more importantly shown me the qualities that I will have to have as a mature scientist in my future career. I will not forget the vision, ethic and attitude that I've learned from him as well as the amount of coffee beans he provided me for five years.

TABLE OF CONTENTS

LIST OF TABLES ix

LIST OF FIGURES x

LIST OF ABBREVIATIONS xii

1 INTRODUCTION 1

1.1 Semiconductor Nanomaterials 1

1.1.1 Semiconductor Properties 1

1.1.2 Size-dependent Nanomaterial Properties 2

1.1.3 Types of Nanomaterials 3

1.2 Semiconductor Nanowires 3

1.2.1 Nanowire Synthesis 3

1.2.2 Nanowire Superstructures 4

1.3 Nanowire Photonics 6

1.3.1 Scattering-Based Properties 6

1.3.1.1 Mie Scattering of Nanowires 6

1.3.1.2 Applications of Scattering-Based Properties 8

1.3.2 Waveguide-Based Properties 9

1.3.2.1 Dispersion Relation of Nanowires 9

1.3.2.2 Applications of Waveguide-Based Properties 9

1.3.3 NW photonic crystals and metamaterials 10

2 METHODS 12

2.1 NW Growth 12

2.1.1 Non-epitaxial NW Growth 12
2.1.2 Epitaxial NW Growth 13
2.2 NW Etching 13
2.3 Single-NW Spectroscopy 14
2.3.1 Laser Microscope Design 14
2.3.2 Extinction and Waveguide Emission Measurement 16
2.4 Electron Microscopy Analysis 18
2.5 Numerical Modeling 19
3 DESIGNING MORPHOLOGY IN EPITAXIAL SILICON NANOWIRES: THE ROLE OF GOLD, SURFACE CHEMISTRY AND PHOSPHORUS DOPING 20
3.1 Introduction 20
3.2 Results 22
3.2.1 Epitaxial Growth with HCl 22
3.2.2 P Dopant Transitions 24
3.2.3 Role of Surface Au 27
3.2.4 Role of HCl on NW growth 32
3.3 Discussion 34
3.3.1 Role of Surface Chemistry 34
3.4 Conclusion 38
4 MIE-COUPLED BOUND GUIDED STATES IN NANOWIRE GEOMETRIC SUPERLATTICES 40
4.1 Introduction 40
4.2 Results and Discussion 42
4.2.1 Mie-BGS coupling in a NW GSL 42
4.2.2 Tunable guiding in a GSL-WG NW 54
4.2.3 Sensing and switching with a GSL-WG NW 59
4.3 Conclusion 61
5 OPTICAL BOUND STATES IN THE CONTINUUM WITH NANOWIRE GEOMETRIC SUPERLATTICES 62

5.1 Introduction 62
5.2 Results and Discussion 64
5.2.1 Optical BICs in a NW GSL 64
5.2.2 TCMT analysis of BICs 66
5.2.3 Illumination and geometry dependence of BICs 69
5.2.4 Experimental verification of BICs 70
5.3 Conclusion 72
6 CONCLUSIONS 73
APPENDIX 1: MATLAB CODE FOR ANALYTICAL CALCULATION OF MIE SCATTERING OF A CYLINDRICAL NW 74
APPENDIX 2: MATLAB CODE FOR TEMPORAL COUPLED MODE THEORY 81
REFERENCES 84

LIST OF TABLES

2.1 List of optics used for the laser microscope 16

4.1 Parameters used in the TCMT for fitting Q_{sca} spectra in Figure 4.1c 48

4.2 Parameters used in the TCMT for fitting Q_{sca} spectra in Supplementary Figure S7 51

5.1 Parameters used in the TCMT for fitting Q_{sca} spectra in Figure 5.3 69

LIST OF FIGURES

1.1 VLS growth of Si NWs 3

1.2 Mie resonances of a 200 nm diameter NW 7

2.1 Laser microscope for polarization-resolved bright-field extinction measurements 14

2.2 Laser illumination geometries for polarization-resolved measurements on NWs 17

2.3 Extinction of single Au NR 18

3.1 Growth of epitaxial $\langle 111 \rangle$ Si NWs 23

3.2 Abrupt P dopant modulation in epitaxial $\langle 111 \rangle$ Si NWs 25

3.3 Fit of the EDS spectrum used to determine relative amounts of each element 26

3.4 Characterization of Au surface aggregation as a function of NW growth rate and P doping.... 28

3.5 Tilt-view SEM images of Vertical Si NW grown at a constant SiH_4 partial pressure with dopant modulation before and after etching in BHF 29

3.6 Effect of total reactor pressure on etching 30

3.7 Impeding KOH wet-chemical etching in intrinsic Si NWs through localized Au aggregation . 32

3.8 Influence of HCl and surface chlorination on NW growth rate, Au aggregation, and NW wet-chemical etching 33

3.9 Schematic illustration of surface passivation during VLS growth under various process conditions 35

3.10 Encoding complex morphology in vertical Si NWs 38

4.1 The geometry and coupled resonances of a NW GSL 42

4.2 Fourier selection of BGS by higher harmonics 44

4.3 Calculated Magnetic Field Profiles of a GSL with varying pitch 45

4.4 Disappearance of BGS coupling at long pitch values outside the Mie resonance envelope 46

4.5 Incident angle dependence of BGS coupling 47

4.6 Schematic plots of Mie-BGS coupling with and without γ_g. 48

4.7 Diameter dependence and spectral tunability of Mie-BGS coupling 49

4.8 Effect of modulation depth on bound character of the BGS 50

4.9 NW with length of nearly 1 mm with no variation in diameter 52
4.10 Experimental extinction spectra of NW GSLs 53
4.11 Effect of Gaussian beam width 54
4.12 Selective excitation of guided modes through a NW GSL 55
4.13 Experimental validation of tunable, narrow-band guiding by NW GSLs 57
4.14 Fabry-Perot cavity free spectral ranges in WGs of different lengths 59
4.15 Optical switching in a GSL-WG 60

5.1 Optical BICs in a NW GSL 64
5.2 Full EM field patterns of $m = 0$ and 1 BICs 65
5.3 Q_{sca} spectra from TCMT and from full wave simulations 68
5.4 Geometric dependence of Q-factor 69
5.5 Geometric conditions, frequency and wavelengths of $m = 1$ BICs with various e at a fixed $d = 200$ nm 70
5.6 Experimental extinction measurement of NW GSLs 71
5.7 Effect of absorption on Q-factors and fits to experimental spectra 72

LIST OF ABBREVIATIONS

0D	zero-dimensional
1D	one-dimensional
2D	two-dimensional
BHF	buffered hydrofluoric acid
BGS	bound guided state
BIC	bound state in the continuum
CVD	chemical vapor deposition
d	diameter
δ	etch depth
e	etch diameter
EDS	energy-dispersive x-ray spectroscopy
EIT	electromagnetically induced transparency
EM	electromagnetic
ENGRAVE	Encoded Nanowire GRowth and Appearance through VLS and Etching
FIB	focused ion beam
FP	Fabry-Perot
FSR	free spectral range
FWHM	full-width-at-half-maximum
GSL	geometric superlattice
IPA	isopropyl alcohol
λ	wavelength
LED	light-emitting diode
MMA	methyl methacrylate
MQM	multi-quantum well
n_{eff}	effective refractive index
NIR	near-infrared
NP	nanoparticle
NR	nanorod

NT	nanotube
NW	nanowire
p	pitch
PC	photonic crystal
PML	perfectly matched layer
PMMA	poly(methyl methacrylate)
Q	quality factor
QD	quantum dot
Q_{ext}	extinction efficiency
Q_{guided}	guided efficiency
Q_{sca}	scattering efficiency
r	nanowire radius
RIU	refractive index unit
σ_{phys}	physical cross-section
σ_{sca}	scattering cross-section
sccm	standard cubic centimeters per minute
SEM	scanning electron microscope
SL	superlattice
SOI	silicon-on-insulator
STEM	scanning transmission electron microscope
TCMT	temporal coupled-mode theory
TE	transverse electric
TEM	transmission electron microscope
TM	transverse magnetic
Vis-SWIR	visible-short wavelength infrared
VLS	vapor-liquid-solid
VS	vapor-solid
WG	waveguide
WZ	wurtzite

ZB	zincblende

INTRODUCTION

1.1 Semiconductor Nanomaterials

1.1.1 Semiconductor Properties

Semiconductors form the basis of modern electronic and information technologies, and their presence can be found in every part of daily life from portable devices in our pocket to global information networks surrounding us. The growth of the semiconductor industry occurred as a result of the ability to precisely tune their electronic materials properties. Crystalline semiconductors have electronic band structures based on the ordered arrangement of their constituent atoms that creates a bandgap, an energetic region between the conduction band minimum edge and the valence band maximum edge where electrons are forbidden to reside. A Fermi level is a chemical potential that describes the potential of the collection of electrons in a material, and electrical properties of a semiconductor are highly dependent on the position of the Fermi level relative to the band edges. The Fermi level can be modified through chemical processes such as incorporation of impurity atoms, formation of vacancies in the crystal lattice, and application of an external bias. Doping controllably modifies the Fermi level, and precise control of doping is central to the design of microelectronic devices. For the most common semiconducting material, silicon (Si), electron-rich group V elements such as phosphorus (P) and arsenic (As) raise the Fermi level as they can donate excess electrons into the conduction band, whereas electron-deficient group III elements such as boron (B) and aluminum (Al) lower the Fermi level by accepting electrons and generating holes in the valence band. The doping processes that raise and lower the Fermi level convert an intrinsic semiconductor into an *n*-type and *p*-type, respectively.

Under illumination, semiconductors can absorb photons possessing energy exceeding the energy of their bandgap. When the light is absorbed, electrons in the valence band are excited to the conduction band and leave holes behind in the valence band. The photoexcited electron-hole pairs will eventually recombine and re-emit photons if done through radiative recombination pathways; however, when the electrons and holes are separated and collected at opposite electrodes, a photocurrent is generated with a photovoltage defined by the

potential difference between the two electrodes. This process is fundamental to the operation of photovoltaic solar cells, and the reverse process is responsible for light-emitting devices such as light-emitting diodes (LEDs).

Photons with energy lower than the bandgap can travel through the bulk of a semiconductor, and the behavior of light inside the material is dictated by the dielectric properties of the semiconductor. Many crystalline semiconductor materials exhibit static relative dielectric constants (ε_r) substantially higher than that of air ($\varepsilon_{r,air}$ = $\sim$1), including Si ($\varepsilon_{r,Si}$ = $\sim$11.6), Ge ($\varepsilon_{r,Ge}$ = $\sim$16) and GaAs ($\varepsilon_{r,GaAs}$ = $\sim$12.9).[1] When cladded with lower-dielectric materials such as SiO_2 (ε_{r,SiO_2} = $\sim$3.9), these materials can guide light waves with no major loss by total internal reflection through which typical optical fibers transmit information in optical communications. The rapid growth of microphotonics was made possible by patterning microscale waveguides on transparent substrates, namely in the silicon-on-insulator (SOI) configuration. In recent years, the size of device components has been further reduced to the nanoscale for a higher integration density of microelectronic and microphotonic devices. When the size of device components becomes comparable to the wavelength of light, however, the behavior of light in the material starts to follow that of waves rather than rays, which necessitates a fundamentally different understanding of wave interactions with nanoscale objects.

1.1.2 Size-dependent Nanomaterial Properties

When the size of a semiconductor is reduced to the nanometer scale, its properties are no longer dictated by the bulk properties. Quantum confinement, which widens the bandgap and discretizes the energy levels as the size of a semiconductor particle decreases, is one of the well-known examples of such an effect. As a result, quantum confinement drastically alters the light absorbing properties of a semiconductor in a geometry-dependent manner. Quantum dots (QDs) are nanocrystals smaller than $\sim$10 nm, and exhibit very bright luminescence with an emission color tunable throughout the visible[2] and near-infrared (NIR)[3,4] spectra. In certain occasions, quantum confinement can also induce an indirect-to-direct transition of a bandgap. For example, despite its dominant position in the semiconductor industry, Si has not been favored in the light-emitting industry due to its bandgap being indirect. Quantum confinement provides a route to circumvent this problem, because when the size of Si nanostructure decreases below $\sim$5 nm, its band alignment starts to become direct with the bandgap increasing in magnitude.[5]

Similarly, a constricted size of a nanomaterial gives rise to resonant interactions with light waves. When the size of a spherical nanoparticle (NP) approaches the wavelength of the visible light (400-700 nm), light

waves can circulate inside the NP for a finite lifetime and radiates back out into the free space, resulting in strong scattering phenomena. This behavior is well-explained by Mie scattering theory,[6] and optical resonant scattering of small particles is often called Mie scattering or a Mie resonance. At resonance, due to the prolonged lifetime of light waves inside the semiconductor nanostructure, the probability of light absorption increases and therefore the photovoltaic efficiency can be improved. Mie scattering is discussed in detail in section 1.3.1.1.

1.1.3 Types of Nanomaterials

Nanomaterials are commonly classified by their geometric dimensions. Spherical NPs and QDs are considered to be zero-dimensional (0D), and 0D NPs exhibit isotropic confinement properties due to the spherical symmetry. One-dimensional (1D) nanomaterials refer to structures extended in one dimension and confined in the other two dimensions, as is the case for nanowires (NWs) and nanotubes (NTs). Lastly, two-dimensional (2D) nanomaterials exhibit an extended, planar structure with an out-of-plane confinement typically within mono- to few-atomic-layer-thick thicknesses. Unlike 0D NPs, 1D and 2D nanomaterials exhibit both confined and bulk properties because they have both confined and extended dimensions.

1.2 Semiconductor Nanowires

1.2.1 Nanowire Synthesis

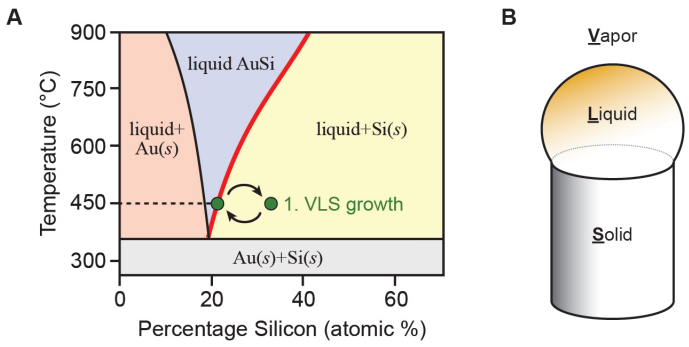

Figure 1.1: VLS growth of Si NWs. (A) Au-Si Eutectic Diagram. (B) Phase of Si atoms during VLS growth

Since first developed by Wagner and Ellis[7] at Bell Laboratory in 1964, vapor-liquid-solid (VLS) growth has been one of the most popular and efficient methods of synthesizing semiconductor NWs. For the Au-Si

system, the VLS mechanism operates based on a eutectic behavior of a semiconductor and a catalyst material. Figure 1.1 shows an exemplary eutectic diagram of Au and Si eutectic composition. A Au NP serves as a catalytic nanoreactor, and when Si is supplied from the vapor-phase precursor (SiH_4 or Si_2H_6) into the Au NP at an elevated temperature above the eutectic isotherm, the Au NP forms a liquid alloy with Si at a Si content of around 20 at.%. The NW growth occurs near the liquidus line (red curve in Figure 1) between the liquid alloy region and the region where liquid alloy and solid Si coexist. At equilibrium, the liquid alloy is stable with a composition between the liquidus lines at the reaction temperature. Upon continued supply of Si atoms, the composition departs the liquidus line to the right into the yellow-shaded region, causing a supersaturation and consequent precipitation of Si in the solid phase. As the reaction continues, a single-crystalline Si NW is produced at the catalyst-Si interface with a circular cross-section determined by the spherical shape of the catalyst. The name of the growth mechanism, VLS, thus describes the movement of Si atoms from the vapor-phase precursor to the liquid alloy catalyst and finally to the solid NW. The VLS process is not limited to the Au-Si binary system, but can be applied to any catalyst-semiconductor eutectic systems or self-catalyzed systems with a low melting point constituent. Si NWs have been synthesized using other metal catalysts[8] such as Ag, Al, Zn, and Pd. Other than group IV materials, III-V materials such as GaAs[9] and InP[10] as well as layered semiconductors such as PbI_2[11] can also be made into the NW geometry by VLS growth.

1.2.2 Nanowire Superstructures

For many technological applications, it is important to form heterostructures, modulate compositions, or spatially localize defect regions in semiconductor NWs at the desired position and length scales.[12,13] Development of synthetic techniques has allowed NWs to diversify their geometries and compositional profiles from a simple, uniform cylindrical shape. For example, sequential deposition of intrinsic and *n*-type shells through vapor-solid deposition over a *p*-type Si NW core produces coaxial *p-i-n* Si NWs that can harvest solar energy.[14,15] For III-V NWs, their electronic properties are highly sensitive to the local variation of the ratio of group III or V elements such as in GaN/InGaN,[16] or in GaAs/AlGaAs/InGaAs[17] systems. Using this effect, when multiple shells with different combinations of group III elements are grown in a single-nanometer length scale, quantum-confined multi quantum well (MQW) NWs exhibit tunable lasing action in the visible[16] and NIR[17] wavelength regime.

Axial NW heterostructures can be synthesized by *in-situ* control of the growth environment during NW growth. Abrupt switching of the vapor-phase precursor materials is the most common way of creating chemical heterostructures. This method can entirely change the semiconductor material when the precursor material is abruptly altered, as demonstrated in Si-Ge heterojunctions with few-atomic-layer-thick transition widths formed by completely replacing a Si precursor with a Ge precursor (GeH_4 or Ge_2H_6).[18,19] For binary or ternary III-V NWs, an atomically sharp transition can be achieved if the precursor for either group III or V element is only altered with the rest unchanged. The transition junction between InAs and GaAs made by this method therefore is just one atomic layer of As shared by the two materials.[20] Moreover, precise control of the switching frequency can produce MQW structures in the axial geometry. Rapid modulation of a Sb precursor flux during the VLS growth of GaAs NW produced GaAs/GaAsSb NW MQW superlattices (SLs), which showed tunable lasing properties.[21] It is also possible to modulate the concentration of dopant impurities while preserving the main semiconductor material. Modulating dopant precursors, PH_3 for *n*-type[22] and B_2H_6 for *p*-type[23] doping, during Si NW growth produces single-crystalline NWs with an alternating doping profile.

Besides chemical compositions, crystal phases of NWs can also be tuned by introducing impurities in III-V NWs. InP, which typically exhibits a wurtzite (WZ) crystal structure, can crystallize into zinc-blende (ZB) crystal phase upon introduction of zinc impurities. Therefore, modulation of a diethylzinc flow during the InP NW growth produces NW twinning SLs in which WZ and ZB crystal phases alternate.[24] Similar types of NW twinning SLs are demonstrated with other III-V materials such as GaP[25] and GaAs.[26]

Diameter modulation is an important tool for controlling optical properties of NWs because optical scattering and waveguide properties of NWs are highly sensitive to the diameter. Modulation of NW diameter has been demonstrated by a variety of means. Musin et al.[27,28] created Ge NWs with a tear-drop morphology by passivating the sidewall of NWs with tetramethyltin (TMT)[27] or trimethylsilane (TMSH)[28] during the growth and thus controlling the rate of vapor-solid deposition of Ge on the sidewall. A much finer geometric resolution in diameter modulation has been demonstrated in Si NWs utilizing the dopant-dependent etch rate of Si. Through their process named ENGRAVE (Encoded Nanowire Growth and Appearance through VLS and Etching), Christesen et al.[22] grew Si NWs encoded with pre-designed dopant profiles and realized NW geometric superlattices (GSLs) with sub-10 nm structural resolution through post-growth wet-chemical etching. Since the etch rate of Si monotonically increases and decreases with doping level in acidic and basic etch solution,[29] respectively, any arbitrary morphology with axial rotational symmetry could

be realized. Continued effort on optimizing the process for epitaxial NWs will be presented in Chapter 3. NW heterostructures with a periodic three-dimensional morphology have also been demonstrated via Plateau-Rayleigh crystal growth. Day et al.[30] deposited a Si shell over a Ge NW core with select growth parameters that unexpectedly induced instability of shells and resulted in breaking of a Si shell into regularly-spaced nanocrystals.

1.3 Nanowire Photonics

1.3.1 Scattering-Based Properties

1.3.1.1 Mie Scattering of Nanowires

Semiconductor NWs are an ideal building block for advanced nanophotonic applications as they interact strongly with light through electromagnetic resonances that are also referred to as optical states or modes.[31] Scattering of NWs is well described by Mie scattering theory,[6] and scattering efficiencies (Q_{sca}) under transverse-magnetic (TM) and transverse-electric (TE) polarized illumination are given by

$$Q_{\text{sca,I}}{}^{(\text{TM})} = \frac{2}{kr}\left[\mid b_{0\text{I}} \mid^2 + 2\sum_{m=1}^{\infty} \left(\mid a_{m\text{I}} \mid^2 + \mid b_{m\text{I}} \mid^2 \right) \right] \tag{1.1}$$

and

$$Q_{\text{sca,II}}{}^{(\text{TE})} = \frac{2}{kr}\left[\mid a_{0\text{II}} \mid^2 + 2\sum_{m=1}^{\infty} \left(\mid a_{m\text{II}} \mid^2 + \mid b_{m\text{II}} \mid^2 \right) \right] \tag{1.2}$$

where k is a wavevector, r is a NW radius, a_m and b_m are mth-order electric and magnetic Mie scattering coefficients, and subscripts I and II represent TM and TE polarizations, respectively. From these equations, Q_{sca} under unpolarized plane wave illumination is given by

$$Q_{\text{sca}}{}^{(\text{unpol})} = \frac{1}{2}\left(Q_{\text{sca,I}}{}^{(\text{TM})} + Q_{\text{sca,II}}{}^{(\text{TE})}\right). \tag{1.3}$$

Because NWs can attract light waves from a free-space area larger than their projected area, NWs frequently exhibit a scattering cross-section (σ_{sca}) much larger than the physical cross-section (σ_{phys}). This effect is known as an antenna effect and gives rise to Q_{sca}(=$\sigma_{sca}/\sigma_{phys}$) that can be larger than ten.[32]

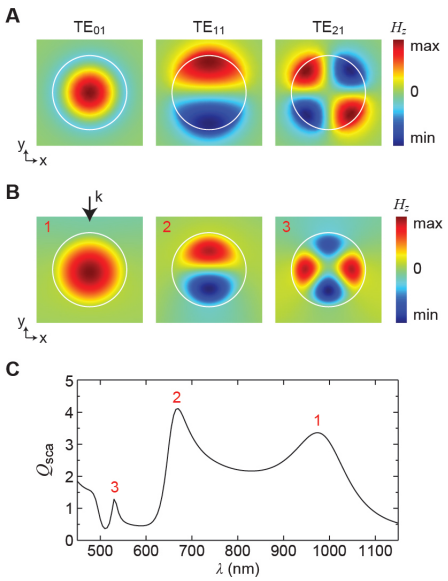

Figure 1.2: Mie resonances of a 200 nm diameter NW. (A-B) Magnetic field patterns of lowest TE Mie resonances in a 200 nm diameter NW calculated by eigenmode calculation (A) and scattering calculation under plane wave illumination (B). White circles represent the NW/air interface. (C) Q_{sca} of a 200 nm diameter NW. Peak labels are used to assign modes in panel (B).

Mie scattering occurs in a number of different fashion depending on the angular number m, and these scattering modes are often referred to as Mie resonances. Under normally-incident TE-polarized illumination, the nomenclature for Mie resonances typically takes the form of TE_{ml} (or TM_{ml} for TM polarization), where m refers to the half-number of maxima of the longitudinally-oriented field (magnetic for TE; electric for TM) along the azimuthal direction and l is the number of field maxima counted in the radial direction from the center of the NW. Figure 1.2A shows examples of eigenstates of three lowest-order TE-polarized Mie resonances. Figure 1.2B and C show field patterns of Mie resonances excited under a plane wave and a corresponding Q_{sca} spectrum, respectively. The symmetry of each mode is slightly deformed due to the directional excitation, but they show that modes can be identified by the same naming criteria. Naming applies to TM-polarized cases in the same way with electric and magnetic components replaced with each other.

1.3.1.2 Applications of Scattering-Based Properties

The precise synthetic control of NW diameter has allowed experimental validation of tunable scattering characteristics.[33,34] Diameter dependence of scattering enables a NW to exhibit a rainbow spectrum when a proper diameter profile is encoded,[35] and it can be used to turn NWs into individual pixels for structural color printing when fabricated in a macroscopic arrays.[36] The length of a NW serves as another geometric parameter for scattering of low-aspect-ratio NWs or nanorods (NRs). The Mie resonance of NRs rapidly shifts with length for small aspect ratios below $\sim$10, but it gradually asymptotes as the aspect ratio becomes larger.[37] Scattering properties of NWs can also be tuned by external environmental controls. For example, the resonant color of a NW shifts with a change in the refractive index of its surrounding medium, and the presence of a reflective substrate in a close proximity can affect the Mie resonance.[38] When placed below a NW, a metasurface mirror can control Mie resonance by shifting a local reflection phase.[39] Optical coupling between two NWs also causes a change of scattering properties, for which the inter-NW spacing plays an important role.[40]

Optical confinement in a NW can be drastically suppressed or enhanced by the presence of metallic shells. The former case has been studied in the context of making NWs invisible at select wavelengths. When a Si NW is coated with Au shell, for example, the scattering efficiency drops nearly two orders of magnitude under TM-polarized incidence. The suppression of scattering occurs at a wavelength where the electric response in the Si core and the Au shell are directed in the opposite direction and therefore cancelled.[41] The same principle turns a Ag-coated ZnO NW into a color filter when configured in a transmissive geometry.[42] When a NW core is removed after being coated with a shell of alternating TiO_2 and Ag, the hollow NT becomes completely invisible under even unpolarized light because the effective permittivity becomes near zero for both TE and TM polarizations.[43]

On the other hand, interfacing a semiconductor NW with a noble metal often creates a plasmonic nanocavity that exhibits enhanced optical interactions. When a thin shell of Ag covers a CdS NW, a whispering-gallery plasmon cavity forms at the interface and enhances the radiative decay rate by over three orders of magnitudes.[44] For silicon, a notoriously inefficient indirect bandgap material for light emission, the plasmon cavity formed with a Ag shell allows for much enhanced light emission with an internal quantum efficiency $>1\%$.[45] Plasmonic cavity-enhanced light emission has also been studied in the electroluminescent

configuration. When charge carriers are injected into a *p-n* junction of a Si NW coated with a Ag shell, the Purcell enhancement of up to 500% can be observed.[46]

1.3.2 Waveguide-Based Properties

1.3.2.1 Dispersion Relation of Nanowires

NWs can guide light waves along their axial dimension, and an angular quantum number (m) and polarization state distinguishes different guided modes from one another. Guided modes in a NW follow the dispersion relation[47–49]:

$$\left(\frac{1}{k_c^2}-\frac{1}{k^2}\right)^2\left(\frac{\beta m}{r}\right)^2 = k_0^2\left(n^2\frac{J_m^{'}(k_c r)}{k_c J_m(k_c r)}-n_0^2\frac{H_m^{'}(kr)}{kH_m(kr)}\right)\times\left(\frac{J_m^{'}(k_c r)}{k_c J_m(k_c r)}-\frac{H_m^{'}(kr)}{kH_m(kr)}\right) \quad (1.4)$$

where k_c and k are the transverse wavevectors inside and outside the cylinder, β and k_0 are the axial wavevectors inside and outside the cylinder, r is the radius of the cylinder, n and n_0 are the refractive indices of the cylinder and the surrounding medium, and J_m and H_m are the mth-order Bessel and Hankel functions of the first kind, respectively. For normal incidence where β is zero, Eq. 1.4 can be decoupled into purely TM and TE modes by setting the first and second term on the right-hand side at zero, respectively. The solutions of these static (β = 0) states agree with Mie resonances under normal illumination described in chapter 1.3.1.1. For propagating guided modes with non-zero β, modes with m higher than zero are hybrid-polarized electromagnetic (EM) modes, and the nomenclature follows EH_{ml} or HE_{ml}. An EH mode is more TE-like with a magnetic component partially oriented axially, and an HE mode is more TM-like with an electric field partially oriented axially. Careful comparison between theories (Eqs. 1.1 through 1.4) and full-wave simulations has revealed the relationship and transition between leaky Mie resonances and hybrid guided modes as a function of wavevector.[48,49]

1.3.2.2 Applications of Waveguide-Based Properties

Guided modes of NWs have been actively investigated in a variety of settings. Single-crystalline NWs with clean surfaces can guide light without a major scattering loss,[50] and guiding though a mild curvature with a radius of curvature larger than 2 μm still shows a minimal loss.[51] When the end facets are sufficiently reflective, guided modes can oscillate between the ends, which turns a NW into a Fabry-Perot (FP) cavity.

The FP oscillation in a NW manifests as regularly spaced sharp peaks over a broad envelop in scattering or emission spectra with a free spectral range determined by the length of the cavity.[52]

NWs made with high-gain media such as III-V materials can exhibit lasing based on the FP oscillation. GaAs NWs with GaAsSb quantum wells placed along the NW axis showed tunable lasing by controlling the atomic percentage of Sb in the quantum wells.[21] Recently, organic-inorganic hybrid perovskite materials have gained a high popularity because of the superior optoelectronic properties and the ease of preparation. Perovskite NWs have been synthesized by a variety of methods in the solution[53–55] and vapor phase,[56,57] and they exhibit low-threshold lasing with the peak wavelength tunable through control of the halide composition.[54–56]

Because the light waves propagating through a NW may carry optical information, there is a great potential for NWs to perform more complex functions such as all-optical data processing. A set of two NWs in a branched geometry can act as a basic logic element through the interference between guided beams in each NW branch,[58] which when configured in a four-terminal network can form a cascaded NOR gate.[59] Similarly, when two NWs are placed in series with a small gap about 5 nm, the emission from one NW can be injected to the other NW through the gap and be delivered to the other far end as a signal. The signal transmission can be significantly reduced by illuminating the second NW with a laser beam because of increased scattering of exciton-polaritons, and removing the laser beam restores the signal transmission, creating an optical switch.[60] All-optical NAND gate operation is achieved by integrating multiple of such NW optical switches.

1.3.3 NW photonic crystals and metamaterials

As described in chapter 1.2.2, diameter modulation in NWs has attracted attention because of the size dependence of optical properties. In particular, When a NW has a periodically alternating permittivity (or refractive index) along the axis, the modulated NW behaves like a photonic crystal (PC) with one-dimensional periodicity and lateral confinement. Permittivity is generally a materials property and therefore a permittivity modulation requires an alteration of materials. The simplest example includes an array of holes in PC slabs, where the slab material and air provides two permittivity domains. Modulation of permittivity in NWs can be achieved by a variety of means, and due to the sub-wavelength nature of NWs, only a small change in diameter can bring a sufficient shift of effective permittivity, eliminates the need of actually changing the material in a NW. For example, Fu et al.[61] demonstrated a distributed Bragg reflector in a GaN NW by

removing short NW sections with a regular spacing via focused ion-beam (FIB) milling. A stopband with an 8 nm width is experimentally observed at ∼450 nm from a NW grating 143 nm in pitch, and the spectral position of the stopband redshifted with an increasing pitch.

Similarly but quite distinctively, periodic diameter modulation also converts a NW into a one-dimensional metamaterial. While PCs and metamaterials seemingly share many similarities, the origins and characteristics of the effects are quite different. In the aspect of sizes, PCs have periodicity comparable to the wavelength of light whereas metamaterials operate either in a much smaller or larger size scale.[62] In addition, the fundamental physics that makes PCs attractive is the photonic bandgap, which can reject or confine specific wavelengths upon proper design. Meanwhile, metamaterials exhibit unique coupling effects between optical modes by breaking the symmetry of the system, enabling detection of otherwise dark or forbidden modes. Chapter 4 will discuss work to turn a NW GSL into a one-dimensional metamaterial by breaking an infinite translational symmetry with a periodic diameter modulation.

There is still a continuing effort for creating NW-based high-quality-factor (high-Q) cavities from both PC and metamaterial perspectives. Theoretical studies have reported the design principles for a plasmon-coupled NW PC cavity[63] and bound states in the continuum in the NW geometry.[64] Although predicted Q-factors of NW cavities are yet too low compared to lithographically-prepared nanobeams,[65,66] NWs hold a promise for high-Q cavities and for advanced nanophotonic applications due to their ability to possess much more complex chemical and structural symmetries than what is possible by lithographic methods. The works herein will introduce efforts toward realizing photonic NW GSLs from the synthetic aspect to physical interpretation and experimental characterization.

METHODS

2.1 NW Growth

Si NWs were grown in a home-built, hot-wall chemical vapor deposition system with silane (SiH_4; Voltaix), phosphine (PH_3; diluted to 1000 ppm in H_2, Voltaix), diborane (B_2H_6; 1000 ppm in H_2, Voltaix), hydrogen chloride (HCl anhydrous; Matheson TriGas; 5 N research purity grade), hydrogen (H_2; Matheson TriGas; 5 N semiconductor grade) in a 1-inch quartz-tube furnace (Lindberg Blue M). A vacuum system with a base pressure of $\sim 3 \times 10^{-3}$ torr was established by a dry screw pump (SDE120TX-45; Kashiyama), and the total reaction pressure was controlled by a 148J needle valve (MKS Instrument) for above 20 torr or by an automated butterfly valve (253B-1-40-1; MKS Instrument) for below 20 torr. Au NPs (Ted-Pella, 150-200 nm; or Sigma-Aldrich, 250-400 nm) of various diameters were used as NW growth catalysts.

2.1.1 Non-epitaxial NW Growth

A 380 μm-thick Si (100) wafer with 600 nm thermal oxide (University Wafer) was used as growth substrate for non-epitaxial NW growths. The wafer was cut into a size of $\sim$ 2 cm $\times$ 1 cm, sonicated in acetone, rinsed sequentially with acetone and isopropyl alcohol (IPA), and dried with nitrogen. These substrates were placed in a UV/O_3 cleaner (Samco UV-1) and treated at 150 °C for 5 minutes. The surface of the substrates were functionalized with poly-L-lysine (Sigma-Aldrich, 0.1% w/v in water, further diluted 66.7%) for 5 minutes, rinsed with nanopure water (Barnstead Nanopure; 10 $M\Omega \cdot$cm) and dried with nitrogen. The substrates were then covered by Au NPs (diluted 33.3% in water) for 5 minutes, rinsed with IPA, dried with nitrogen, and treated by UV/O_3 for 5 minutes.

All NWs were nucleated at 480 °C with 2.00 standard cubic centimeter per minute (sccm) of SiH_4, 4.00 sccm of HCl, and 194.0 sccm of H_2 at 40 Torr total reactor pressure for 30 min, which yields an average growth rate of 600 nm/min. After nucleation, a long section of *n*-type Si was grown for a desired length after nucleation by turning on the PH_3 flow at a fixed flow-rate ratio of 1:10 SiH_4:PH_3, and the same gas phase ratio was used throughout the study. Doping modulation for GSL profiles was performed by abruptly

turning on and off the PH_3 flow at a constant time interval, followed by growing a long section of *n*-type again until growth termination. For doping-inverted *n*-type GSLs, the PH_3 flow profile was inverted, and the final intrinsic NW sections were grown for desired WG lengths. For *p*-type doping, the flow rate of B_2H_6 was stepwisely increased to the desired value achieving a flow-rate ratio of 1:7.5 SiH_4:B_2H_6 for the initial introduction of B_2H_6, and was abruptly modulated afterwards.

2.1.2 Epitaxial NW Growth

p-type Si (111) wafers (Nova Electronic Materials; B-doped; 1-10 Ω·cm) were cut into the same size described above, sonicated in acetone, IPA, and water and treated in a UV/O_3 cleaner at 150 °C for 5 minutes. Substrates were briefly immersed in buffered hydrofluoric acid (BHF, Transene BHF Improved) for native oxide removal, and Au NP deposition was performed in a solution containing 5 parts of prediluted Au NP solution (5% in water) and 1 part of BHF for 5 minutes. Au-functionalized substrates were then treated by UV/O_3 and BHF for removal of residual organics and native oxide, respectively.

NWs were nucleated at 480 °C with 2 standard cubic centimeter per minute (sccm) of SiH_4, 4 sccm of HCl, and 196 sccm of H_2 (96 sccm H_2 only for NWs in Figure 3.1C,D) at 2 Torr total reactor pressure for 60 min. For 200 mTorr growths, after the nucleation step, the reactor pressure was ramped to 20 Torr by 1 Torr every 12 s with 20 sccm of PH_3. For NWs used for quantification of Au, the SiH_4 partial pressure was modulated at a constant total reactor pressure by abruptly changing the SiH_4 flow rate with HCl flow rate adjusted proportionally. The only exception is the 20-to-200 mTorr transition in Figures 2 and 3 where the SiH_4 partial pressure was raised briefly from 20 to 100 mTorr for 12 s and then to 200 mTorr. All *n*-type doping was performed at a fixed ratio of 1:10 SiH_4/PH_3 flow rates, and doping modulation was performed by abruptly turning on and off the PH_3 flow. The flow rate of H_2 was adjusted for all changes to keep the total flow rate of all gases unchanged.

2.2 NW Etching

Si NW etching was performed either in aqueous KOH solution (diluted 20 wt.%) or in buffered hydrofluoric acid (BHF, Transene BHF Improved, diluted 2 vol.%) for intrinsic and *n*-type Si etching, respectively. For intrinsic Si etching, a growth substrate with epitaxial NWs was immersed in a 2% BHF solution by volume for 30 s to remove native oxide on the NWs and rinsed in water. The substrate was then immersed in

KOH solution (20 wt% in water with IPA capping layer) at room temperature for the desired length of time. After quenching in dilute glacial acetic acid (2 vol% in water), the substrate was rinsed in IPA and blown dry with nitrogen. For *n*-type Si etching, a substrate was immersed in 2 vol% of BHF with a hexane capping layer for 1-2 min, dried with nitrogen, and treated with UV/O_3 at 150 °C for 100 s. This immersion-oxidation process was iterated for a variable number of cycles. For Au removal, NWs were immersed in BHF for 15 s, rinsed in water for 10 s, and blown with nitrogen. The NWs were then immediately immersed in a solution of KI/I_2/H_2O (4:1:20 by weight) for 1 min followed by two 30 s water rinses, a 10 s IPA rinse, and blow-dry. We found that a brief BHF etch was needed prior to the Au etch, presumably to remove an ultrathin silicon oxide layer that can form on the surface of Au nanoparticles.

2.3 Single-NW Spectroscopy

2.3.1 Laser Microscope Design

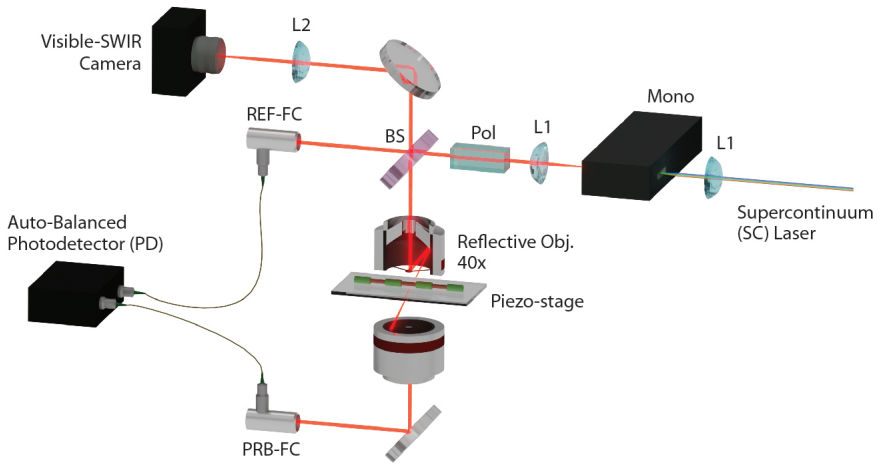

Figure 2.1: Laser microscope for polarization-resolved bright-field extinction measurements.

A broadband laser from a supercontinuum source was directed into a monochromator to output a single wavelength with <2 nm bandwidth. The laser was collimated into a beam size of 1 mm, polarized by a Glan-Thompson polarizer and split evenly into a reference and probe arms for balanced detection by Nirvana balanced photoreceivers. The polarization axis was always placed parallel to the table due to the uneven splitting ratio of the *p*- and *s*-polarized light for the beam splitter. If the polarization axis is placed perpendicular to the table the intensity of the probe arm drops substantially, which is detrimental to

measurements. After the beam splitter, the reference beam was directly fiber-coupled to the photoreceiver, and the probe beam was directed to one side of the back aperture of a reflective objective to deeply under-fill the aperture and achieve quasi-plane wave illumination with a low numerical aperture (see Figure 2.1). The transmitted probe beam was re-collimated by a matched objective and fiber-coupled to the photoreceiver.

The linear output and loop bandwidth settings on the photoreceiver were set to *AutoBal* and *100*, respectively. The *SIG* output reads the raw intensity of the probe beam and is used to monitor the quality of fiber coupling. *LINEAR* shows the autobalanced output and thus should stay at zero (or at the noise level) provided the autobalaning works correctly. *LOG* is a measure of the intensity ratio between the reference and probe beams reaching the detector (see user's manual for detailed equations), and must be tuned between -2 and 2 to obtain a good autobalancing performance. During operation, the custom program measures the *LOG* output at every wavelength and alerts when it goes out of the range. In case of alert, a reflective neutral-density filter wheel located in the reference beam path needs to be adjusted to bring the *LOG* back in the range. All three outputs were interfaced with a high-resolution data acquisition system (NI-9239, $\pm$10 V readout, 24-bit; National Instruments).

Optical imaging was performed by a visible-short wave infrared (Vis-SWIR) camera with a halogen lamp illuminating in a dark-field configuration for locating samples or with a laser beam for collection of guided spectra. More details of each optic used in the microscope are summarized in Table 2.1.

Table 2.1: List of optics used for the laser microscope

Label	**Description / Note**	**Manufacturer**
SC Laser	SuperK EXTREME EXB-6	NKT Photonics
Mono	Acton 2300i	Princeton Intruments
Visible-SWIR Camera	Ninox 640 VIS-SWIR	Raptor Photonics
Auto-Balanced PD	Nirvana 2007 (400-1070 nm), 2017 (800-1700 nm)	Newport
Piezo-Stage	Nano-LP200; 3-zxis positioner	Mad City Labs
Reflective Obj.	LMM-40-P01, 0.5 NA, Infinity-corrected	Thorlabs
FC	RC08FC-P01; Reflective, Protected silver	Thorlabs
BS	BSW16; 50/50 beam splitter, Ø2", 400-700 nm	Thorlabs
Pol	GTH10M; Glan-Thomson polarizer	Thorlabs
L1	AC254-100-A-ML; Achromatic doublet, Ø1"	Thorlabs
L2	AC508-075-A; Achromatic doublet, Ø2"	Thorlabs

2.3.2 Extinction and Waveguide Emission Measurement

NWs and NW GSLs were transferred onto standard glass microscopy slides (Fisher Scientific) coated with $\sim$3 nm of indium ti oxide (ITO) by physical vapor deposition (Kurt Lesker PVD 75) to facilitate SEM imaging performed afterwards. The sample of interest was first located and focused by moving a micrometer-driven manual translational sample stage and an objective lens stage. For polarization-resolved measurements, the position of the laser beam on the back aperture of the objective and the orientation of the NW on the substrate should change for each polarization because the polarization axis of the probe beam entering the objective is always fixed in one direction. For TM measurements, the NW needs to be placed along the operator's view angle and the beam should be directed through the right side of the back-aperture (see Figure 2.2A). For TE, the NW needs to be oriented horizontally with respect to the operator and the beam should be directed through the side nearest to the operator (see Figure 2.2B).

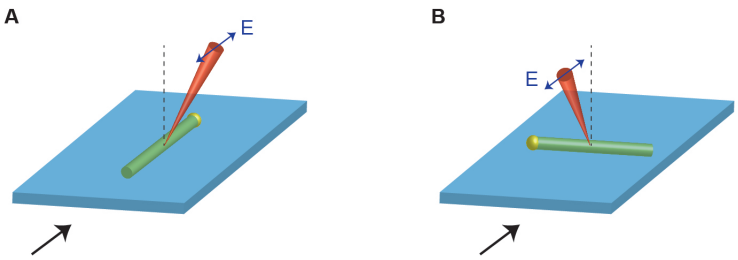

Figure 2.2: Laser illumination geometries for (A) TM- and (B) TE-polarized measurements. Black arrows represent the operators view angle.

The optical power was collected with the probe beam placed on and off the NW by modulating the substrate position using a piezo-positioner, and the NW must have a clean blank area around it to ensure a collection of a clean background spectrum. For doing this, the laser beam was scanned over the NW in the direction perpendicular to the NW axis using the piezo-stage with a step size of 0.2 μm while monitoring the *SIG* output from the detector, and the *on-wire* position was recorded from the point of the lowest intensity. In this step, a proper wavelength of the laser beam must be chosen to get enough signal modulation by scattering. Afterwards, the beam was moved to a clean blank area and the *off-wire* position was recorded. Extinction (%) was calculated as (1 - T) $\times$ 100 with $T = I / I_0$, where I and I_0 are transmitted powers collected with the beam on and off the NW, respectively. This position-modulated extinction measurement was repeated twice and averaged at every wavelength, and scanned over the desired spectral range. As described above, when the *LOG* value went outside the $\pm$ 2 range for the next wavelength, the filter wheel was adjusted to correct the *LOG* value and the measurement continued. The lowest measurable extinction was $\sim 10^{-3}$ (OD) with a single Au NR (Figure 2.3).

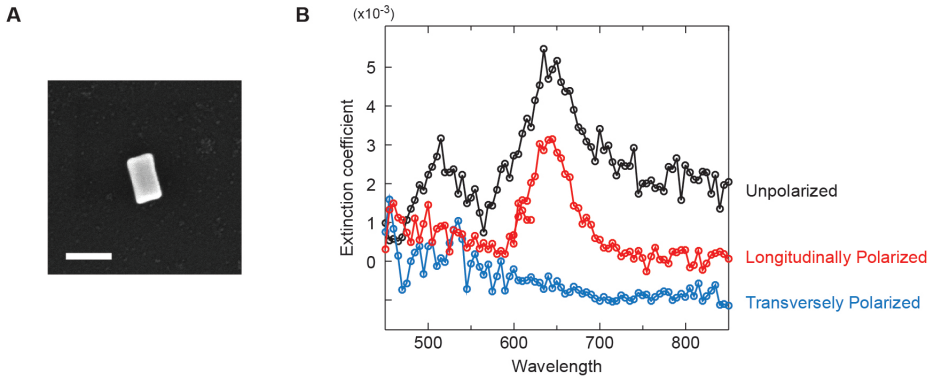

Figure 2.3: Extinction of single Au NR. (A) Scanning electron micrograph of a single Au NR; scale bar, 100 nm. (B) Polarization-resolved and unpolarized extinction spectra of a Au NR shown in panel (A).

The guiding spectra were collected by taking optical images at every wavelength and integrating the signal within the NW tip region. For optical switch experiments, sequential layers of PMMA (MicroChem 950PMMA.A4) were spun cast (Laurell WS-650MZ-23NPP) at 4000 rpm and baked at 150 °C.

2.4 Electron Microscopy Analysis

NWs were transferred to lacey-carbon TEM grids (Ted-Pella no. 01895) for STEM analysis by drop-casting NWs dispersed in IPA. STEM imaging was performed on a Tecnai Osiris operating at 200 kV with a subnanometer probe with a current of 2 nA (spot size 3, 4k extraction voltage). The Osiris is equipped with a Super-X EDS system, which consists of four solid-state detectors built into the objective lens. The maximum peak counts summed from the four detectors were on the order of 45 kcps. Collection times for each map were 13 min. Drift-corrected STEM EDS maps were obtained using Bruker Esprit software. Each EDS line scan profile of P and Au was fit to a previously reported fit function[67] consisting of an error function coupled with a Gaussian-convoluted exponential to extract transition widths. SEM imaging was performed with an FEI Helios 600 Nanolab Dual Beam System, and geometrical parameters of each GSL were determined using our home-written image analysis software.[68]

2.5 Numerical Modeling

Finite-element optical simulations were performed using COMSOL Multiphysics software by running scattered-field calculations with a TM- or TE-polarized plane wave or a Gaussian beam with a 1.5 μm FWHM defined over three-dimensional NW GSL structures. For plane wave simulations, a periodic boundary condition was applied in the axial direction at each side of a GSL repeating unit, and domains to the side of the NW GSL were surrounded by air and perfectly matched layers (PMLs). For simulations with a focused Gaussian beam, the beam is placed in the middle of the GSL section and NW waveguide segments on each side of the GSL were placed in PMLs. Q_{sca} and Q_{guided} were calculated by integrating Poynting vectors across the outer surface of a NW in all directions and across a cross-sectional area at the end of a NW waveguide, respectively, and dividing by the optical power incident on the projected area of the GSL. Propagation to both right and left directions was taken into account for calculating Q_{guided}, and absorption efficiency was added to Q_{sca} to calculate extinction efficiency, Q_{ext}.

For eigenvalue calculations, one period of a GSL was longitudinally sliced in half by a perfect electric conductor plane and placed between periodic boundaries in the axial direction. The air region surrounding the GSL was terminated by a scattering boundary. Complex eigenfrequencies were calculated for various values of d, e and p with a zero value for the axial wavevector traveling through the periodic boundary condition. The same calculation was performed with scanning the axial wavevector to obtain the band structure and angle-dependent Q-factors.

DESIGNING MORPHOLOGY IN EPITAXIAL SILICON NANOWIRES: THE ROLE OF GOLD, SURFACE CHEMISTRY AND PHOSPHORUS DOPING

3.1 Introduction

Semiconductor nanowires (NWs) grown by the vapor-liquid-solid (VLS) mechanism have emerged as promising building blocks in many technological areas,[69,70] and the bottom-up design of NWs with well-defined morphology has been recognized as an important route to impart functionality to NWs.[29] Various methods have been developed to realize morphology-controlled NWs, including spatially selective wet-chemical etching,[22,71] periodic radial deposition,[28] or Plateau-Rayleigh crystal growth,[30] and a range of applications have begun to be explored. For instance, NWs with a constriction have been demonstrated as a resistive memory element,[22] NWs encoded with a periodic grating by focused ion-beam lithography exhibit optical filtering capability,[61,72] and strong confinement of light is predicted in NW gratings with a defect cavity.[63] In addition, spicule-like NWs show a large mechanical hysteresis in insertion/regression from soft materials and could be relevant as biological probes.[71]

Previously, we demonstrated a process termed ENGRAVE (Encoded Nanowire GRowth and Appearance through VLS and Etching) to encode precise sub-10 nm morphology in VLSgrown silicon (Si) NWs.[22] The ENGRAVE process combines precise phosphorus (P) doping of Si NWs with dopant-dependent wet-chemical etching in aqueous potassium hydroxide (KOH) or buffered hydrofluoric acid (BHF) solution.[29] In prior studies, NWs were typically observed to grow in the $\langle 112 \rangle$ direction using nonepitaxial silicon oxide substrates. Here, we extend the ENGRAVE process to epitaxial Si NW growth on (111) Si substrates. Epitaxial growth is widely used in the growth of both group III-V and group IV NWs and is advantageous for the design of high-performance NW-based devices. For instance, vertical NW arrays exhibit beneficial

[1] Portions of this chapter reproduced with permission from Kim, S.; Hill, D. J.; Pinion, C. W.; Christesen, J. D.; McBride, J. R.; Cahoon, J. F. Designing Morphology in Epitaxial Silicon Nanowires: The Role of Gold, Surface Chemistry, and Phosphorus Doping. *ACS Nano* **2017**, *11* (5), pp 4453-4462. Copyright 2017 American Chemical Society.

light trapping properties[73–75] and have been used in the design of solar cells[76–78] and photoelectrochemical cells[79] using either axial or radial *p-n* junctions.[80] In biological areas, epitaxial NW arrays have shown their potential for serving as cell transfection platforms[81,82] and cellular mechanics probes.[83] In addition, precisely positioned single vertical NWs are good candidates for single-photon emitters[84] or for optical couplers[85] in photonic interconnects.

The mechanism of epitaxial growth of ⟨111⟩ Si NWs with gold (Au) catalysts has been widely studied. When silicon hydrides such as silane (SiH_4) or disilane (Si_2H_6) are used during chemical vapor deposition (CVD) growth on (111) substrates, it has been observed that epitaxial growth is stable only if Au decorates and passivates the sidewall of the NW.[86,87] If Au passivation of the surface is disrupted, kinking of NW growth into the more thermodynamically stable ⟨112⟩ direction is observed for NWs larger than ∼10–20 nm. Disruption of Au passivation and kinking has been induced by several methods, including an increase in Si_2H_6 partial pressure,[86,88] a modulation of the total reactor pressure during VLS growth,[89,90] or coercive hydrogenation of Si surface with hydrogen radicals.[91] Several potential mechanisms for Au decoration from the liquid VLS catalyst have been postulated, and one or several mechanisms may be relevant depending on growth conditions. These mechanisms include (i) diffusion of AuSi from the catalyst after completion of VLS growth,[92] (ii) wetting of the NW sidewalls with a thin AuSi eutectic liquid during or after growth,[88] or (iii) deposition of liquid AuSi particles as the liquidsolid contact line moves forward.[87] In all cases, the liquid AuSi droplets would phase separate into solid Au and Si upon cooling below the eutectic temperature at the end of the growth process, forming few-nanometer Au particles. Mechanisms i and ii can explain cases where a high Au density is found near the catalyst but not elsewhere on the NW. Mechanism ii can also explain a continuous distribution of Au along the NW if growth conditions allow the liquid AuSi to spread along the entire length of the NW during growth. Mechanism iii can explain a varying and nonuniform distribution of Au along the NW surface, such as observed ring patterns,[87] if the deposited AuSi is immobile on the NW surface.

Unlike NW growth with Si hydrides, growth with silicon tetrachloride ($SiCl_4$) does not require Au passivation, and high yields of epitaxial and uniform Si NWs have been achieved.[93,94] The absence of Au has been attributed to chlorination of the NW sidewalls, providing surface passivation and a diffusional barrier to Au.[95] Surface chlorination also suppresses $SiCl_4$ pyrolysis on NW sidewalls and produces uniform NWs without tapering. The introduction of HCl with silicon hydrides (e.g., SiH_4, Si_2H_6) is an alternate route to gain these advantages at the lower temperatures used to decompose the hydride precursors,[96,97] and epitaxial

$\langle 111 \rangle$ NWs that are apparently Au- and taper-free have been produced with SiH_4/HCl growth systems.[95,98,99] These growth conditions are found to be equally effective for *n*-type and *p*-type NWs doped using phosphine (PH_3) and diborane (B_2H_6) gases, respectively.[99]

Here, we report the synthesis of epitaxial Si NWs encoded with ENGRAVE morphology using SiH_4, HCl, and H_2 for NW growth at 480 °C and using PH_3 as the phosphorus (P) dopant precursor. Unlike prior reports on epitaxial NWs, we evaluate both the abruptness of dopant transitions and the efficiency of dopant-dependent wet-chemical etching in KOH and BHF solutions. The results highlight several mechanistic aspects of VLS growth that must be carefully controlled to enable the ENGRAVE process. First, we find that high SiH_4 partial pressures (>100 mTorr) and high NW growth rates (>150 nm/ min) are needed to avoid Au deposition on the sidewalls that inhibits wet-chemical etching in KOH solution. Second, we find that HCl is needed both to stabilize growth in the $\langle 111 \rangle$ direction at high growth rates and to avoid overcoating on the NW sidewall, which inhibits wet-chemical etching. Using the optimized growth conditions, we demonstrate a variety of complex morphologies in vertical NWs, a result that is expected to inspire the design of complex three-dimensional devices for electronic, photonic, and energy applications.

3.2 Results

3.2.1 Epitaxial Growth with HCl

Epitaxial Si NWs were nucleated in a home-built hot-wall chemical vapor deposition (CVD) system at 480 °C on (111) Si substrates with a SiH_4 partial pressure of 20–40 mTorr. After nucleation, the SiH_4 partial pressure was either constant or changed in a stepwise fashion. During any partial pressure change, the ratio of HCl and SiH_4 flow rates was maintained at a constant value of 2.0, and this ratio was used throughout the study except where noted otherwise. Under these conditions, a high yield of epitaxial and vertical NWs is achieved, as illustrated by the scanning electron microscopy (SEM) image in Figure 3.1A. Lattice-resolved transmission electron microscopy (TEM) imaging shown in Figure 3.1B confirms that the NWs grow in the $\langle 111 \rangle$ crystallographic direction.

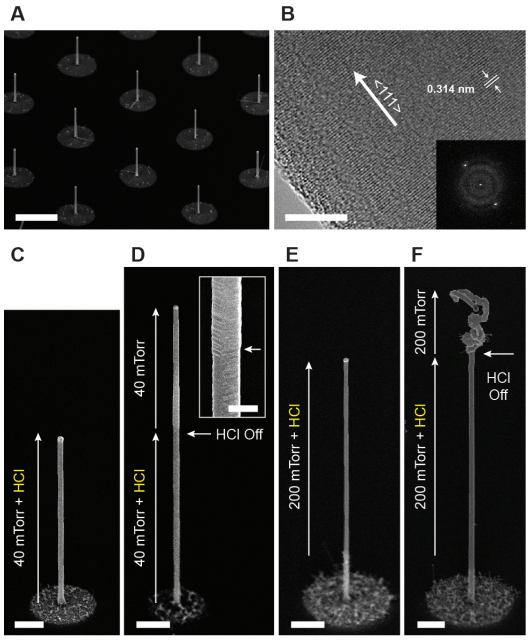

Figure 3.1: Growth of epitaxial $\langle 111 \rangle$ Si NWs. (A) Tilt-view SEM image of an array of vertical and epitaxial NWs grown on a (111) Si substrate; scale bar, 5 μm. (B) Lattice-resolved HRTEM image confirming the $\langle 111 \rangle$ growth direction of the epitaxial NWs; scale bar, 10 nm. Inset: fast-Fourier transform of the image showing diffraction spots consistent with the expected $\{111\}$ lattice spacing of 0.314 nm. (C–F) Characteristic SEM images of epitaxial NW growth at 480 °C with varying SiH_4 partial pressures and with or without HCl, as noted in each image. Arrows denote NW segments grown under distinct conditions; scale bars, 1 μm.

Panels C–F in Figure 3.1 compare epitaxial growth with and without HCl at 40 and 200 mTorr SiH_4 partial pressures. In the presence of HCl, NWs grow free of kinking and radial overgrowth at both partial pressures (Figure 3.1C,E), which is consistent with prior literature reports.[95,98,99] For a NW grown at 40 mTorr in which HCl was turned off midgrowth (Figure 3.1D), faceting of the NW as a result of radial overcoating (which occurs only during the growth segment without HCl) is observed, but the NW retains a linear and vertical orientation. In contrast, a NW grown at 200 mTorr, in which HCl was turned off midgrowth, shows dramatic instability, as indicated by the wormlike growth on the upper half of the NW (Figure 3.1F). This instability is consistent with previously observed unstable growth during a change in growth direction from $\langle 111 \rangle$ to $\langle 112 \rangle$.[86]

3.2.2 P Dopant Transitions

To study dopant transitions in the epitaxial NWs, a series of *n*-type/intrinsic/*n*-type (*n–i–n*) sequences was encoded in NWs at six different SiH_4 partial pressures ranging from 20 mTorr to 200 mTorr. For *n*-type sections, the PH_3 partial pressure was maintained at a ratio of 100:1 SiH_4 to PH_3 for all studies, corresponding to an encoded doping level of 5×10^{20} cm^{-3}. Growth durations for each partial pressure were adjusted to yield consistent segment lengths, assuming a linear scaling of growth rate with partial pressure. An elemental map of P and Si in the NW, collected by energy dispersive X-ray spectroscopy (EDS) in a scanning transmission electron microscope (STEM), is shown in Figure 3.2A. As is apparent from the image, each *n–i–n* sequence is easily resolved in the NW. Using the intrinsic segment lengths derived from the EDS map, a linear relationship of growth rate with partial pressure is verified, as shown in Figure 3.2B. EDS quantification of the P concentration in the segments indicates that the chemical doping level varies from 5.0 $\times 10^{20}$ cm^{-3} to 4.4 $\times 10^{20}$ cm^{-3} from 20 to 200 mTorr, respectively.

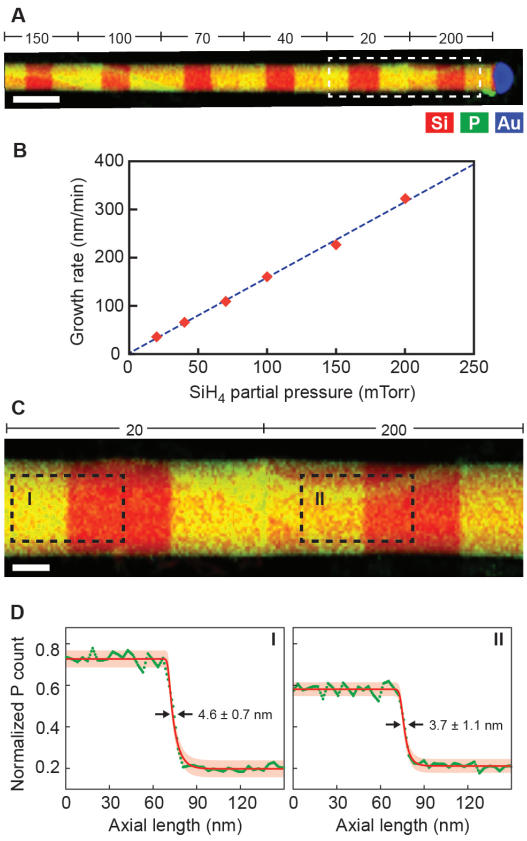

Figure 3.2: Abrupt P dopant modulation in epitaxial ⟨111⟩ Si NWs. (A) STEM EDS elemental map of a Si NW grown with six sequential *n*–*i*–*n* sequences, as denoted by the labels, at SiH_4 partial pressures of 150, 100, 70, 40, 20, and 200 mTorr. Si, P, and Au are depicted in red, green, and blue, respectively, and yellow regions correspond to overlapping Si and P signals; scale bar, 200 nm. (B) Si NW growth rates at 480 °C as a function of SiH_4 partial pressure. Dashed line represents a linear fit to the data with a slope of 1.6 nm·min^{-1}·mTorr^{-1} . Growth rate data was determined from the growth times and intrinsic segment lengths derived from the image in panel A. (C) High-magnification EDS elemental map of the white dashed area in panel A, showing *n*–*i*–*n* sequences grown at SiH_4 partial pressures of 20 mTorr (left) and 200 mTorr (right); scale bar, 50 nm. (D) P elemental line scans (green curves) along the NW axis derived from the dashed regions denoted I (left) and II (right) in panel C. Solid red lines denote fits of the profiles to exponential functions (see text), and the shaded red area denotes 95 % confidence intervals.

To evaluate the abruptness of dopant transitions, an EDS map of the area containing 20 and 200 mTorr segments was obtained with higher resolution, as shown in Figure 3.2C. Despite the 10-fold increase in

growth rate, no statistically significant broadening of the dopant transition width is observed. Line scans of each *n*-type-to-intrinsic transition are shown in Figure 3.2D along with fits to the single exponential function convoluted with a Gaussian to take into account instrumental broadening.[67] Calculated transition widths were 4.6 $\pm$ 0.7 and 3.7 $\pm$ 1.1 nm for 20 and 200 mTorr partial pressures, respectively. The sub-5 nm transitions and invariance of the transition width with growth rate confirm that the reservoir effect, in which the liquid catalyst can retain P dopants and broaden transition widths, has been suppressed under these growth conditions.[67] The dopant transition widths in these VLS-grown NWs are only slightly broader than the transition widths recently reported with a solid rather than liquid catalyst.[100]

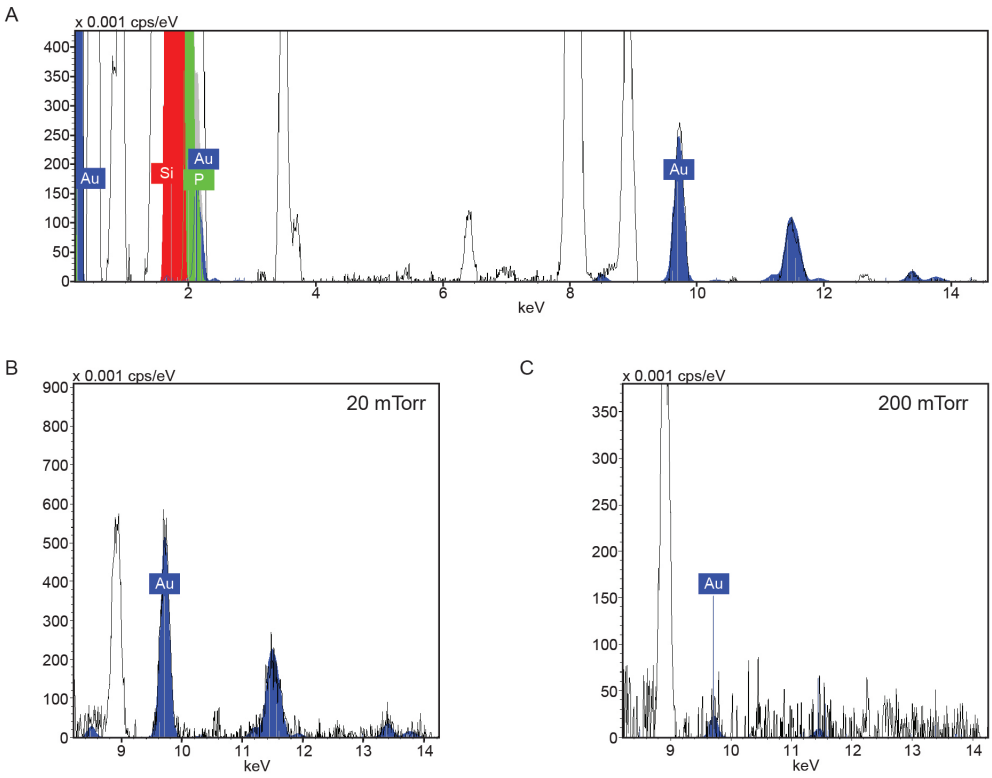

Figure 3.3: Fit of the EDS spectrum used to determine relative amounts of each element. (A) Example of a fit of the entire EDS spectrum. (B, C) Fits of EDS spectra around Au peaks at 20 mTorr (B) and 200 mTorr (C).

3.2.3 Role of Surface Au

Figure 3.4A shows a bright-field STEM image and EDS elemental heatmap of Au for the same multisegmented *n–i–n* NW shown in Figure 3.2. The image shows that Au is heterogeneously deposited on the surface of the epitaxial NW, and the quantity of Au within each *n–i–n* segment strongly depends on the growth rate and SiH_4 partial pressure. In particular, the Au colormap shows a signal intensity progressively increasing with decreasing partial pressure from 150 to 20 mTorr and a sudden drop in Au at the transition from 20 to 200 mTorr. A magnified elemental heatmap of the last two *n–i–n* segments, grown at 20 and 200 mTorr, is presented in Figure 3.4B. The 20 mTorr segment shows high Au counts with a number of Au nanoclusters. The net atomic percentage of Au in the 20 mTorr segment, as determined by EDS mapping, is 0.12 %, which corresponds to a surface Au coverage of 2.2 atoms·nm^{-2} . This value agrees well with previous reports for NW growth in the $\langle 111 \rangle$ direction,[88] and loss of this relatively small quantity of Au would produce a subtle ($<$2 nm/micron) change in the diameter of the 100 nm Au catalyst as the NW grows. However, the Au signal at 200 mTorr falls below the detection limit (Figure 3.3), suggesting that the Au deposition is dramatically depressed. In addition, the presence of an abrupt transition from a high-intensity to near zero-intensity zone suggests that there is no substantial diffusion of Au or AuSi during the VLS growth. Thus, the deposited Au appears to be immobile on the surface during growth, which is consistent with prior reports that surface chlorination suppresses Au diffusion.[98] In addition, the localized heterogeneity of the Au and absence of Au on the Si surface close to the Au catalyst suggests that the Au is deposited as the liquid contact line moves forward during VLS growth (corresponding to mechanism iii discussed above).

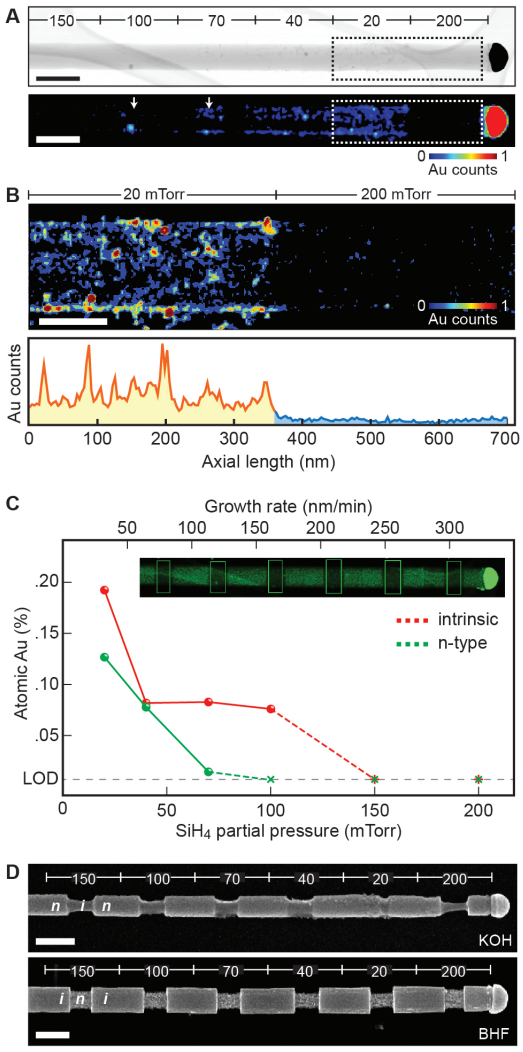

Figure 3.4: Characterization of Au surface aggregation as a function of NW growth rate and P doping. (A) (Top) Bright-field STEM image of a single-crystalline Si NW grown with six *n*–*i*–*n* sequences, as denoted by the labels, at SiH_4 partial pressures of 150, 100, 70, 40, 20, and 200 mTorr; scale bar, 200 nm. (Bottom) Normalized heatmap of the Au EDS signal from the NW shown in the upper panel. White arrows indicate preferential deposition on intrinsic segments at 70 and 100 mTorr; scale bar, 200 nm. (B) (Top) Normalized heatmap of the Au EDS signal from the regions denoted by the dashed boxes in panel A; scale bar, 100 nm. (Bottom) Au elemental line scan along the NW growth axis derived from the image in the upper panel. (C) Au atomic percentages as a function of SiH_4 partial pressure (bottom axis) or growth rate (top axis) for *n*-type segments (green) and intrinsic segments (red). Data derived from the NW shown in panels A and B. LOD refers to

the limit of detection. Inset: STEM EDS elemental map of P showing the regions (green rectangles) used to collect data for intrinsic segments. (D) SEM images of NWs grown with *n*–*i*–*n* (top) or *i*–*n*–*i* (bottom) segments at SiH_4 partial pressures of 150, 100, 70, 40, 20, and 200 mTorr, as denoted by labels. NWs were etched with KOH solution (top) or BHF solution (bottom); scale bars, 200 nm.

In Figure 3.4C, we quantify the amount of Au deposited as a function of SiH_4 partial pressure for both intrinsic and *n*-type segments. The Au signal decreases rapidly with increasing SiH_4 partial pressure and falls below the detection limit at 100 mTorr for *n*-type and 150 mTorr for intrinsic regions. At intermediate partial pressures of 70 and 100 mTorr, the Au signals on the intrinsic regions are substantially larger than on the *n*-type regions. This trend is apparent in the intrinsic regions denoted by arrows in the heatmap of Figure 3.4A, showing substantial Au in comparison to the adjacent *n*-type regions. In addition, SEM images of larger diameter NWs (Figure 3.5) also show clear Au deposition on intrinsic segments.

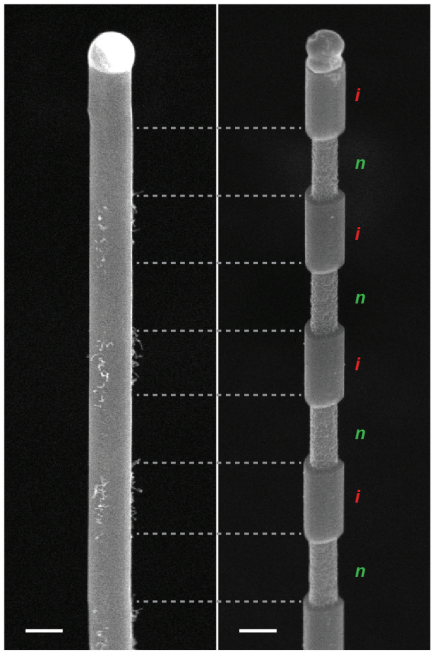

Figure 3.5: Tilt-view SEM images of Vertical Si NW grown at a constant SiH_4 partial pressure with dopant modulation before (left) and after (right) etching in BHF. Secondary whiskers are preferentially found on intrinsic Si.

As shown by the two SEM images in Figure 3.4D, we evaluated the quality of ENGRAVE structures by wet-chemical etching of NWs with *n–i–n* or *i–n–i* segments grown at varying SiH_4 partial pressures using KOH and BHF solutions, respectively. In KOH solution, we expect the intrinsic segments to selectively etch, and we observed smooth and conformal etching for all segments grown above 100 mTorr (upper panel in Figure 3.4D). However, at or below 100 mTorr, the intrinsic segments exhibit imperfect and nonuniform etching. The poor etching appears to be directly correlated with the deposition of Au on the NW surface, and this result is consistent with the recent report of an Au-enabled etch stop in Si NWs.[?] In contrast, the BHF etching was substantially less affected by the surface Au (bottom panel in Figure 3.4D). In BHF solution, we expect the *n*-type regions of the *i–n–i* segments to selectively etch,[29] and all of these regions exhibited good etching independent of the SiH_4 partial pressure. The only minor effect was a slight increase in the etch rate with increasing surface Au, which could be attributed to the appearance of a metal-assisted etch mechanism.[101,102] However, the relatively minor effect suggests that etching of *n*-type Si in BHF occurs primarily by the dopant-dependent electrochemical etch mechanism.[103,104] Note that in a control study shown in Figure 3.6, we found that the total reactor pressure in the CVD system played no role in the deposition of Au on the NW surfaces and that instead the SiH_4 partial pressure was the key deterministic factor.

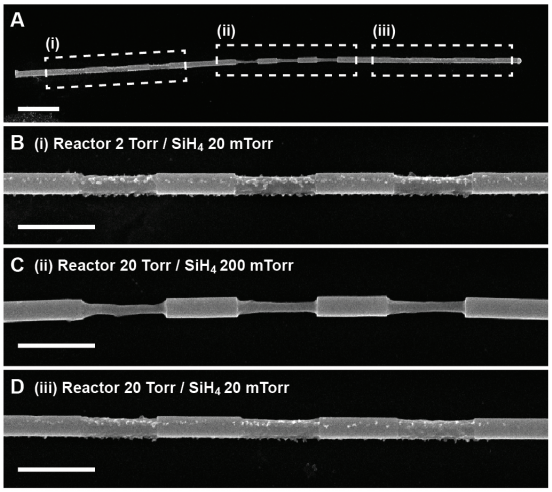

Figure 3.6: Effect of total reactor pressure on etching. (A) SEM image of etched Si NW grown sequentially with three different reactor pressure/ SiH_4 partial pressure combinations; (i) 2 Torr/20 mTorr, (ii) 20 Torr/200 mTorr, and (iii) 20 Torr/20 mTorr. Scale bar, 1 μm. (B–D) High-magnification SEM images of the three sections in panel A. Scale bars, 500 nm.

The reproducibility of the Au etch stop behavior in KOH solution was confirmed through the growth of intrinsic NWs with the SiH_4 partial pressure periodically modulated between 20 and 200 mTorr, as shown in Figure 3.7A. The pressure modulation resulted in the periodic deposition of Au nanoclusters on the sidewall of the NW, as apparent from the secondary VLS whiskers in the low partial pressure regions in the SEM of Figure 3.7A. Etching of the NW in KOH solution (Figure 3.7B) produced a grating structure in which the high partial pressure regions etched whereas the low partial pressure regions did not. To further confirm that the etch stop behavior was the result of Au deposition, we removed Au from the NW surface using a brief BHF etch followed by a potassium iodide (KI) Au etch. As apparent from the SEM images in Figure 3.7C, the Au etchant removes the Au catalyst from the NW, and all regions of the NW exhibit substantial etching in KOH solution. This result confirms that Au removal from the NW sidewall eliminates the periodic structure observed after KOH etching, confirming the role of Au as an etch stop. The relatively small degree of periodicity still remaining in the NW is attributed to incomplete removal of Au during the KI etch.

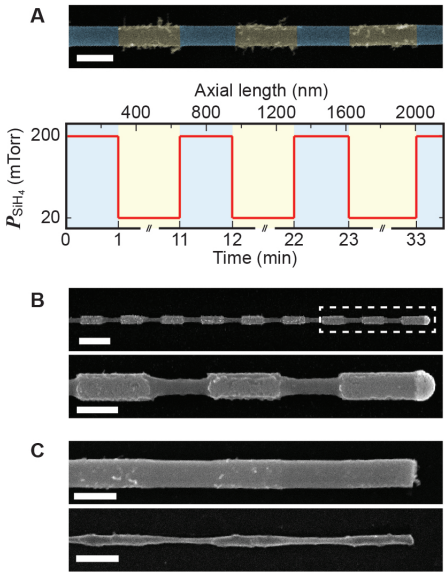

Figure 3.7: Impeding KOH wet-chemical etching in intrinsic Si NWs through localized Au aggregation. (A) (Top) False-colored SEM image of a Si NW in which blue segments were grown at 200 mTorr and yellow segments at 20 mTorr by modulating the SiH_4 flow between 2.0 and 0.2 standard cubic centimeters per minute (sccm); scale bar, 200 nm. (Bottom) SiH_4 partial pressure ($\boldsymbol{P}_{SiH_4}$) as a function of time (bottom axis) or axial NW length (top axis) for the NW shown in the upper panel. (B) (Top) SEM image of an intrinsic Si NW with modulated partial pressure after etching in aqueous KOH solution; scale bar, 500 nm. (Bottom) Magnified SEM image of the dashed area in the top panel; scale bar, 200 nm. (C) (Top) SEM image of a Si NW after Au removal using an aqueous KI wet-chemical etch. (Bottom) SEM image of the same Si NW as shown in the top panel after etching in KOH solution; scale bars, 200 nm.

3.2.4 Role of HCl on NW growth

To further understand the role of HCl and surface chlorination, we synthesized a NW with *n*–*i*–*n* segments grown at varying HCl-to-SiH_4 partial pressure ratios with the SiH_4 partial pressure fixed either to 20 or 200 mTorr, as shown schematically in Figure 3.8A. A SEM image of the NW after wet chemical etching in KOH solution is shown in Figure 3.8B. As apparent from the image, intrinsic segments grown at 200 mTorr etch uniformly, whereas intrinsic segments grown at 20 mTorr do not etch. Surprisingly, a 5-fold change in the ratio of HCl to SiH_4 ratio produces no substantial change in the etch behavior. Even at the highest ratio, with a HCl partial pressure of 80 mTorr, the *n*–*i*–*n* segments grown at low growth rate with a SiH_4 partial pressure of 20 mTorr exhibit no etching, which we attribute to the deposition of Au on the NW surface. Figure 3.8C

shows SEM images of a NW grown at a SiH_4 partial pressure of 200 mTorr and *n–i–n* segments grown at a HCl/SiH_4 ratio varying from 0.1 to 5. For a ratio below ∼1.0, there is some evidence that Au begins to appear on the NW surface, as shown by the segment labeled I and grown with a pressure ratio of 0.1. However, even this *n–i–n* segment, grown at a high growth rate but low HCl partial pressure of 20 mTorr, still exhibits substantially better etching than any segment grown at low growth rate.

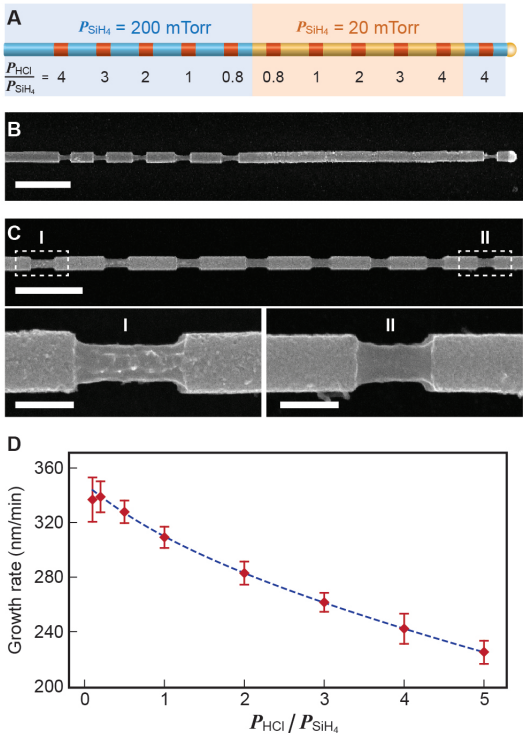

Figure 3.8: Influence of HCl and surface chlorination on NW growth rate, Au aggregation, and NW wet-chemical etching. (A) Schematic of a Si NW grown at 200 and 20 mTorr SiH_4 partial pressure with HCl to SiH_4 pressure ratios ($\boldsymbol{P}_{HCl}/\boldsymbol{P}_{SiH_4}$) ranging from 0.8 to 4. Red regions denote the intrinsic segments surrounded by *n*-type segments. (B) SEM image of a Si NW, corresponding to the diagram in panel A, after etching in KOH solution; scale bar, 500 nm. (C) (Top) SEM image of a Si NW etched in KOH solution with *n–i–n* segments grown at $\boldsymbol{P}_{HCl}/\boldsymbol{P}_{SiH_4}$ ratios, from left to right, of 0.1, 0.2, 0.5, 1, 2, 3, 4, and 5; scale bar, 1 m. (Bottom) Magnified SEM images of etched segments labeled I (left) and II (right) grown with at $\boldsymbol{P}_{HCl}/\boldsymbol{P}_{SiH_4}$ ratios of 0.1 and 5, respectively; scale bars, 200 nm. (D) Plot of growth rate versus the $\boldsymbol{P}_{HCl}/\boldsymbol{P}_{SiH_4}$ ratio, ranging from 0.1 to 5, at a constant SiH_4 partial pressure of 200 mTorr. Growth rate data was acquired from the intrinsic segment lengths of NWs etched as shown in panel C.

The only clear effect of changing the HCl to SiH_4 ratio was a change in the NW growth rate. As illustrated in Figure 3.8D for NWs grown at 200 mTorr, we observed a 30–35 % decrease in growth rate when the ratio was changed from 0.1 to 5.0. This effect can most likely be attributed to a gas-phase reaction between SiH_4 and HCl to form silicon chlorides such as $SiCl_2$.[105,106] Because Si–Cl has a larger bond strength than Si–H,[100,107] the formation of silicon chlorides is expected to decrease the rate of Si incorporation into the catalyst, depressing the growth rate. This growth rate reduction with HCl qualitatively agrees with a previous report on the kinetics of Si epitaxy in which SiH_4 and HCl were employed.[106]

3.3 Discussion

3.3.1 Role of Surface Chemistry

The results presented in Figures 3.1–3.8 highlight the importance of both HCl and a high SiH_4 partial pressure ($>$100 mTorr, corresponding to a growth rate $>$150 nm/min) for achieving high-quality vertical NWs with abrupt dopant transitions and segments that can be selectively etched using either KOH or BHF solutions. Although the microscopic mechanisms causing Au deposition and catalyst stability or instability remain an open question, the results presented herein can be reasonably well explained within the framework of the Si NW surface chemistry. For this discussion, we assume the Si surface will be found in one of four states during VLS growth: (i) unpassivated, (ii) passivated with hydrogen, (iii) passivated with chlorine, or (iv) passivated or coated with Au(s) or AuSi(l). As illustrated in Figure 3.9, we can use these four states to explain the experimental observations in this study

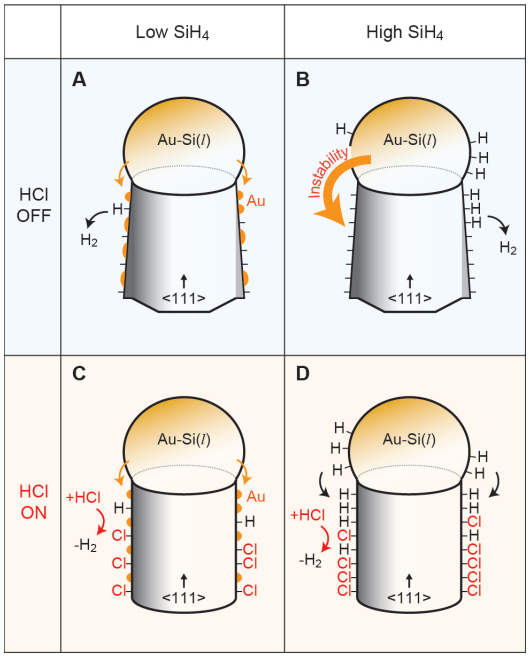

Figure 3.9: Schematic illustration of surface passivation during VLS growth under various process conditions, including (A) low SiH_4 partial pressure without HCl, (B) high SiH_4 partial pressure without HCl, (C) low SiH_4 partial pressure with HCl, and (D) high SiH_4 partial pressure with HCl.

First, we can hypothesize why vertical $\langle 111 \rangle$ NWs can be grown without HCl if the growth rate is low but not if the growth rate is high. At low growth rates, we found the NW surface to be coated with small Au particles (Figure 3.9A), which serve to passivate the NW sidewall and stabilize $\langle 111 \rangle$ growth. At high growth rates, however, the Au particles are absent. In this case, the NW sidewall may be passivated with hydrogen in regions close to the triple-phase boundary (see the paragraph below), but hydrogen is expected to have desorbed at regions farther from the boundary (Figure 3.9B). Desorption thus leaves a large surface area without passivation, and we propose that a large volume of the AuSi(l) catalyst will then wet this surface, causing instability and the worm-like growth apparent in Figure 3.1F. This hypothesis is supported by multiple literature studies that have proposed the same mechanism of $\langle 111 \rangle$ growth stabilization by surface Au.[86,87]

Second, we can hypothesize why the Au nanoparticles appear on the NW surface at low growth rates and SiH_4 partial pressures but not at high growth rates and partial pressures. Pyrolysis of SiH_4 is known to provide H atoms that can passivate the NW sidewall,[91] and we presume that pyrolysis predominantly occurs at the surface of the catalyst because no Si deposition is observed on the NW sidewall. In addition, the growth temperature is too low for surface hydrogenation by molecular H_2 but high enough to desorb surface

hydrogen into H_2. Therefore, the surface concentration of H will depend both on the rate of SiH_4 pyrolysis and the rate of H desorption as H_2. Thus, at low SiH_4 partial pressures, we expect minimal H to be present on the catalyst surface because H_2 desorption will be faster than H can be supplied from the SiH_4. As illustrated in Figure 3.9A, this causes the Si NW surface in the vicinity of the triple-phase boundary to be unpassivated, causing deposition of Au on the sidewall of the NW. At high SiH_4 partial pressures, however, the higher rate of SiH_4 pyrolysis provides a larger supply of H to the catalyst, causing the Si NW surface in the vicinity of the triple-phase boundary to be passivated (Figure 3.9B). The H passivation suppresses deposition of Au.[108] The absence of Au in P-doped *n*-type sections of the NWs grown at intermediate SiH_4 partial pressures (cf. Figure 3.4C) supports this explanation because PH_3 pyrolysis provides an additional source of H. Moreover, P could potentially act as a passivating agent, and P-doped Si NWs are often observed to contain a thin layer of heavily doped Si at the surface.[109] In addition, the absence of H passivation in the vicinity of the triple phase boundary also explains the deposition of Au at low SiH_4 partial pressures for NWs grown with HCl (Figure 3.9C). Note that given the tendency of H to desorb from the Si surface at the growth temperature of 480 °C,[91,96] we expect that H will be present only in the vicinity of the triple-phase boundary and to have desorbed from regions further from the catalyst. These results highlight a key difference between NW growth with $SiCl_4$[95] and NW growth with SiH_4 and HCl. In the former case, immediate Cl passivation at the triple-phase boundary presumably prevents Au deposition, whereas in the latter case hydrogen passivation is required to prevent Au deposition at the triple-phase boundary.

Third, we can hypothesize why HCl induces stable $\langle 111 \rangle$ NW growth at high SiH_4 partial pressures. After growth of new Si crystal planes at the triple phase boundary, we expect that the surface will be rapidly chlorinated by HCl, as indicated in Figure 3.9C,D. For low SiH_4 partial pressures, the NW surface is already passivated by Au, which alone is able to stabilize NW growth in the $\langle 111 \rangle$ direction. Thus, the addition of surface chlorination does not have any direct additional impact on the catalyst stability. For high SiH_4 partial pressures without Au on the surface, however, Cl passivation is critical for preventing the liquid catalyst droplet from wetting the surface and inducing a kink[88,91] or wormlike growth.[86] This effect can be explained by a high Si–Cl(s)/AuSi(l) solid/liquid surface energy, where Si–Cl(s) refers to a chlorinated silicon surface. In addition, the NW surface chlorination prevents additional Si deposition on the NW sidewall, preserving the cylindrical NW geometry and preventing the appearance of surface faceting and a tapered structure. Note that the results shown in Figure 3.1D for a NW grown with and without HCl at a low SiH_4 partial pressure suggest that the primary role of HCl is Cl passivation that prevents deposition rather than Si etching by HCl

after deposition. In Figure 3.1D, the region grown with HCl shows less sidewall deposition than the region grown without, indicating the Cl passivation was stable for some time even after HCl was removed from the CVD system. In addition, NWs grown with HCl are never observed to be inversely tapered (narrower at the base rather than tip), indicating that Si etching is not a primary process during growth. These observations are consistent with the fact that $SiCl_2$ is known to desorb only at temperatures $\sim$100 °C higher than the NW growth temperature used herein.[96,110,111]

Although a discussion of surface chemistry during VLS growth provides a reasonable framework for interpreting the experimental observations, there is still a need for future studies that can provide direct evidence of the proposed mechanisms. Moreover, an alternate explanation for the presence or absence of Au at low or high SiH_4 partial pressures and growth rates, respectively, can be proposed. A high NW growth rate is a consequence of a higher supersaturation of the liquid AuSi catalyst. If we assume that during VLS growth Au is deposited on the NW sidewall either in the form of solid Au or liquid AuSi droplets at the liquidus concentration, then the deposition will cause a decrease in the atomic percentage of Au in the liquid catalyst. Under supersaturation conditions, which possess a high nonequilibrium percentage of Si, the loss of Au will induce a substantial free energy penalty to the microscopic system.[100] This free energy penalty increases with increasing supersaturation of the liquid catalyst. Thus, the absence of Au at high SiH_4 partial pressure could potentially originate from the higher catalyst supersaturation, which induces a higher free energy barrier for deposition of a small Au particle on the NW surface. However, the passivation effect of the Au (i.e., passivation of a Si dangling bond) may mitigate this effect. The current set of experimental results cannot conclusively distinguish between an explanation based on catalyst supersaturation or NW surface chemistry.

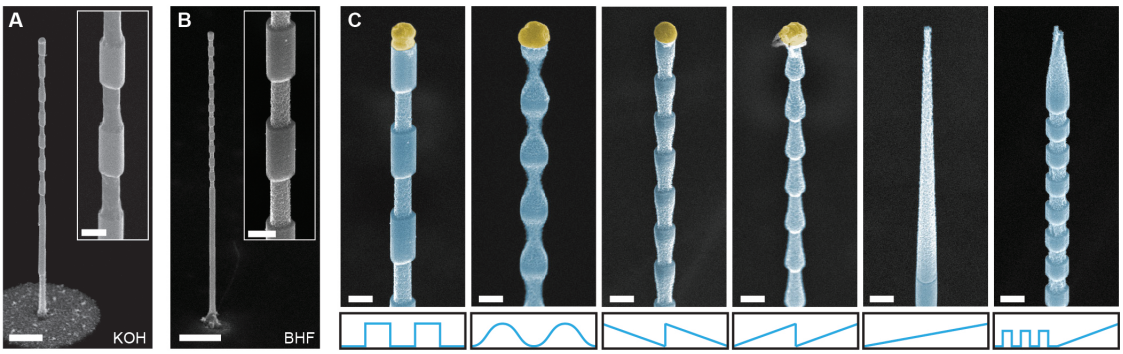

Figure 3.10: Encoding complex morphology in vertical Si NWs. (A, B) Tilt-view SEM images of vertical NW gratings in epitaxial ⟨111⟩ Si NWs prepared by etching in KOH solution (panel A) and BHF solution (panel B); scale bars, 1 m. Insets: magnified views of each etched NW; scale bars, 200 nm. (C) False-colored tilt-view SEM images of vertical NWs with various morphologies created by P dopant modulation and BHF etching. The Au catalyst is false-colored in yellow and Si in blue; scale bars, 200 nm. Lower panels depict the PH_3 flow profile and dopant profile used to encode the morphology in the final 1 m of each NW.

Figure 3.10A shows a vertical NW grating prepared by Au-free ⟨111⟩ epitaxial growth and subsequent etching in KOH solution, and Figure 3.10B shows an analogous vertical NW grating prepared by BHF etching using an iterative oxidation and etch process described elsewhere.[29] Each NW contains sub-5 nm P dopant transitions; however, more abrupt morphological junctions are found in the gratings prepared by BHF compared to KOH solutions, which is most likely the result of broadening due to mass transport of the KOH etchant in solution.[67] Using optimal growth and etching conditions, a broad set of complex morphologies can be encoded in vertical NWs, as shown by the gallery of encoded NWs—including gratings, sinusoids, sawtooths, and tapers—depicted in Figure 3.10C.

3.4 Conclusion

We have demonstrated the importance of understanding and controlling the microscopic details of NW synthesis in order to design complex, morphology-encoded epitaxial NWs. Epitaxial Si NWs with sub-5 nm P dopant transitions and Au-free sidewalls are found to grow in a high SiH_4 partial pressure environment in the presence of HCl. We have shown by quantitative electron microscopy analyses that deposition of Au on the NW sidewall is highly correlated with SiH_4 partial pressure. Surface Au-free NWs with encoded dopant patterns exhibit conformal etching in aqueous KOH or BHF solution, creating complex morphologies in

epitaxial NWs. We expect that the precise and high-resolution morphological control demonstrated here can serve as a versatile tool for a variety of technologies.

MIE-COUPLED BOUND GUIDED STATES IN NANOWIRE GEOMETRIC SUPERLATTICES

4.1 Introduction

Optical interconnects and logic elements operating on the nanometer scale could enable the leap into all-optical computing technology, which would alleviate the bandwidth and energy consumption limitations of current technologies.[112] For instance, dielectric waveguides (WGs) made on silicon-on-insulator (SOI) platforms have been widely explored for carrying and modulating optical signals;[113] however, they are confined to a planar geometry, and coupling light into and out of these structures relies on conventional grating couplers that are often orders of magnitude larger in size than the WGs.[114,115] Nanowires (NWs)[116] offer an alternate platform on which to design dielectric WGs at exactly the diffraction limit in an optimal cylindrical geometry.[50,51,60,117] NWs enable the guiding of light in flexible, non-planar, three-dimensional geometries, and permit the addition of conformal cladding materials including dielectrics and metals.[44] Despite these advantages, in-coupling of light to NW WGs remains problematic and has relied on scattering at NW end facets[50,51] or end-on parallel coupling to the NWs[60,117] because there is no comprehensive light coupling scheme for a NW geometry. Moreover, existing methods are not spectrally selective, limiting their utility for applications where mode-selection is important. Given that NWs are also well known to exhibit strong Mie resonances,[33,47] there have been efforts to explore the connection between Mie resonances and guided modes.[48] However, because of momentum mismatch, guided modes are by their nature inaccessible optical bound states[118] under normal incidence light, leaving the opportunities for interplay between a Mie and guided mode as yet obscure.

Nanoscale systems often exhibit unique light-matter interactions[119] when the geometric and compositional design of a system causes complex wave interference effects, which can include Fano resonances,[120]

[2] Portions of this chapter reproduced with permission from Kim, S.; Kim, K.-H.; Hill, D. J.; Park, H.-G.; Cahoon, J. F. Mie-coupled bound guided states in nanowire geometric superlattices. *Nature Communications* **9**, Article number: 2781 (2018).

electromagnetically induced transparency (EIT),[121] and scattering dark states.[122,123] A Fano resonance arises from weak coupling between two resonances with different damping rates, creating an abrupt spectral feature in the optical response. EIT and scattering dark states originate from oppositely-oriented radiative resonances that destructively interfere with each other in the far field.[121–125] The same optical effect can occur in systems with a near-field interaction between a super-radiant, bright mode and a sub-radiant, dark mode.[126,127] In this case, an exchange of energy between the modes results in a coupled excitation of the bright and dark state, causing an abrupt Fano-like or EIT-like feature in the optical response. Far-field and near-field interactions are usually interchangeable frameworks that can describe the same phenomena with a different basis set.[122,128] These spectral features are often generated through geometric perturbation of a nanostructure to break spatial symmetry, causing a previously dark state to be accessed.[121,126,129,130]

Here, we show that a NW geometric superlattice (GSL), which breaks the infinite translational symmetry of a NW, can couple a Mie resonance with a bound-guided state (BGS) of the NW. Complementary to reports on bound states in the continuum (BIC),[118] which describe the appearance of bound states above the light cone, we selectively access one normally inaccessible BGS from a continuum of conventional bound states below the light cone by precisely modulating the NW geometry. As a result, a sharp, Fano-like feature that can be assigned as a scattering dark state appears in the Mie scattering spectrum at the wavelength of the BGS. The geometric dependence of both the Mie resonance and BGS provides broadband tuning of the effect from visible through near-infrared wavelengths. We experimentally demonstrate the appearance of scattering dark states from NW GSLs and show selective guiding of light up to telecommunication wavelengths with a Fourier-transform-limited bandwidth. This report is the first demonstration of Mie-BGS coupling and selective narrow-band guiding in a NW WG system. In addition, we show that the coupling wavelength is highly sensitive to the local refractive index, an effect that we use to design a sensor and optical switch.

4.2 Results and Discussion

4.2.1 Mie-BGS coupling in a NW GSL

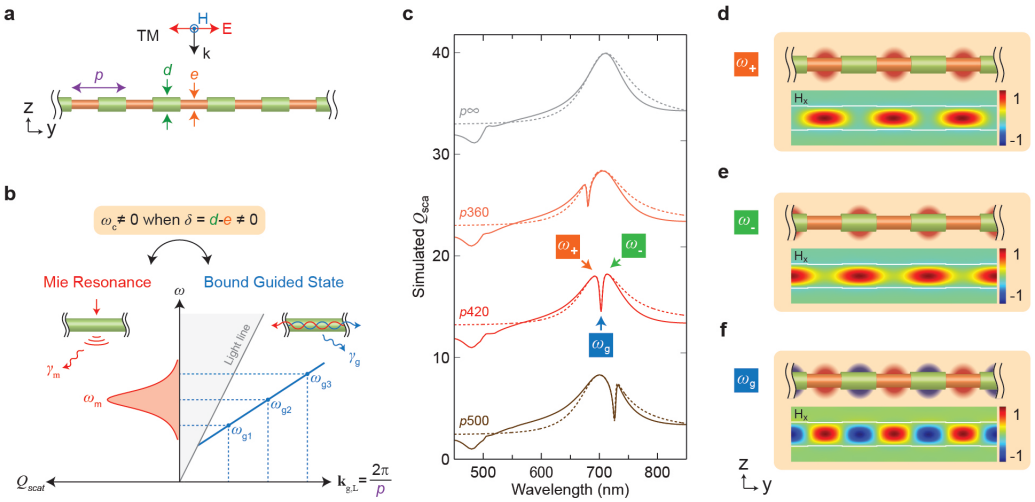

Figure 4.1: The geometry and coupled resonances of a NW GSL. **a** Structure and illumination geometry of a Si NW GSL. **b** Schematic illustration of a leaky Mie resonance with a broad spectral envelope (left) and a continuum of BGS states (right), in which a specific BGS state, ω_g, is selected by the choice of pitch p. **c** Numerically calculated spectra of Q_{sca} (solid lines) and analytical fit by TCMT (dotted lines) for an infinite NW with uniform d (= 0) of 140 nm (gray) and for NW GSLs with d = 140 nm, e = 135 nm, and varying p of 360 nm (orange), 420 nm (red), and 500 nm (brown). The pitch, p, in nanometers is denoted for each spectrum, where $p = \infty$ corresponds to an infinite NW of uniform diameter d. All spectra are successively offset vertically by 10. **d–f** Schematic and calculated magnetic field profiles for a GSL with p = 420 nm at frequencies of ω_+ (**d**), ω_- (**e**), and ω_g (**f**), corresponding to the red spectrum and labels in **c** at wavelengths of 692, 713, and 703 nm, respectively.

The geometry of a NW GSL, illustrated in Figure 4.1a, is uniquely defined by three geometrical parameters, the pitch (p), outer diameter (d), and etch diameter (e), and is composed of equally spaced cylindrical segments of modulated diameter ($\delta = d - e$), where each segment has an axial length of $p/2$. We consider this structure illuminated at normal incidence under TM polarization with the magnetic (**H**) and electric (**E**) fields perpendicular and parallel, respectively, to the NW axis. Figure 4.1b schematically

illustrates coupling between the two eigenmodes in a NW geometry, a Mie resonance that strongly couples with a free-space plane wave and a BGS selected from the continuum. Here, we consider the criterion for an ideal bound state to be absence of loss, absence of external coupling, and time invariance of energy within the structure. Thus, for a NW system, the ideal BGS refers to a standing wave with amplitude A_g formed by the superposition of two counter-propagating guided modes, $A_{\mathrm{g}} = [A_{\mathrm{r}}(\mathbf{x},\mathbf{z})B(\mathbf{y})\exp(\mathrm{i}\mathbf{k}_{\mathrm{g,L}}(\mathbf{y}\text{-}\mathbf{y}_0) - \mathrm{i}\omega_{\mathrm{g}}t)$ $+ A_{\mathrm{l}}(\mathbf{x},\mathbf{z})B(\mathbf{y})\exp(-\mathrm{i}\mathbf{k}_{\mathrm{g,L}}(\mathbf{y}\text{-}\mathbf{y}_0) - \mathrm{i}\omega_{\mathrm{g}}t)]$, with the same angular frequency (ω_{g}) and longitudinal wavevector ($\mathbf{k}_{\mathrm{g,L}}$), where $\mathbf{y}$ is spatial position along the NW axis, $\mathbf{y}_0$ is the spatial origin chosen to coincide with the center of a GSL segment, $A_{\mathrm{r}}(\mathbf{x},\mathbf{z})$ and $A_{\mathrm{l}}(\mathbf{x},\mathbf{z})$ are the cross-sectional amplitudes of right- and left-propagating guided modes, respectively, (with $A_{\mathrm{r}} = A_{\mathrm{l}}$, for an ideal BGS), $B(\mathbf{y})$ is the longitudinal envelope function (with $B(\mathbf{y})$ = constant, for an ideal BGS), i is the imaginary unit ($\mathrm{i}^2 = -1$), and t is time. Note that this expression will also describe a conventional guided mode if either A_{r} or A_{l} is zero. For a perfect cylinder ($\delta = 0$), the Mie and BGS modes are orthogonal and incapable of coupling to one another. For a GSL ($\delta > 0$), we consider a non-zero coupling frequency, ω_{c}, between a Mie resonance centered at ω_{m} and a BGS centered at ω_{g}. For normal incidence illumination, the coupling is non-zero only for the ω_{g} with a $\mathbf{k}_{\mathrm{g,L}}$ that matches the geometrically defined p(i.e., $\mathbf{k}_{\mathrm{g,L}} = 2\pi m/p$, where m = 1, 3, 5, . . .) because these frequencies experience coherent amplification whereas mismatched ones vanish. Thus, the structure behaves as a Fourier selector in which only the spatial frequency components, including higher mth order odd harmonics (Figure 4.2), matched to the structure are coupled to a BGS.

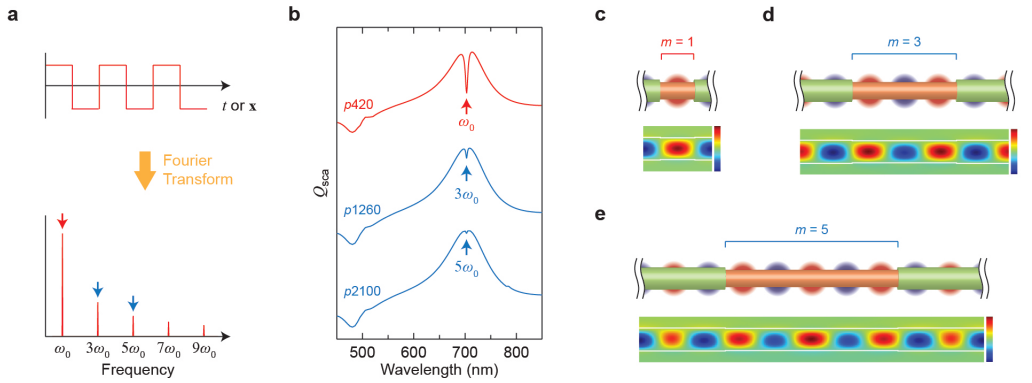

Figure 4.2: Fourier selection of BGS by higher harmonics. **a** A square wave representing a GSL structure and its Fourier series that consists of odd-numbered harmonics of the fundamental frequency. **b** Q_{sca} spectrum of NW GSLs with d = 140 nm and e = 135 nm of three different values of p = 420 nm (top), p = 1260 nm (middle) and p = 2100 nm (bottom). Pitch was varied to tailor higher harmonic interactions with a Mie resonance fixed at the same wavelength. **c–e** Schematic and calculated magnetic field profiles for the GSLs in panel **b** at the dip, showing a BGS mode with m = 1 (**c**), m = 3 (**d**) and m = 5 (**e**) antinodes confined at each segment.

Figure 4.1c shows numerically calculated scattering efficiency (Q_{sca}, see Methods for details) spectra (solid lines) and analytically calculated spectra (dashed lines) derived from temporal coupled-mode theory (TCMT)[122,131] for a uniform NW (labeled $p\infty$) and three NW GSLs of varying p. The dominant peak in the uniform NW spectrum corresponds to the fundamental TM_{11} magnetic dipolar Mie resonance (directly related to the HE_{11} guided mode[48]) centered at ω_{m}. For the GSL, in contrast, a sharp and pronounced scattering dip (labeled ω_{g} for p420) is observed within the Mie resonance. The calculated field profile at ω_{g} (Figure 4.1f) exhibits a standing wave with antinodes centered on each cylindrical segment (see also a time-lapsed animation in Supplementary Movie 1). This standing wave profile corresponds to the BGS. For shorter (p360) and longer (p500) values of p, the scattering dip shifts to the blue or red of ω_{m}, respectively; nevertheless, the same standing wave profile is observed at the scattering dip for all values of p (Figure 4.3). The peaks to the blue and red of the scattering dip in Figure 4.1c (labeled ω_+ and ω_-, respectively, for p420) exhibit mode profiles (Figure 4.1d, e) with antinodes centered only on the small or large diameter segments, respectively, and these profiles are also preserved for every value of p (Figure 4.3). Substantially larger values of p shift ω_{g} off the Mie resonance envelope, causing the scattering dip to disappear and no power to

be transferred to the BGS (Figure 4.4). In addition, a tilt of the incoming plane wave provides a non-zero momentum along the NW axis, causing the BGS scattering dip to split into two separate dips dominated by a right- and left-propagating BGS state (Figure 4.5); however, we focus only on normal incidence illumination in this study.

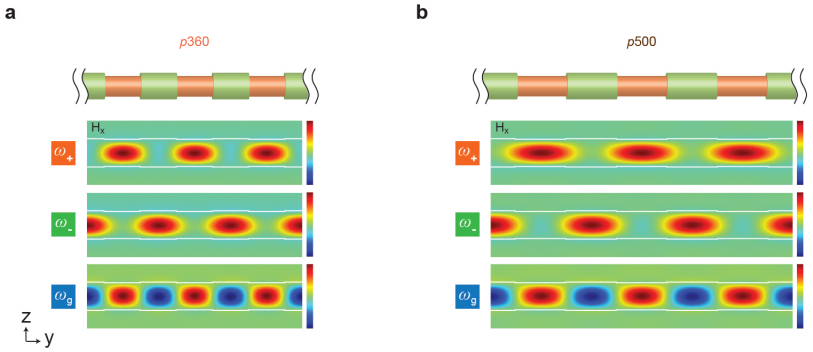

Figure 4.3: Calculated Magnetic Field Profiles of a GSL with varying pitch. **a-b**, Schematic and calculated magnetic field profiles for a GSL with p = 360 nm (**a**) and p = 500 nm (**b**) from Figure 4.1c, showing coupled TM_{11} dipolar modes appearing in small diameter regions (ω_+, top) and large diameter regions (ω_-, middle), and a standing wave as a superposition of counter-propagating HE_{11} guided modes (ω_g, bottom).

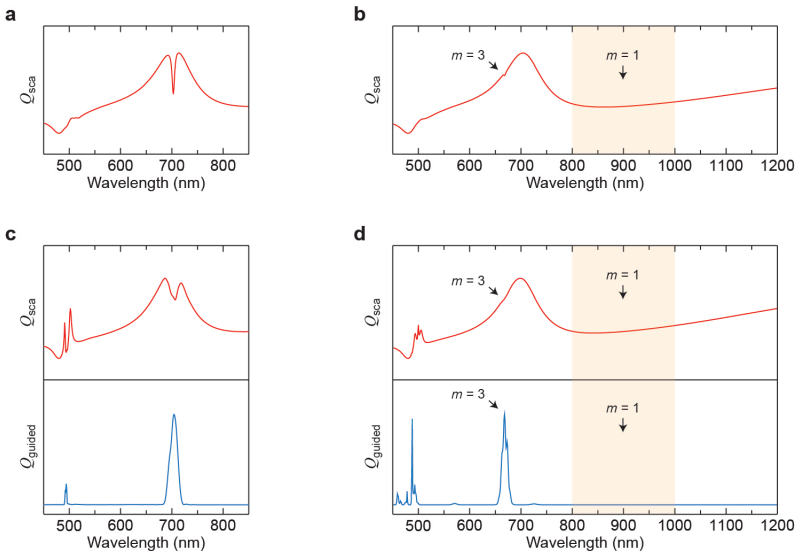

Figure 4.4: Disappearance of BGS coupling at long pitch values outside the Mie resonance envelope. **a-b** Simulated Q_{sca} spectra with d = 140 nm and e = 135 nm for an onresonance p = 420 nm (**a**) and an off-resonance p = 1000 nm (**b**) NW GSL under plane wave illumination. A scattering dip is not observed for p = 1000 nm in the shaded region of the spectrum where the first-order (m = 1) BGS is expected, but the third-order (m = 3) mode appears at ∼668 nm. **c-d**, Simulated Q_{sca} spectra (upper graphs) and Q_{guided} spectra (lower graphs) for an on resonance p = 420 nm (**c**) and an off-resonance p = 1000 nm (**d**) GSL-WG under illumination with a Gaussian beam. For the off-resonance structure (panel **d**), no guided power is observed in the shaded region of the spectrum where the first-order (m = 1) BGS is expected, but guided power from the third-order (m = 3) mode appears at ∼668 nm.

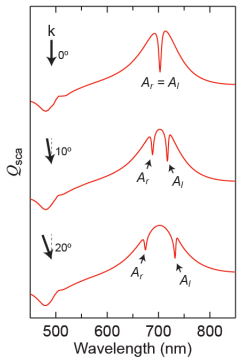

Figure 4.5: Incident angle dependence of BGS coupling. Simulated Q_{sca} spectra of a NW GSL with d = 140 nm, e = 135 nm, and p = 420 nm under plane wave illumination at 0° (upper), 10° (middle), and 20° (bottom) with respect to the normal, showing a splitting of the BGS into primarily right-propagating (A_{r}) and left-propagating (A_{l}) BGS modes.

The features of the Mie-BGS coupling can be accounted for using TCMT.[122,131] The dynamic state of the resonance amplitudes can be expressed as:

$$\frac{d}{dt}\begin{pmatrix} A_{\text{m}} \\ A_{\text{g}} \end{pmatrix} = \left[-i \begin{pmatrix} \omega_{\text{m}} & \omega_{\text{c}} \\ \omega_{\text{c}} & \omega_{\text{g}} \end{pmatrix} - \begin{pmatrix} \gamma_{\text{m}} & 0 \\ 0 & \gamma_{\text{g}} \end{pmatrix} \right] \begin{pmatrix} A_{\text{m}} \\ A_{\text{g}} \end{pmatrix} + \begin{pmatrix} k_{\text{m}} \\ 0 \end{pmatrix} S_{+} \tag{4.1}$$

where A_{m} is the Mie resonance amplitude, γ_{m} and γ_{g} are radiative decay rates for the Mie resonance and BGS, S_{+} is the incoming wave, and k_{m} is the coupling coefficient to the incoming wave. Here, we have neglected absorptive contributions and neglected an off-diagonal radiative coupling term, γ_{c}. The outgoing wave, S_{-}, can be expressed as $S_{-} = S_{+} + d_{\text{m}}A_{\text{m}}$, where d_{m} is the coupling coefficient to the outgoing wave. The coupling coefficients of the BGS to the incoming and outgoing waves are set to zero under normal incidence illumination, which assumes that γ_{g} is small compared to γ_{m}. In a perfectly cylindrical NW geometry (δ = 0), coupling between the Mie resonance and BGS does not occur, and ω_{c} and γ_{g} are both zero, leaving both resonances unaffected and the BGS completely dark. However, in the case of a NW GSL, both parameters are non-zero, and scattering cross-sections calculated using Eq. (4.1) are plotted in Figure 4.1c as dotted lines. Analytical parameters are summarized in Table 4.1 and were determined by a fit to the numerical simulation considering energy conservation and time reversal symmetry,[122] reproducing the spectral features in the numerical results. Note that the scattering dip does not go to zero because of the introduction of loss in the

guided mode ($\gamma_g > 0$; see Figure 4.6). The good agreement of numerical and TCMT results validates the assignment of the scattering dip as a scattering dark state resulting from coupling between a Mie resonance and BGS. Similar calculations with different geometrical parameters (Figure 4.7) show that the effect is fully tunable from visible through infrared wavelengths by changing d and p with a fixed δ.

	λ_m (nm)	λ_g (nm)	ω_m (THz)	ω_g (THz)	ω_c (THz)	γ_m (THz)	γ_g (THz)
$p\infty$	700	1000	2691	1884	–[a]	177	–[a]
$p360$	700	680	2691	2770	24	179	5.4
$p420$	700	703	2691	2679	30	179	5.4
$p500$	700	726	2691	2595	30	179	4.5

[a] Any arbitrary value can be chosen

Table 4.1: Parameters used in the TCMT for fitting Q_{sca} spectra in Figure 4.1c.

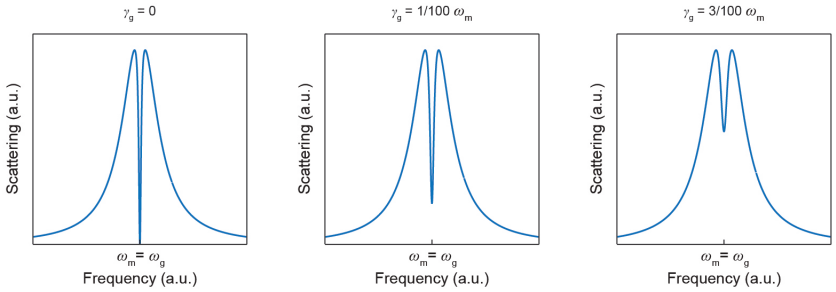

Figure 4.6: Schematic plots of Mie-BGS coupling with and without γ_g. Schematic scattering plots for $\omega_m = \omega_g$ when γ_g is zero (left), 1/100 ω_m (middle) and 3/100 ω_m (right).

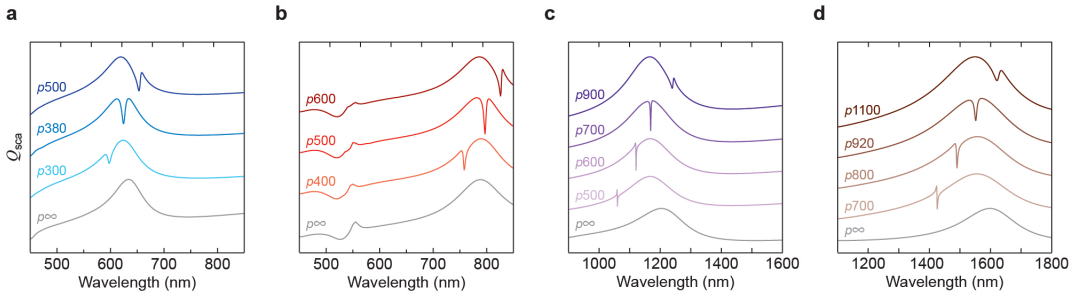

Figure 4.7: Diameter dependence and spectral tunability of Mie-BGS coupling. Simulated Q_{sca} spectra of GSLs of selected pitches with d = 120 nm, e = 115 nm (**a**), d = 160 nm, e = 155 nm (**b**), d = 250 nm, e = 245 nm (**c**), and d = 340 nm, e = 330 nm (**d**).

Diagonalization of the energy matrix in Eq. (4.1) yields eigenfrequencies, ω_+ and ω_-, and the eigenmodes, A_+ and A_-. If the scattering dip appears at the center of the Mie resonance ($\omega_m = \omega_g$; red curve in Figure 4.1c), the eigenmodes are $A_\pm = A_m \pm A_g$, where Am corresponds to a dipolar Mie resonance uniformly distributed across the axial length of the NW, and A_g is the standing-wave mode profile of the BGS. The eigenmodes A_+ and A_- thus represent interference between the Mie resonance and BGS, in which the axially uniform amplitude of the Mie resonance overpowers the oscillating amplitude of the BGS with a relative phase shift of π for the two eigenmodes. This result corresponds to the numerically calculated mode profiles in Figure 4.1d, e for the adjacent peaks on the blue (ω_+) and red (ω_-) sides of the scattering dip. This eigenmode analysis can also justify the assignment of the scattering dip as a Fano resonance arising from the interaction between a sharp BGS and a broad Mie background resonance.

The bound character of the BGS is apparent if we consider the effect of the modulation depth, δ. Numerical simulations (Figure 4.8) with δ ranging from 20 to 2 nm show a marked narrowing of the scattering dark state linewidth and increase of the quality factor, extrapolating to infinity as δ approaches zero. Moreover, ω_c decreases as δ decreases in magnitude (Table 4.2) because access to the bound state vanishes. In contrast, as δ increases in magnitude, the linewidth significantly broadens and eventually bifurcates into two distinct peaks that align with the positions of ω_+ and ω_-. This transition occurs because the Mie resonance and BGS are no longer weakly coupled, and instead two qualitatively new modes arise that are more representative of scattering from Si NW segments of distinct diameters.

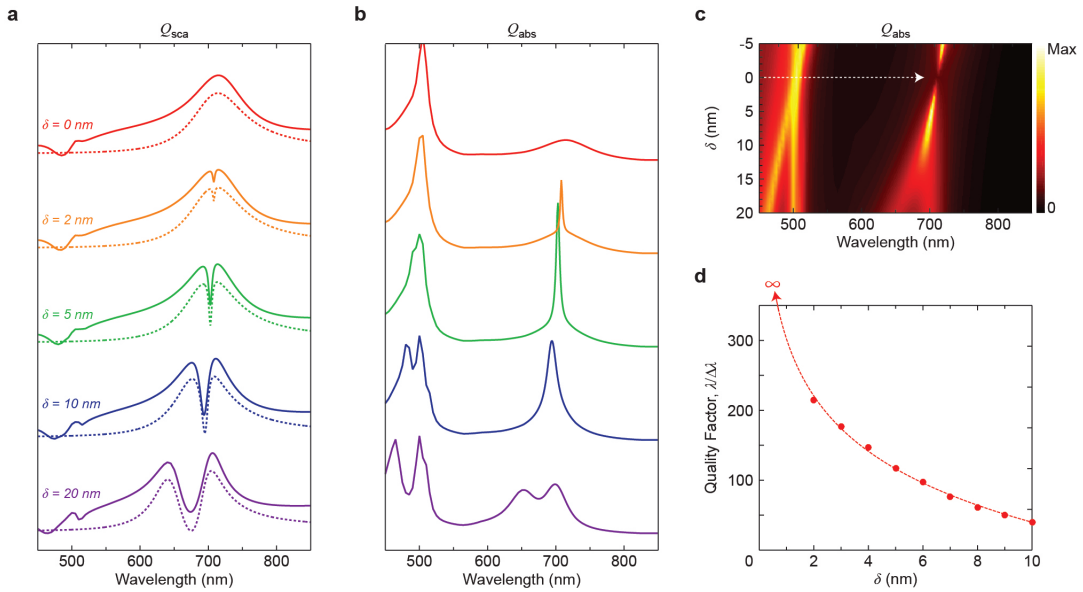

Figure 4.8: Effect of modulation depth on bound character of the BGS. **a** Numerically calculated Q_{sca} spectra (solid lines) and analytical fit by TCMT (dotted lines) for a NW GSL with d = 140 nm, p = 420 nm and varying δ of 0, 2, 5, 10, and 20 nm. δ = 0 nm corresponds to a NW with uniform diameter. Parameters for TCMT spectra are provided in Table 4.2. **b** Numerically calculated Q_{abs} spectra of GSLs from panel **a**, showing a broad background peak for δ = 0 nm and appearance of a high-quality factor absorption peak for non-zero δ that eventually bifurcates into two peaks at $\delta > 15$ nm. **c** Two-dimensional Q_{sca} heat map with vertical and horizontal axes for δ and wavelength, respectively, showing a vanishing point at δ = 0 nm that corresponds to a completely bound guided state (BGS). **d** Quality factor ($\lambda/\Delta\lambda$) calculated from the fit parameters (Table 4.2) used panel **b** plotted against δ, which extrapolates to infinity as δ approaches zero.

δ (nm)	λ_m (nm)	λ_g (nm)	ω_m (THz)	ω_g (THz)	ω_c (THz)	γ_m (THz)	γ_g (THz)
0	711	–[a]	–[a]	–[a]	0	177	–[a]
2	707	708	2664	2661	12	178	5.3
5	700	703	2691	2679	30	179	5.4
10	687	695	2742	2710	55	183	5.5
20	665	675	2833	2791	129	189	5.7

[a] Any arbitrary value can be chosen

Table 4.2: Parameters used in the TCMT for fitting Q_{sca} spectra in Supplementary Figure 4.8.

To experimentally verify the predicted optical properties of NW GSLs, a process termed ENGRAVE (Encoded Nanowire GRowth and Appearance through VLS and Etching)[22,29,68] was used to fabricate Si NW GSL nanostructures from the bottom-up using a gold (Au) nanoparticle catalyzed vapor-liquid-solid (VLS) growth process. VLS growth produces single-crystalline NWs and is capable of precise size control and on-demand modification of morphology,[22,27,29,71,132] chemical composition,[12] and crystal phase.[24] Of the geometric parameters, p is determined by the dopant switching frequency during the growth, and d and e are determined by the size of Au catalyst and post-growth etch duration, respectively. Optimized growth conditions without Au loss from the catalyst[133] yield NWs exceeding 500 μm in length with no undesired diameter variation (Figure 4.9). Figure 4.10a–c shows scanning electron microscope (SEM) images of three distinct NW GSLs with increasing diameters d prepared by the ENGRAVE process using etch depths of δ = 10–25 nm. Geometrical parameters of each GSL were determined by quantitative image analysis.[68] For optical characterization, a home-built laser microscope (Figure 2.1) capable of polarization-resolved bright-field extinction measurements using a supercontinuum laser source and balanced detection was employed.

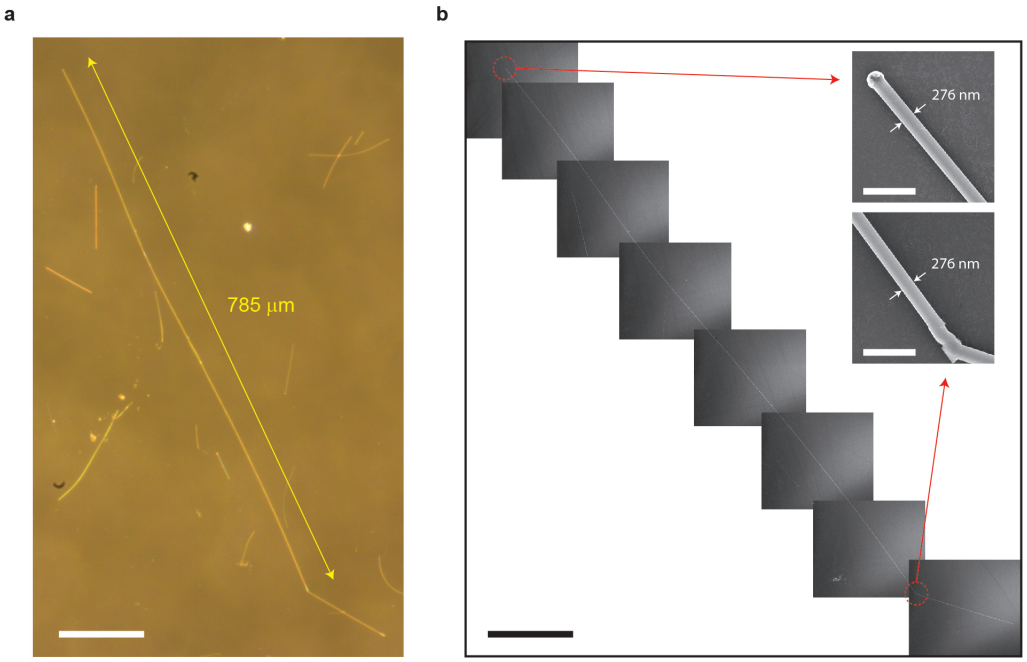

Figure 4.9: NW with length of nearly 1 mm with no variation in diameter. **a-b**, Optical (**a**) and SEM (**b**) images of a NW exhibiting no diameter variation over nearly 1 mm; scale bars, 100 µm. Insets: Magnified views at each end of a straight portion of the NW; scale bars, 1 µm.

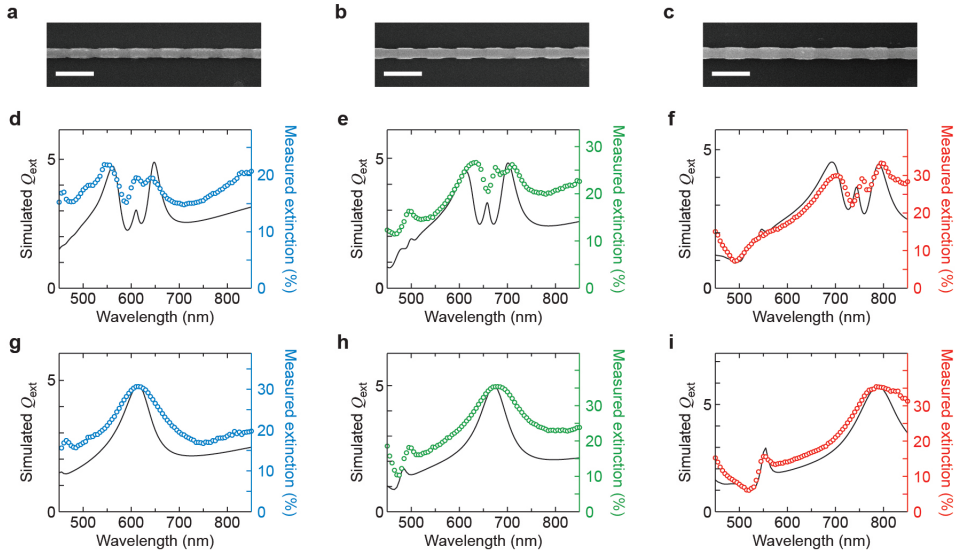

Figure 4.10: Experimental extinction spectra of NW GSLs. **ac** SEM images of three NW GSL with geometrical parameters of d = 130 $\pm$ 1 nm, e = 114 $\pm$ 1 nm, p = 397 $\pm$ 10 nm (**a**), d = 145 $\pm$ 1 nm, e = 119 $\pm$ 5 nm, p = 383 $\pm$ 9 nm (**b**), and d = 158 $\pm$ 1 nm, e = 134 $\pm$ 2 nm, p = 465 $\pm$ 10 nm (**c**); scale bars, 500 nm. Duty cycles for NW GSLs used in panels ac in Figure were calculated to be 50 $\pm$ 2 %, 50 $\pm$ 2 %, 49 $\pm$ 2 %, respectively, indicating that the length of segments in each GSL is p/2 within $\sim$1 %. **d-i** Extinction spectra of NW GSLs (**d-f**) and of uniform NWs of the same diameters (**g-i**), showing experimentally measured extinction (colored circles and right-hand axes) and numerically simulated Q_{ext} (black lines and left-hand axes). Spectra in **d-f** correspond to the images in **a-c**, respectively.

Experimental extinction spectra, plotted as (1 - T) $\times$ 100%, where T is the measured transmittance (see Methods), are shown in Figure 4.10d-i for GSLs (Figure 4.10d-f) and uniform NWs of the same diameters (Figure 4.10g-i). Each spectrum shows a broad Mie resonance that shifts to longer wavelengths with increasing diameter. For the GSLs, sharp spectral features deviating from the background Mie resonances are observed. Numerical simulations (black solid lines) of the extinction efficiency (Q_{ext}) that use geometrical parameters obtained from the SEM images and include the focused laser beam (see Methods) agree well with the experimental measurements, confirming the presence of Mie-BGS coupling and a scattering dark state in these nanostructures. However, the simulations also reveal several differences between focused excitation and the plane wave excitation modeled in Figure 4.1. First, the simulations predict a scattering dip with a substantially larger linewidth, which can be attributed to the localized excitation causing a broader

distribution of Fourier spatial components to couple to the BGS. Second, the simulations predict an extinction peak within the dip, which can be attributed to mode distortion caused by the finite number of GSL periods excited by the focused beam. Mode degradation in truncated arrays is a common phenomenon observed in planar metamaterials due to loss of coherence. [134,135] In our case, the finite beam prevents the Bloch condition along the GSL from being satisfied, causing incomplete formation of the BGS and an increase in scattering loss, manifesting as a peak within the scattering dip (Figure 4.11).

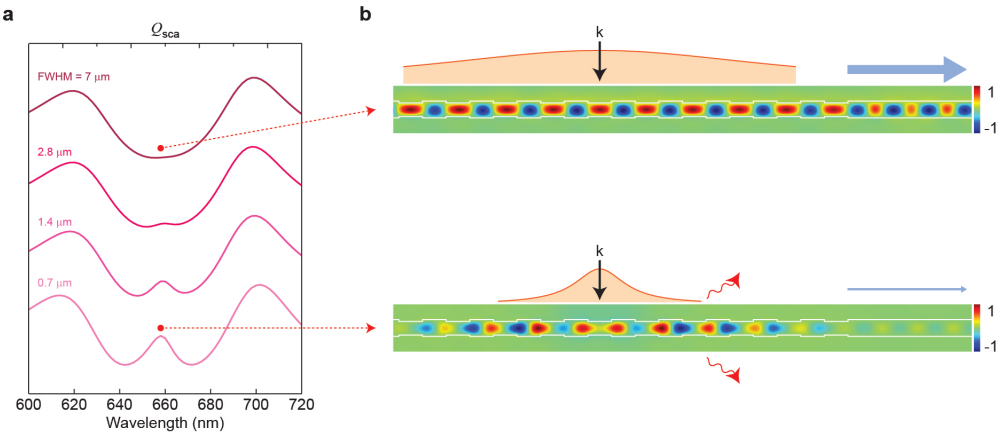

Figure 4.11: Effect of Gaussian beam width. **a** Q_{sca} spectra around the scattering dip region of a GSL with d = 140 nm, e = 115 nm and p = 400 nm under focused Gaussian illumination of varying width. Each spectrum is labeled with its Gaussian full-width at half maximum. Absorptive loss is artificially turned off to only account for scattering characteristics. **b** Calculated magnetic field snapshots at marked locations from panel **a** and Supplementary Movie 3-4, showing coherent coupling to the BGS under a large beam (top) and radiative loss under a small beam (bottom).

4.2.2 Tunable guiding in a GSL-WG NW

The geometric dependence of Mie-BGS coupling, as observed in Figure 4.10, can be predicted from the dispersion relation for the WG modes of a uniform diameter Si NW (Figure 4.12a) and the diameter dependence of the TM_{11} Mie resonance. For a fixed longitudinal wavevector $\mathbf{k}_{g,L}$, which corresponds to a GSL satisfying $p = 2\pi m/\mathbf{k}_{g,L}$, the frequency of the guided mode decreases with increasing diameter, and the Mie resonance frequency similarly decreases with increasing diameter. However, because the frequencies of the Mie resonance and BGS change with diameter at different rates, the pitch p required to center the BGS on

the Mie resonance shifts to larger values as the diameter of the NW increases and the frequency decreases. In Figure 4.12a, this shift can be visualized as the intersection of the solid lines (BGS dispersion relation) with the magenta dashed line (Mie resonance position), which represents the degenerate point where $\omega_m = \omega_g$ and provides a guideline for the geometric design of a GSL to enable optimal Mie-BGS coupling at a given free-space wavelength. Magenta diamonds and black circles represent data points where the modes are and are not degenerate, respectively, as determined from numerical simulations of NW GSL spectra in Figure 4.1c and Figure 4.7. The good alignment of these data points with the dispersion relations confirms the geometric relationship between d and p for Mie-BGS coupling.

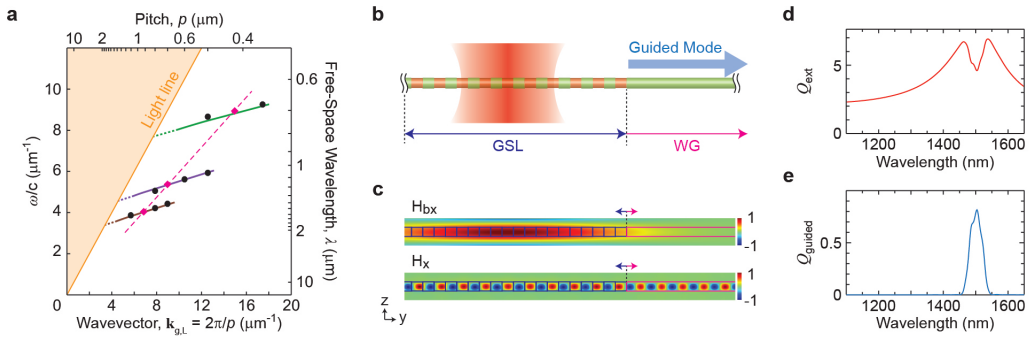

Figure 4.12: Selective excitation of guided modes through a NW GSL. **a** Dispersion curves (solid lines) of fundamental HE_{11} guided modes in infinitely long NWs with d = 140 nm (green), d = 250 nm (purple), and d = 340 nm (brown). Marker symbols denote the positions of scattering dark states that are centered on a Mie resonance (magenta diamonds) or off-center from a Mie resonance (black circles). Magenta dashed line represents the frequency of a BGS that is centered on a Mie resonance for each value of d, so the intersection of solid and dashed lines represents the condition $\omega_m = \omega_g$. **b** Structure and excitation geometry of a NW GSL connected to a NW WG. **c** Calculated magnetic field profiles of an incoming Gaussian beam background field, H_{bx}, (top) and an excited mode scattered field, H_x, (bottom) of a NW GSL with d = 330 nm, e = 310 nm and p = 900 nm, and 10 periods, showing propagation from the GSL into the WG. **d, e** Simulated Q_{ext} (**d**) and Q_{guided} (**e**) spectra corresponding to the structure in **b** and **c**.

To take advantage of the WG characteristics, we designed a GSL-WG NW, illustrated in Figure 4.12b, composed of a truncated GSL adjacent to a long, uniform cylindrical segment that can act as a lossless WG. The geometric parameters of the GSL were designed to support Mie-BGS coupling in the near-infrared

spectral region to avoid absorptive losses in Si. Numerical simulations for a GSL (d = 330 nm; e = 310 nm; p = 900 nm) with 10 periods of the pitch illuminated by a focused laser beam (Figure 4.12c) yield an extinction spectrum (Figure 4.12d) with a broad Mie resonance centered at ∼1500 nm and an extinction dip centered at ∼1504 nm. A Mie-BGS coupled excitation occurs at the dip, and the numerical simulations show energy propagation into the guided mode of the WG segment adjacent to the GSL, as shown by the magnetic field profile in Figure 4.12c and Supplementary Movie 2. Integration of the energy flux in the WG portion of the NW yields the guided spectrum shown in Figure 4.12e. As expected, the spectral region guided in the NW corresponds to the spectral region of the dip in the extinction spectrum. The guided bandwidth of ∼46 nm is in good agreement with the expected Fourier-transform-limited bandwidth of 48 nm for a Gaussian beam with a full-width at half maximum of 7 μm. Moreover, we calculate a maximum guided efficiency (Q_{guided}) of 0.82 for coupling into the WG based on the ratio of the power measured at the end of the WG to the power incident on the projected area of the GSL. Thus, the near-unity Q_{guided} highlights the high efficiency with which the Mie-BGS coupling mechanism can funnel the energy associated with the strong light-matter interaction of the Mie resonance into the guided mode of a NW.

To experimentally validate the expected guiding characteristics of a GSL-WG NW, we synthesized NWs with a GSL adjacent to a 50 μm WG segment, as illustrated in Figure 4.13a. Geometric parameters of the NW were chosen to support lossless guiding at frequencies below the bandgap of Si. Because of infrared free carrier absorption losses in heavily-doped n-type Si NWs,[136] we adopted the doping-inverted ENGRAVE process[29,133] in which n-type rather than intrinsic segments are etched (see Methods), allowing the WG segment to be composed of intrinsic Si. To experimentally measure guiding in the GSL-WG structure, an excitation beam was focused on the GSL segment, and optical images were collected to observe any light emission from the end of the WG segment, where light is expected to scatter after traversing the 50 μm WG. Figure 4.13c-e displays optical images of a GSL-WG structure illuminated at three excitation wavelengths. As apparent from these images, WG light emission is observed from the end of the WG segment for an excitation wavelength of 1455 nm but is not observed at wavelengths of 1400 and 1550 nm.

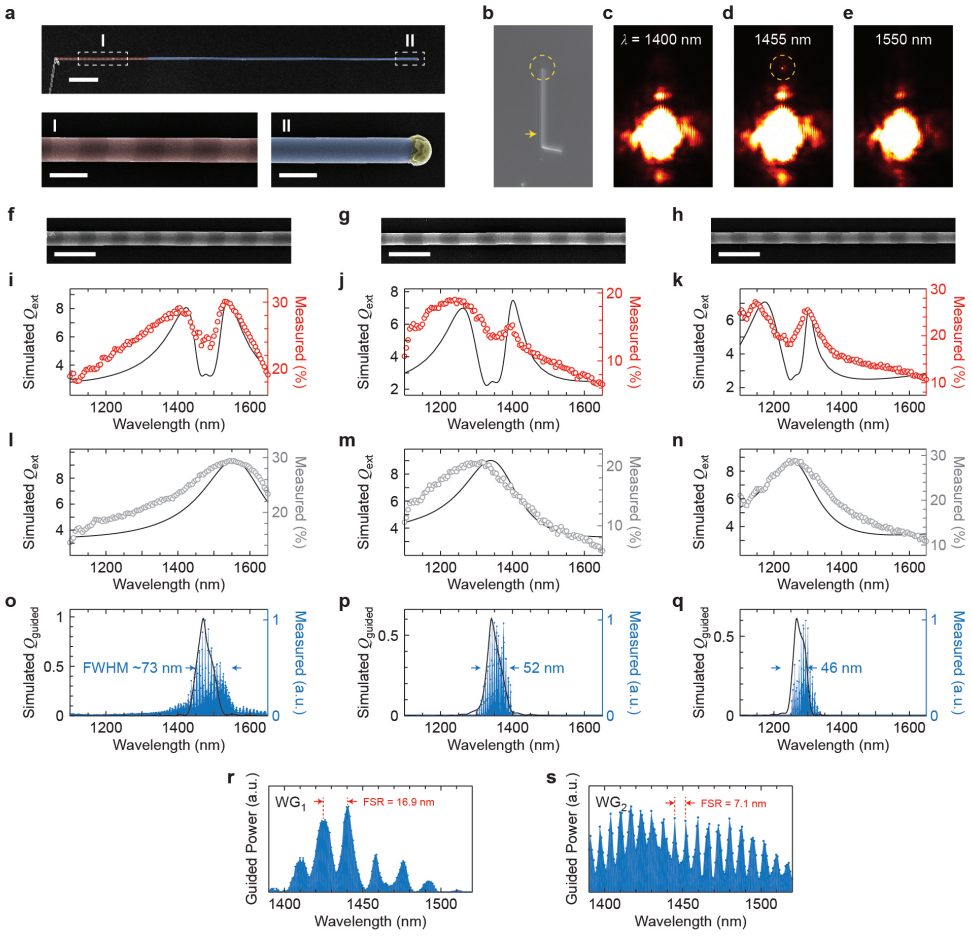

Figure 4.13: Experimental validation of tunable, narrow-band guiding by NW GSLs. **a** (Top) False-colored SEM image of a NW GSL (red) with $d = 334 \pm 1$ nm and $p = 781 \pm 9$ nm prepared by the doping-inverted ENGRAVE process followed by a 50 µm-long NW WG (blue); scale bar: 5 µm. (Bottom) Magnified views of dotted regions in the top image; scale bars: 500 nm. **be** False-colored optical images of the NW from a without an excitation beam (**b**) and under excitation at wavelengths of 1400 nm (**c**), 1455 nm (**d**), and 1550 nm (**e**). Yellow arrow and circles denote locations of the excitation beam and the NW tip, respectively. **fh** SEM images of GSLs with geometrical parameters of $d = 334 \pm 1$ nm, $p = 781 \pm 9$ nm (**f**), $d = 284 \pm 3$ nm, $p = 882 \pm 6$ nm (**g**), $d = 266 \pm 1$ nm, $p = 772 \pm 6$ nm (**h**); scale bars, 1 µm. **iq** Spectra of GSL extinction (**ik**), NW WG extinction (**ln**), and WG emission (**oq**). Experimental measurements (right-hand axes) are shown as circles (and blue shaded area for guided spectra), and simulated spectra (left-hand axes) are shown as black lines. **rs** Fabry-Perot patterns in guided power spectra for NW WGs with length of 21 µm (**r**, WG_1) and 53 µm (**s**, WG_2)

Extinction spectra were collected from both GSL and WG segments of NWs with three distinct geometric parameters (Figure 4.13i-n) designed to tune the Mie-BGS coupling from $\sim$1300 to $\sim$1500 nm. As expected, the uniform-diameter WG segments show one Mie resonance whereas the GSL segments show a scattering dark state within the Mie resonance. WG emission spectra, as shown in Figure 4.13o-q, were also experimentally measured by integrating the signal from the end of the WGs (e.g., from the region denoted by a dashed circle in Figure 4.13b). The WG emission spectra show that guiding occurs over a select wavelength range that corresponds to the spectral position of the scattering dip in the extinction spectra. The WG spectrum in Figure 4.13o was collected from the same NW imaged in Figure 4.13b, and the spectrum shows maximal WG intensity in the 1450-1500 nm range, in agreement with the images in Figure 4.13c-e. Simulations of Q_{ext} and Q_{guided} spectra are shown as solid black lines in Figure 4.13i-q and agree well with experimental measurements, confirming the Fourier-selected guiding characteristics of the GSL-WG NW system. Q_{guided} ranges from 0.5 to 1.0 depending on the choice of geometrical parameters.

Interestingly, the guiding spectra exhibit a high frequency oscillation (Figure 4.13o-q), which indicates that the WG acts as a Fabry-Perot cavity. To confirm this effect, we prepared a single GSL with WG segments of two different lengths on either side (Figure 4.14). WG emission was observed from the ends of both WGs, and spectra collected from each end (Figure 4.13r-s) show free spectral ranges (FSRs) of 16.9 and 7.1 nm as well as finesse values of 1.58 and 1.17 from WG_1 and WG_2, respectively. The FSRs are in good agreement with the expected values of $\sim$15 and $\sim$6 nm based on respective WG cavity lengths, and the finesse values correspond to round-trip reflectance values of 3 % and 1.2 % for WG_1 and WG_2, respectively. The appearance of this Fabry-Perot pattern confirms the high-quality and low loss of the GSL-WG system, and suggests a potential route for further spectral filtering of the guided light.

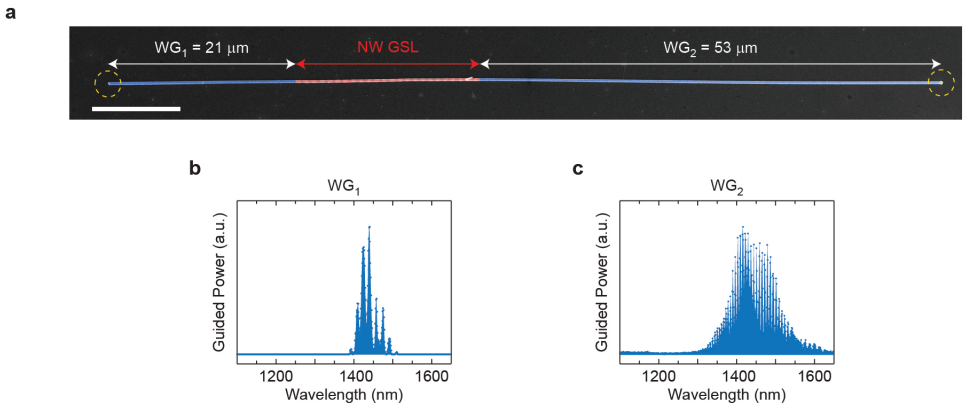

Figure 4.14: Fabry-Perot cavity free spectral ranges in WGs of different lengths. **a** A NW GSL attached to WGs at both ends in lengths of 21 and 53 μm; scale bar, 10 μm. **b-c**, Experimental guided spectra collected from WG_1 (**b**) and WG_2 (**c**).

4.2.3 Sensing and switching with a GSL-WG NW

The guiding characteristics of the GSL-WG system are sensitive not only to geometric parameters but also to the refractive index, n, of the surrounding medium, as shown schematically in Figure 4.15a. A change in n from 1 to 1.5 in steps of 0.1 refractive index units (RIUs) results in a shift of the maximal guided power by 142 nm, as shown by the simulations in Figure 4.15b, c. This large spectral shift corresponds to a sensitivity of 270 nm RIU^{-1}, which is comparable to the sensitivity of planar dielectric metasurface sensors [134] and suggests potential applications of the GSL system in both sensing [134] and optical switching. [137] Figure 4.15d shows the progressive change in guided power as a function of n at three select wavelengths, exemplifying the sensing and on/off switching characteristic that can be achieved at each wavelength by relatively small changes in n. However, in comparison to typical microresonators and planar metasurfaces, the finite length and nanoscale dimensions of the NW GSL cause a relatively low quality factor and wide bandwidth for the guided light. This difference highlights an inherent but common tradeoff in the design of optical components in the nanoscale regime; nevertheless, several index-changing strategies, such as the electro-optic effect [138,139] and photoisomerization, [140] offer sufficiently large index modulation to enable switching in the NW GSL-WG system.

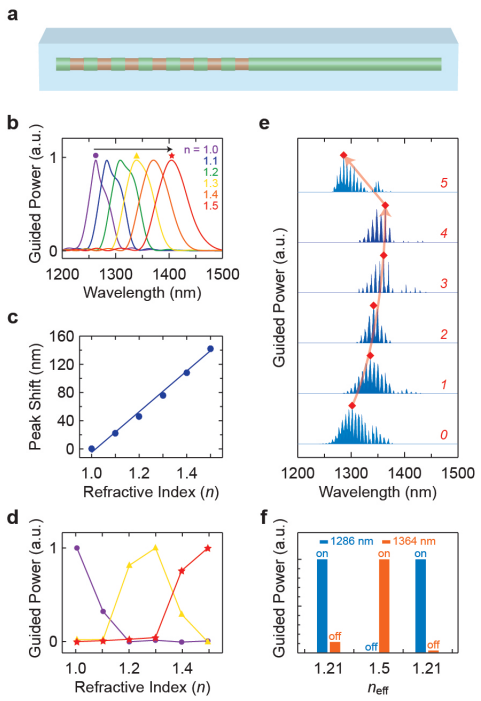

Figure 4.15: Optical switching in a GSL-WG. **a** Schematic of a GSL-WG in which the refractive index, n, of the surrounding medium (blue) changes from 1 to 1.5. **b** Simulated guided power spectra for a GSL-WG with d = 280 nm, e = 250 nm, and p = 800 nm for n varying from 1 (blue) to 1.5 (red) in steps of 0.1. **c** Plot of guided peak position shift versus refractive index n. **d** Normalized guided power versus refractive index at wavelengths of 1262 nm (purple circles), 1338 nm (yellow triangles), and 1404 nm (red stars). Spectral positions correspond to the marker symbols in **b**. **e** Experimental guided power spectra of a NW WG with a GSL of d = 280 nm and p = 820 nm measured without PMMA (0), after sequential additions of up to 4 PMMA layers (1-4), and after removal of PMMA (5). Red diamonds and lines denote the spectral position with maximal guided power for each spectrum. **f** Normalized guided power at wavelengths of 1286 and 1364 nm derived from spectra labeled 0, 4, and 5 in **e**, which correspond to estimated effective indices of 1.21, 1.5, and 1.21, respectively

We experimentally demonstrate reversible, passive sensing, and optical switching by sequentially adding up to 4 poly(methyl methacrylate) (PMMA) layers over a NW GSL-WG on a SiO_2 glass substrate. Each successive PMMA layer increases the effective index of the environment. As shown by the guided spectra in Figure 4.15e, the PMMA layers induce up to a 78 nm spectral shift of the maximum guided power, from 1286 to 1364 nm. This shift corresponds to a change of the effective refractive index (n_{eff}) of ~0.29 RIU,

from 1.21 to 1.50, which is approximately the expected change considering the fixed n of the substrate. Moreover, the spectrum reverts to its original position upon removal of all PMMA layers, thus demonstrating that the process is reversible. Figure 4.15f shows the relative guided power measured at wavelengths of 1286 and 1364 nm as a function of n_{eff}. The data exemplifies the expected sensing and optical switching behavior of the GSL-WG system, allowing the guiding of a specific wavelength to be modulated and even turned on and off by the choice of n_{eff}.

4.3 Conclusion

In conclusion, we have demonstrated that periodic geometric perturbation of a NW allows coupling of a Mie resonance and a BGS. The coupling creates a pronounced dip in scattering spectra as predicted by both numerical finite-element modeling and analytical modeling using TCMT. The periodic GSL structure acts as a Fourier frequency selector to determine the wavelength of the BGS to be coupled with the Mie resonance. The effect can be readily tuned from visible through near-infrared wavelengths by controlling geometric parameters, as proven by experimental measurements of extinction of individual GSL NWs. We demonstrate selective, Fourier-transform-limited guiding of light up to telecommunication wavelengths with near-unity coupling efficiency, highlighting the unique ability of the Mie-BGS coupling mechanism to direct energy from the strong Mie resonance light-matter interaction into a NW WG. We also demonstrate a simple optical switch that takes advantage of the spectral sensitivity of the coupled wavelength to the surrounding medium. The Mie-BGS light coupling mechanism thus offers a new platform for controlled light management when designing optical circuits.

OPTICAL BOUND STATES IN THE CONTINUUM WITH NANOWIRE GEOMETRIC SUPERLATTICES

5.1 Introduction

Trapping light in subwavelength structures is of utmost importance in wave physics [118,141,142] and central to a wide range of photonic and optoelectronic applications [45,143–145]. Localized optical modes with infinite lifetimes, namely optical bound states in the continuum (BICs), can exist in the radiation continuum, and they have been described in one-dimensional (1D) arrays of coupled waveguides [146–148] and two-dimensional (2D) photonic crystals (PCs) [118,149,150]. Despite the subwavelength size of each optical resonator unit cell, however, BIC structures require infinite periodicity to formally satisfy the BIC condition [118], necessitating macroscopic quasi-infinite planar structures for experimental realization of both the 1D array and 2D PC examples. To reduce the physical dimensions of BIC cavities, recent theoretical studies have investigated the presence of BICs in 1D structures with lateral 2D confinement, such as 1D arrays of dielectric spheres [151,152] or disks [64,153], as well as supercavity modes in individual dielectric nanorods [154,155]. Optical BICs in these examples are reported to exist because of symmetry mismatch, accidental decoupling [64,151], or topological protection [152]. Although a detuned quasi-BIC has been observed in the microwave regime from a chain of millimeter-sized ceramics [156], experimental demonstration of BICs in the optical regime with laterally-confined 1D nanostructures has to our knowledge not been reported.

In this letter, we describe the perfect trapping of light in single Si nanowire (NW) geometric superlattices (GSLs) through BICs above the light cone. A NW GSL has a subwavelength diameter that is periodically modulated along the NW axis [22,29,157], as shown in Fig. 5.1(a). The optical confinement defined by the NW diameter gives rise to well-defined, strong Mie resonances [6,33,34], allowing NWs to strongly interact with external plane waves. Moreover, a NW GSL exhibits an additional set of unique photonic modes that

[3] Portions of this chapter reproduced with permission from Kim, S.; Kim, K.-H.; Cahoon, J. F. Optical Bound States in the Continuum with Nanowire Geometric Superlattices. *submitted for publication*.

are dependent on the pitch (p), outer diameter (d), and inner diameter (e) of the GSL. As shown herein, in a NW GSL under transverse-electric (TE) polarized plane wave illumination, GSL guided resonances[158] with different orbital angular momenta[64,151] can be excited and couple to Mie resonances to produce sharp Fano resonances. For a certain set of geometric parameters, these GSL modes undergo complete destructive interference, resulting in disappearance of the Fano features and formation of optical BICs. Full wave simulations and theoretical modeling using temporal coupled-mode theory (TCMT) formulated to include Lorenz-Mie scattering theory describe the origin of Fano resonances in different angular channels and the appearance of optical BICs. We discuss the geometric parameters for which a GSL satisfies the BIC condition and verify theoretical predictions with experimental measurements on single Si NW GSLs. We expect the realization of 1D BICs in the optical regime to motivate further research into the design of cavities for lasers, sensors, etc. that can utilize this phenomenon to achieve compact, nanoscale devices.

5.2 Results and Discussion

5.2.1 Optical BICs in a NW GSL

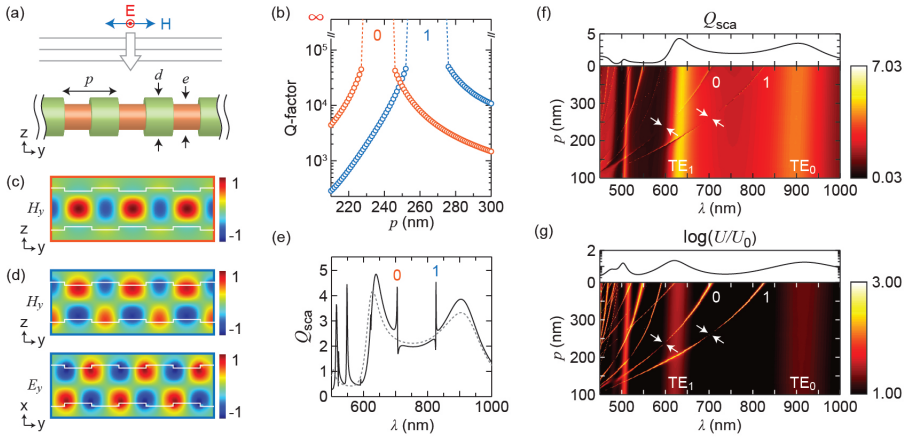

Figure 5.1: Optical BICs in a NW GSL. (a) Geometry of a NW GSL under TE-polarized plane wave illumination, where the length of each segment is $p/2$. (b) Q-factors of two GSL eigenmodes with varying p in a NW GSL with d = 200 nm, e = 170 nm. Modes are labeled with angular numbers m = 0 or m = 1. (c) H_y pattern of m = 0 GSL eigenmode. (d) H_y (upper) and E_y (lower) patterns of m = 1 GSL eigenmode. (e) Q_{sca} spectrum of a NW GSL with d = 200 nm, e = 170 nm, and p = 400 nm (solid black curve) and of a NW with d = 185 nm (gray dashed curve). (f-g) Heatmaps of Q_{sca} (f) and $\log(U/U_0)$ (g) for a NW GSL with varying p for fixed d = 200 nm and e = 170 nm. Single spectra for a uniform NW with d = 185 nm are presented on top of each heatmap.

As shown in Fig. 5.1(b), eigenmode analysis of NW GSL structures reveals GSL modes with quality factors (Q-factors) that diverge to infinity within a range of p, indicating that these GSL modes are optical bound states with infinite lifetimes. The y-component of the electromagnetic (EM) fields, H_y and E_y, of the two GSL eigenmodes are given in Fig. 5.1(c) and (d). Full EM profiles of these modes are presented in Fig. 5.2. Each GSL mode is assigned with angular numbers of m = 0 or 1 based on the azimuthal order of field maxima. In Fig. 5.1(c), the m = 0 GSL mode has a definitive TE polarization (i.e. E_y = 0; not shown), and H_y exhibits an antiferromagnetic ordering of magnetic dipoles. In contrast, the m = 1 GSL mode in Fig. 5.1(d) is hybrid-polarized, so both E_y and H_y are nonzero and must be considered. Bulgakov et al.[64,151] have categorized BICs arising in confined 1D geometries based on symmetry and propagation constant, and static

BICs may have either even or odd symmetry under inversion. Odd modes are always symmetry protected from the free-space radiation whereas even modes become decoupled from the radiation continuum only with certain geometric parameters. The m = 0 mode in Fig. 5.1(c) exhibits even symmetry and belongs to the latter case, and the BIC condition is achieved by tuning p as shown in the orange trace in Fig. 5.1(b). The m = 1 mode in Fig. 5.1(d), however, is odd in E_y but even in H_y. Thus, it is symmetry-protected against the decay into the transverse-magnetic (TM) diffraction channel but reaches the bound state only when it also decouples from the TE continuum through the proper choice of p (Fig. 5.1(b), blue trace). Previously, we reported a coupled-excitation of guided modes in a NW GSL under excitation with a transverse-magnetic (TM) polarized plane wave [157], and although those modes have a similar symmetry to the m = 1 GSL mode in Fig. 5.1(d), Fig. 5.1(c) shows that the GSL modes are not limited to the guided modes and can possess different symmetry types.

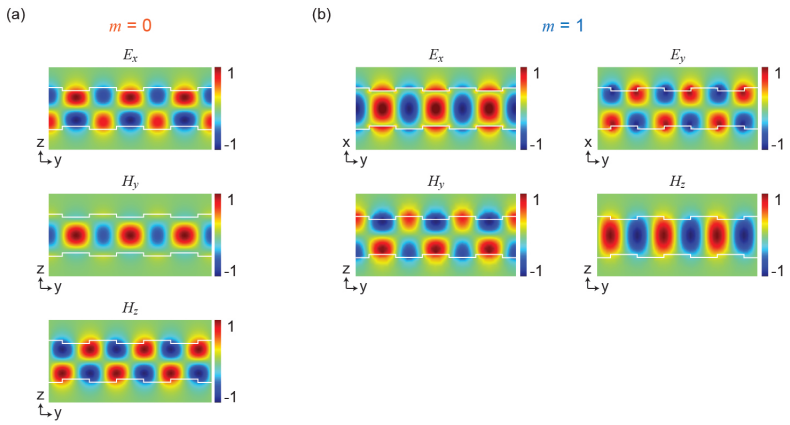

Figure 5.2: Full EM field patterns of m = 0 BIC (a) and m = 1 BIC (b).

A scattering efficiency (Q_{sca}) spectrum of a NW GSL with p = 400 nm is shown in Fig. 5.1(e) along with a reference Q_{sca} spectrum for a uniform NW. Because the value of p places the structure outside the range needed for a BIC, the Q_{sca} spectrum of the GSL exhibits two Fano resonances resulting from coupling between the GSL mode and the background Mie resonance in the same angular channel. In the Q_{sca} heatmap in Fig. 5.1(f), two sharp branches of GSL modes denoted with angular numbers m = 0 and 1 red-shift with increasing p while the background Mie resonances, denoted TE_0 and TE_1, do not shift because of the fixed diameters. The m = 0 and 1 GSL branches show vanishing points at p values of 237 and 262 nm, respectively, where the modes become completely bound. These features are more clearly observed in the heatmap of

confined energy (U/U_0) in Fig. 5.1(g). While the *p* values producing a BIC, marked with arrows in Fig. 5.1(f) and (g), fall in the ranges of infinity Q-factor for each mode in Fig. 5.1(b), the range of *p* satisfying the BIC condition are much narrower than the BIC ranges predicted by eigenmode calculations because of the directional illumination in plane wave simulations.

5.2.2 TCMT analysis of BICs

TCMT can be used to predict the optical coupling behavior in a NW GSL and has been used to interpret similar effects in photonic crystal slabs[131,158,159] and in spherical nanoparticles[122,160–162]. Here, we employ TCMT in the context of NWs by relating resonance parameters to the exact solutions of Mie coefficients[6]. For the scattering of a uniform, cylindrical NW, H_y under a TE plane wave (H_x; H_z = 0) is given by

$$H_y = \sum_{m=-\infty}^{\infty} [h_m^+ H_m^{(2)}(k\rho) + h_m^- H_m^{(1)}(k\rho)] e^{im\phi}, \tag{5.1}$$

where h_m^+ and h_m^- are amplitudes of the incoming and outgoing waves, $H_m^{(1)}$ and $H_m^{(2)}$ are the *m*th-order Hankel functions, k is a wavevector, and ρ and ϕ are the polar coordinates[162]. We define a reflection coefficient by $R_m \equiv h_m^-/h_m^+$, and a single-mode TCMT expression is given by

$$\frac{d}{dt} A_m^{Mie} = (-i\omega_m^{Mie} - \gamma_m^{Mie}) A_m^{Mie} + \kappa_m^{Mie} h_m^+, \tag{5.2}$$

with $h_m^- = h_m^+ + d_m^{Mie} A_m^{Mie}$, where A_m^{Mie}, ω_m^{Mie} and γ_m^{Mie} are the amplitude, eigenfrequency, and radiative decay rate of an *m*th-order Mie resonance, respectively, and κ_m^{Mie} and d_m^{Mie} are coupling coefficients to the incoming and outgoing plane waves, respectively. Absorptive loss is neglected for simplicity, and $\kappa_m^{Mie} = d_m^{Mie} = i\sqrt{2\gamma_m^{Mie}}$ by time-reversal symmetry [28]. The total Q_{sca} of a NW [31] is

$$Q_{\text{sca}} = \frac{2}{kr} \sum_{m=-\infty}^{\infty} \left| \frac{1 - R_m}{2} \right|^2, \tag{5.3}$$

where *r* is the NW radius. Noting the similarity of Eq. (5.3) to the Mie scattering formula, we can relate the scattering coefficient, $\left|\frac{1-R_m}{2}\right|$ in Eq. (5.3), with an exact Mie scattering coefficient[6] to yield

$$\left| \frac{1 - R_m}{2} \right| = \left| \frac{\gamma_m^{Mie}}{i(\omega - \omega_m^{Mie}) + \gamma_m^{Mie}} \right| = |a_m|, \tag{5.4}$$

where a_m is an *m*th-order electric Mie coefficient responsible for scattering of a NW under TE polarization (analogously we can use the magnetic Mie coefficient, b_m, for TM polarization). Rearranging Eq. (5.4), we get

$$\omega_m^{Mie} = \frac{2i \cdot a_m \cdot Q_m^{Mie} \cdot \omega}{(2i \cdot Q_m^{Mie} + 1)a_m \pm 1}, \tag{5.5}$$

where $Q_m^{Mie} = \omega_m^{Mie}/2\gamma_m^{Mie}$ is the Q-factor of a Mie resonance on the order of 5-10 that can easily be estimated from numerical spectra. With ω_m^{Mie} and γ_m^{Mie} as functions of a_m, the modified TCMT can correctly produce the asymmetric line shapes of NW Mie resonances.

For a NW GSL, the full TCMT equation becomes

$$\frac{d}{dt}\begin{pmatrix} A_m^{Mie} \\ \\ A_m^{GSL} \end{pmatrix} = \left[-i \begin{pmatrix} \omega_m^{Mie} & \omega_m^{c} \\ \\ \omega_m^{c} & \omega_m^{GSL} \end{pmatrix} - \begin{pmatrix} \gamma_m^{Mie} & 0 \\ \\ 0 & \gamma_m^{GSL} \end{pmatrix} \right] \begin{pmatrix} A_m^{Mie} \\ \\ A_m^{GSL} \end{pmatrix} + \begin{pmatrix} \kappa_m^{Mie} \\ \\ \kappa_m^{GSL} \end{pmatrix} h_m^{+} \tag{5.6}$$

and $h_m^{-} = h_m^{+} + d_m^{Mie} A_m^{Mie} + d_m^{GSL} A_m^{GSL}$, where A_m^{GSL}, ω_m^{GSL} and γ_m^{GSL} are the amplitude, eigenfrequency, and radiative decay rate of an *m*th-order GSL mode, ω_m^{c} is the coupling strength between the Mie and GSL modes, and κ_m^{GSL} and d_m^{GSL} are coupling coefficients of GSL modes to the incoming and outgoing plane waves, respectively.

We only consider the coupling of modes within the same angular channel[120], and using Eq. (5.6) we can fit the numerical Q_{sca} spectra to reproduce all scattering features. As an example, Fig. 5.3(a)-(c) display Q_{sca} spectra for *p* = 220, 260, and 320 nm at a fixed *d* = 200 nm and *e* = 170 nm, where total Q_{sca} obtained from TCMT (circles) are overlaid with numerical simulations (red curves). The case of *p* = 260 nm satisfies the BIC condition, but shorter and longer *p* do not. Fano resonances appear for the shorter and longer *p* cases because the GSL modes couple with the Mie resonance ($\omega_m^{c} \neq 0$). At *p* = 260 nm, however, the *m* = 1 Fano peak almost completely vanishes at 701 nm (Fig. 5.3(b)). The analytical Q_{sca} in Fig. 5.3(b) is obtained with both ω_1^{c} and $\gamma_1^{GSL} \approx 0$, implying the emergence of a perfectly bound optical state. Because the *m* = 0 GSL mode becomes bound at a slightly different *p* than *m* = 1 (c.f. Fig. 5.1(b)), it is still observed at ∼618 nm but with a vanishing linewidth of ∼0.2 nm. Fig. 5.3(d) shows the total Q_{sca} (dashed curve) and separate Q_{sca} spectra from each angular channel calculated using Eq. (6) for the *p* = 320 nm NW GSL (circles). The two Fano resonances at ∼661 and ∼765 nm are separately observed in the *m* = 0 and 1 angular channels,

respectively, and the long tails of the asymmetric Mie resonances permit Fano resonances to appear far away from the Mie maxima of the same channel. The fitting paramters for Fig. 5.3 are summarized in Table 5.1.

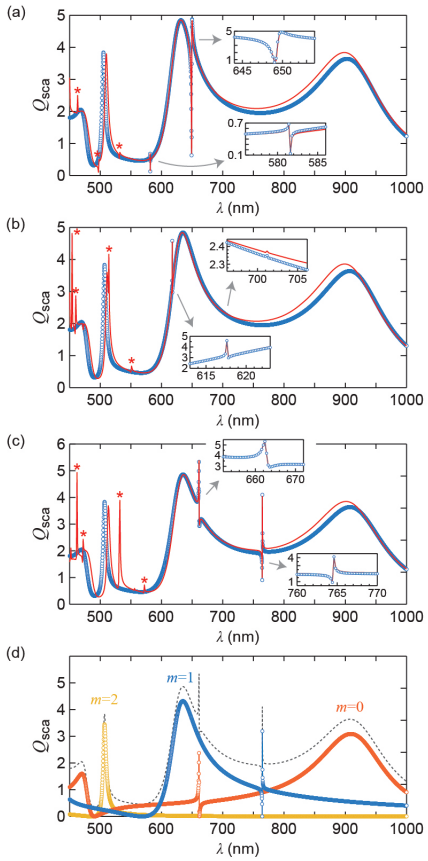

Figure 5.3: Q_{sca} spectra from TCMT and from full wave simulations. (a-c) Total Q_{sca} calculated by modified TCMT (blue circles) overlaid with numerical calculations (red curve) for a NW GSL with d = 200 nm, e = 150 nm, and p = 220 nm (a), p = 260 nm (b), or p = 320 nm (c). Insets show magnified views near Fano resonances. Peaks marked with asterisks result from higher order GSL modes not included in the TCMT. (d) Total Q_{sca} spectra (dashed curve) from panel (c) decomposed into each mth-order angular channel (circles).

p (nm)	λ_0^{GSL} (nm)	λ_1^{GSL} (nm)	ω_0^{GSL} (THz)	ω_1^{GSL} (THz)	γ_0^{GSL} (THz)	γ_1^{GSL} (THz)	ω_0^{c} (THz)	ω_1^{c} (THz)
220	581.6	649.05	3238.7	2902.2	1.6×10^{-4}	2.9×10^{-4}	9.3	16.6
260	617.6	701.2	3050.0	2686.3	2.3×10^{-2}	3.9×10^{-4}	6.1	0.5
320	661.8	764.4	2846.3	2464.2	2.8×10^{-4}	2.5×10^{-5}	24.8	10.5

Table 5.1: Parameters used in the TCMT for fitting Q_{sca} spectra in Figure 5.3.

5.2.3 Illumination and geometry dependence of BICs

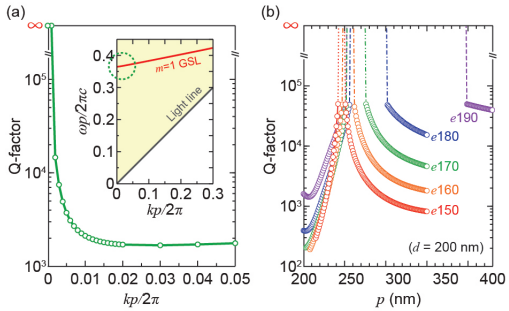

Figure 5.4: Geometric dependence of Q-factor. (a) Plot of Q-factor as a function of $kp/2\pi$. Inset: band structure of the m = 1 mode. (b) Q-factors of an m = 1 mode as a function of p with d = 200 nm and various e.

The appearance of a BIC depends sensitively on illumination and structural geometry. For instance, BICs only appear at a Γ point because the symmetry of the BIC is distorted with a nonzero axial wavevector. As an example, Fig. 5.4(a) shows the Q-factor of the m = 1 BIC mode of a NW GSL, calculated from the circled area in the inset band diagram, as a function of $kp/2\pi$ starting at Γ. The Q-factor decreases from infinity as the wavevector deviates from Γ because the loss of illumination symmetry allows the mode to couple to the Mie resonance. Moreover, even at Γ, the range of p that produces a BIC (or infinite Q-factor) changes with different values of e at a fixed d, and there is a substantial widening of the p range producing a BIC as e approaches d, as shown in the eigenmode calculations in Fig. 5.4(b). When d and e are similar, the magnitude and mode volume of dipoles within each diameter segment are similar in magnitude (Fig. 5.2), so a broad set of p can produce the total destructive interference needed to form a BIC. However, as e deviates from d, the p

range supporting a BIC narrows and eventually disappears. Frequencies of BICs formed at different p and e are summarized in Fig. 5.5.

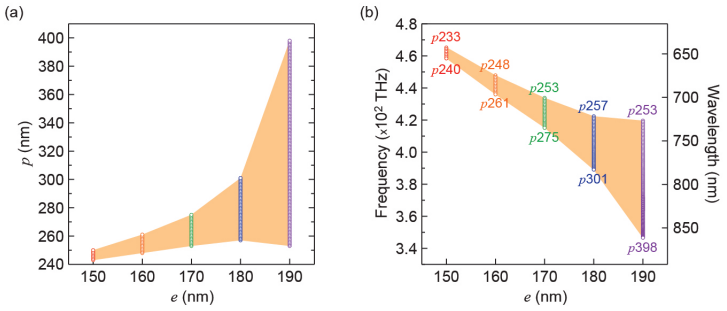

Figure 5.5: Geometric conditions, frequency and wavelengths of $m = 1$ BICs with various e at a fixed $d = 200$ nm. (a) Plots of p that forms $m = 1$ BICs as a function of e for a fixed $d = 200$m. (b) Frequency (left axis) and wavelength (right axis) of BICs from panel (a).

5.2.4 Experimental verification of BICs

We experimentally verified the scattering characteristics of NW GSLs fabricated by the ENGRAVE (Encoded Nanowire GRowth and Appearance through Vapor-liquid-solid growth and Etching) technique[22,29]. A d close to 200 nm was chosen to allow direct comparison with the scattering heatmap in Fig. 5.1(f), and p was varied from 200 nm to 400 nm with 50 nm increments to investigate the spectral shift and disappearance of the Fano resonances. To minimize variation in d and e, five 10 µm-long GSL sections with different p were encoded simultaneously in a single NW with 10 µm uniform segments separating each GSL, as shown by the scanning electron microscope (SEM) images in Fig. 5.6(a). Polarization-resolved transmissive single-NW extinction was measured in the visible range using a home-built laser microscope[157]. Simulated Q_{sca} corresponding to measured geometries and measured extinction spectra are shown in Fig. 5.6(b) and (c), respectively. Q_{sca} was simulated with a Gaussian beam (full-width-at-half-maximum of 1.5 µm) in the presence of material absorption to properly reflect the experiment.

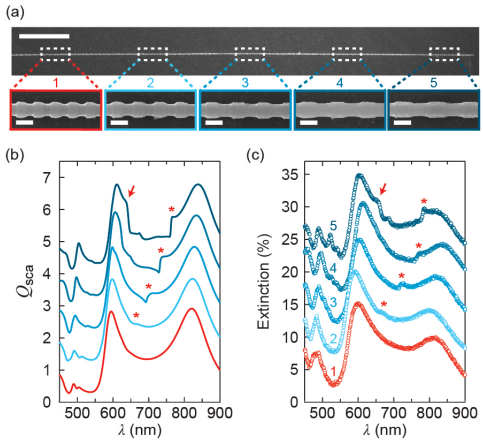

Figure 5.6: Experimental extinction measurement of NW GSLs. (a) SEM image (upper panel) of a NW containing five GSL sections; scale bar, 10 μm. Magnified views (lower panels) of each GSL segment corresponding to the boxed regions in the upper panel; scale bars, 200 nm. Geometric parameters are d = 189 ± 2 nm, e = 141 ± 2 nm, p = 201 ± 4 nm (GSL 1), d = 185 ± 1 nm, e = 135 ± 2 nm, p = 250 ± 4 nm (GSL 2), d = 186 ± 1 nm, e = 147 ± 2 nm, p = 300 ± 3 nm (GSL 3), d = 185 ± 1 nm, e = 153 ± 2 nm, p = 348 ± 4 nm (GSL 4) and d = 183 ± 1 nm, e = 148 ± 2 nm, p = 400 ± 6 nm (GSL 5). (b-c) Simulated Q_{sca} (b, spectra offset by 1) and measured extinction (c, spectra relatively offset by 5%) of GSLs. Red traces in both graphs represent spectra of a GSL at the BIC condition. Arrows and asterisks indicate the m = 0 and 1 Fano resonances, respectively.

For simulated spectra of a GSL with p = 400 nm (uppermost in Fig. 5.6(b)), two Fano resonances for m = 0 and m = 1 GSL modes are observed at ∼645 and ∼762 nm as marked by the arrow and asterisk, respectively. Compared to the sub-nm linewidth shown in Fig. 5.1(e), a substantial broadening of the Fano lineshape is observed because of absorptive loss and the finite beam [163]. An additional small peak at ∼676 nm comes from the use of a finite beam [157]. As p decreases, the m = 0 peak gradually merges into the broad Mie resonance peak centered at ∼600 nm, and the m = 1 peak (red asterisks) blueshifts and progressively decreases in magnitude. At p = 230 nm (red curve), the Fano peak vanishes because the mode becomes decoupled from the TE and TM radiation continua. The same pattern is observed in the experimentally measured extinction spectra in Fig. 5.6(c). The extinction of GSL 5 (uppermost) shows the m = 1 Fano resonance at ∼785 nm (red asterisk). The m = 1 Fano resonance blueshifts with decreasing p, and it eventually vanishes for GSL 1 (red circles), corresponding to the formation of a BIC. As a result, the extinction of GSL 1 looks identical to

the typical extinction spectrum of a uniform NW, demonstrating the inaccessibility of the trapped modes by far-field illumination. Inclusion of absorption in eigenmode calculations shows a significant reduction of the Q-factors to ∼150, and experimental Q-factors, obtained from fitting the spectra, yield values of 95-180 that qualitatively agree with calculations (see Fig. 5.7).

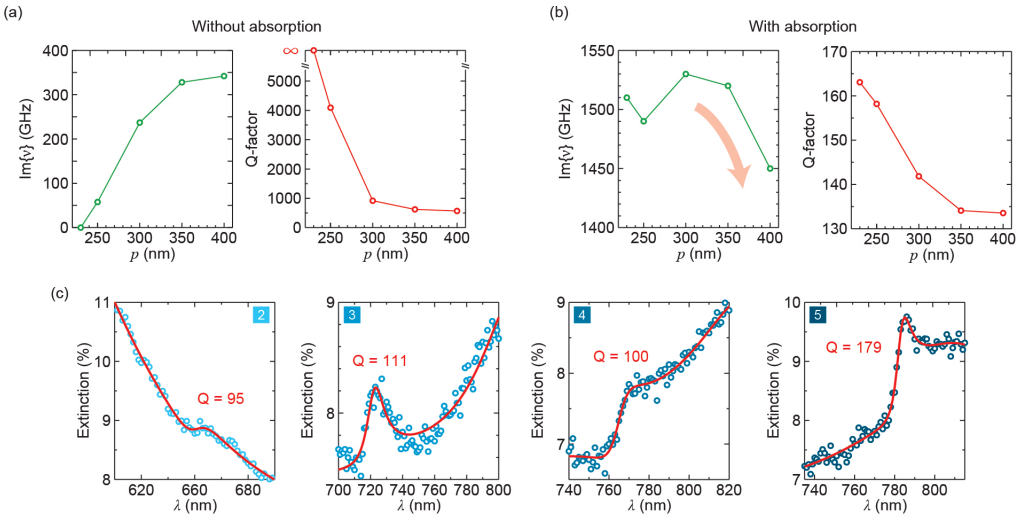

Figure 5.7: Effect of absorption on Q-factors and fits to experimental spectra. (a-b) Total loss and Q-factors calculated from eigenmode calculation in GSLs 1 (p=230 nm) through GSL 5 (p=400 nm) presented in Fig. 5.6 in the absence (a) and presence (b) of absorptive loss. In the presence of absorption, total loss decreases as p moves away from the BIC-forming condition (p=230 nm) due to decrease in absorption. (c) Fits to the experimental spectra of GSLs 2-5 from Fig. 5.6 near the Fano resonances.

5.3 Conclusion

In conclusion, we have demonstrated that NW GSLs support unique photonic modes that can be completely bound under a certain set of geometric parameters, and this report represents the first experimental demonstration of a BIC in a laterally-confined 1D geometry in the optical regime. The bottom-up growth of Si NW GSLs through the ENGRAVE process offers several technological advantages such as mechanical robustness from single-crystalline materials, ability to electro-generate photons inside the cavity through doping[23], and ease of device integration through templated growth[164]. Because the subwavelength lateral dimensions provide a true nanoscale footprint, these findings could enable the design of compact high-Q photonic devices such as single-NW photodetectors, lasers, sensors, waveguides, and photonic circuits.

CONCLUSIONS

As the physical down-sizing of microelectronic circuit elements has approached the quantum-tunneling limit, value has ever been increasing for semiconductor nanomaterials to manage photons with the same level of control as has already been done for electrons. Controlled manipulation of photons requires periodic structures with a period comparable to the wavelength of light, and semiconductor materials with high permittivities are ideal candidates for building such structures. In this work, we have investigated ways of synthesizing silicon (Si) nanowire (NW) geometric superlattices (GSLs) as well as tailoring design parameters to utilize them as nanophotonic platforms. Synthesis of arrays of vertically-standing NW GSLs using dopant-encoded vapor-liquid-solid (VLS) growth and wet-chemical etching, namely the ENGRAVE process for Encoded Nanowire GRowth and Appearance through VLS and Etching, required substantially different growth conditions than the conditions used for non-directed NW growths. The difference largely came from the tradeoff between traditionally needing to have Au decoration on NW sidewalls for stable epitaxial growth and needing to have Au-free sidewalls for conformal etching of undoped Si. The key to grow vertical epitaxial NWs that etch well was to stabilize the NW sidewalls with chlorine by flowing HCl during NW growths with SiH_4 partial pressure much higher than the conventional epitaxial growth conditions. As a result, rapid chlorination near the growth front suppresses migration of Au from the catalyst to the NW, which eventually enables the desired etching.

Despite much more colorful scattering from vertically standing NW GSLs than uniform NWs, the challenges associated with optical characterization of vertical NW GSLs necessitated a prerequisite analysis of the simplest geometry; a NW GSL horizontally oriented on a substrate under global plane wave illumination. In this geometry, a unique coupling of a bright Mie resonance with a dark, BGS was observed at a select wavelength determined by the pitch of the GSL. The selective coupling effect enabled the use of the GSL as a narrow-band light coupler to the NW waveguide (WG), and its potential for advanced optical operations such as optical switching was demonstrated based on the spectral tuning of a Mie resonance via external index control.

One might ask whether the NW GSLs should be classified as a photonic crystal (PC) or a metamaterial, but the answer is still unclear. While the Mie-BGS coupling arising from symmetry-breaking seems to share many similarities with the physics of metamaterials, a PC-like property was also observed from the same GSLs with somewhat different geometric parameters. The presence of optical bound states in the continuum (BICs), infinity-Q optical modes typically found in PCs, were observed from our Si NW GSLs theoretically and experimentally. Although this finding is still premature, it promises a bright future for applications of Si NWs for efficient light-emitting devices due to the increased lifetime of photons within the NW optical cavity. A large number of variations and hybridizations are possible including a combination of NW BIC cavities with NW photonic bandgap reflectors. Perhaps the answer to this question posed earlier is that NW GSLs are not bound to only one class but instead offer characteristics of both PCs and metamaterials.

The future research following this work should consider much broader types of geometries other than the square-wave, grating-like morphology. Indeed we have a large library of NW morphologies we can produce, and we will need to be able to leverage our synthetic skills to discover new properties. I believe that more can be found than simple alteration of diameters to exhibit exciting optical properties. Besides, because degenerately-doped Si can also support plasmons in the infrared spectrum, I would like to suggest to explore more adventurous ideas such as squeezing of infrared light using NW tapers. Lastly, I would like to close the last chapter of this work with one last statement: I look forward to seeing bright lasing out of Si NWs.

APPENDIX 1: MATLAB CODE FOR ANALYTICAL CALCULATION OF MIE SCATTERING OF A CYLINDRICAL NW

This section shows the MATLAB code for analytical calculation of Mie scattering of a cylindrical NW. Equations in this script are mostly based on Bohren.[6]

% Refractive index of silicon

The chart below contains refractive index values of silicon from 400 to 2000 nm with 1 nm step size.

5.5700	5.5367	5.5047	5.4738	5.4440	5.4153	5.3877	5.3611	5.3354	5.3106	5.2868	5.2637	5.2415	5.2200	5.1992	5.1791	5.1597	5.1408	5.1224	5.1046
5.0872	5.0703	5.0537	5.0375	5.0216	5.0059	4.9904	4.9752	4.9600	4.9449	4.9300	4.9152	4.9004	4.8859	4.8714	4.8572	4.8431	4.8291	4.8154	4.8019
4.7886	4.7755	4.7626	4.7500	4.7376	4.7256	4.7137	4.7021	4.6907	4.6796	4.6687	4.6580	4.6475	4.6373	4.6273	4.6174	4.6078	4.5983	4.5891	4.5800
4.5711	4.5624	4.5538	4.5454	4.5372	4.5290	4.5211	4.5132	4.5055	4.4978	4.4903	4.4829	4.4756	4.4683	4.4611	4.4540	4.4470	4.4400	4.4331	4.4262
4.4193	4.4125	4.4058	4.3991	4.3925	4.3860	4.3796	4.3732	4.3669	4.3607	4.3546	4.3486	4.3426	4.3368	4.3311	4.3255	4.3200	4.3146	4.3093	4.3042
4.2991	4.2941	4.2892	4.2843	4.2796	4.2748	4.2702	4.2655	4.2609	4.2564	4.2518	4.2473	4.2428	4.2383	4.2337	4.2292	4.2246	4.2200	4.2154	4.2107
4.2060	4.2013	4.1966	4.1918	4.1871	4.1823	4.1776	4.1729	4.1682	4.1636	4.1590	4.1544	4.1499	4.1454	4.1410	4.1366	4.1323	4.1281	4.1240	4.1200
4.1161	4.1122	4.1085	4.1048	4.1012	4.0977	4.0942	4.0909	4.0876	4.0843	4.0811	4.0780	4.0749	4.0718	4.0688	4.0658	4.0629	4.0600	4.0571	4.0542
4.0513	4.0485	4.0457	4.0428	4.0400	4.0372	4.0343	4.0315	4.0287	4.0258	4.0230	4.0202	4.0174	4.0146	4.0118	4.0090	4.0062	4.0035	4.0008	3.9980
3.9954	3.9927	3.9900	3.9874	3.9848	3.9823	3.9798	3.9773	3.9748	3.9724	3.9700	3.9677	3.9653	3.9631	3.9608	3.9586	3.9565	3.9543	3.9522	3.9501
3.9481	3.9460	3.9440	3.9420	3.9401	3.9381	3.9362	3.9343	3.9324	3.9305	3.9286	3.9267	3.9248	3.9230	3.9211	3.9193	3.9174	3.9156	3.9137	3.9119
3.9100	3.9081	3.9063	3.9044	3.9025	3.9006	3.8987	3.8968	3.8950	3.8931	3.8912	3.8893	3.8874	3.8855	3.8837	3.8818	3.8799	3.8781	3.8762	3.8744
3.8726	3.8707	3.8689	3.8671	3.8653	3.8636	3.8618	3.8601	3.8584	3.8566	3.8550	3.8533	3.8516	3.8500	3.8484	3.8468	3.8452	3.8437	3.8421	3.8406
3.8391	3.8376	3.8362	3.8347	3.8333	3.8319	3.8304	3.8290	3.8277	3.8263	3.8249	3.8236	3.8222	3.8209	3.8195	3.8182	3.8169	3.8156	3.8143	3.8130
3.8117	3.8104	3.8091	3.8078	3.8065	3.8052	3.8039	3.8026	3.8013	3.8000	3.7987	3.7974	3.7961	3.7948	3.7935	3.7921	3.7908	3.7895	3.7882	3.7869
3.7856	3.7843	3.7830	3.7817	3.7804	3.7791	3.7778	3.7765	3.7752	3.7739	3.7726	3.7714	3.7701	3.7688	3.7676	3.7663	3.7651	3.7639	3.7627	3.7615
3.7603	3.7591	3.7579	3.7567	3.7556	3.7544	3.7533	3.7522	3.7511	3.7500	3.7489	3.7479	3.7468	3.7458	3.7448	3.7438	3.7428	3.7418	3.7408	3.7398
3.7389	3.7379	3.7370	3.7361	3.7352	3.7343	3.7334	3.7325	3.7316	3.7308	3.7299	3.7291	3.7282	3.7274	3.7266	3.7257	3.7249	3.7241	3.7233	3.7225
3.7217	3.7209	3.7201	3.7193	3.7185	3.7177	3.7170	3.7162	3.7154	3.7146	3.7139	3.7131	3.7123	3.7115	3.7108	3.7100	3.7092	3.7085	3.7077	3.7069
3.7061	3.7054	3.7046	3.7038	3.7030	3.7022	3.7015	3.7007	3.6999	3.6991	3.6984	3.6976	3.6968	3.6960	3.6952	3.6945	3.6937	3.6929	3.6921	3.6914
3.6906	3.6898	3.6890	3.6883	3.6875	3.6867	3.6859	3.6852	3.6844	3.6836	3.6829	3.6821	3.6813	3.6806	3.6798	3.6790	3.6783	3.6775	3.6768	3.6760
3.6752	3.6745	3.6737	3.6730	3.6722	3.6715	3.6707	3.6700	3.6693	3.6685	3.6678	3.6670	3.6663	3.6656	3.6648	3.6641	3.6634	3.6627	3.6619	3.6612
3.6605	3.6598	3.6591	3.6583	3.6576	3.6569	3.6562	3.6555	3.6548	3.6541	3.6534	3.6527	3.6520	3.6513	3.6506	3.6499	3.6492	3.6485	3.6479	3.6472
3.6465	3.6458	3.6451	3.6445	3.6438	3.6431	3.6424	3.6418	3.6411	3.6404	3.6398	3.6391	3.6385	3.6378	3.6371	3.6365	3.6358	3.6352	3.6345	3.6339
3.6332	3.6326	3.6320	3.6313	3.6307	3.6300	3.6294	3.6288	3.6281	3.6275	3.6269	3.6263	3.6256	3.6250	3.6244	3.6238	3.6232	3.6226	3.6220	3.6213
3.6207	3.6201	3.6195	3.6189	3.6183	3.6177	3.6171	3.6165	3.6159	3.6154	3.6148	3.6142	3.6136	3.6130	3.6124	3.6118	3.6113	3.6107	3.6101	3.6095
3.6090	3.6084	3.6078	3.6073	3.6067	3.6062	3.6056	3.6050	3.6045	3.6039	3.6034	3.6028	3.6023	3.6017	3.6012	3.6006	3.6001	3.5996	3.5990	3.5985
3.5980	3.5974	3.5969	3.5964	3.5958	3.5953	3.5948	3.5943	3.5938	3.5932	3.5927	3.5922	3.5917	3.5912	3.5907	3.5902	3.5897	3.5892	3.5887	3.5882
3.5877	3.5872	3.5867	3.5862	3.5857	3.5852	3.5847	3.5843	3.5838	3.5833	3.5828	3.5823	3.5819	3.5814	3.5809	3.5805	3.5800	3.5795	3.5791	3.5786
3.5781	3.5777	3.5772	3.5768	3.5763	3.5759	3.5754	3.5750	3.5745	3.5741	3.5737	3.5732	3.5728	3.5723	3.5719	3.5715	3.5710	3.5706	3.5702	3.5698
3.5693	3.5689	3.5685	3.5681	3.5677	3.5673	3.5669	3.5664	3.5660	3.5656	3.5652	3.5648	3.5644	3.5640	3.5636	3.5632	3.5628	3.5624	3.5621	3.5617
3.5613	3.5609	3.5605	3.5601	3.5598	3.5594	3.5590	3.5586	3.5583	3.5579	3.5575	3.5572	3.5568	3.5564	3.5561	3.5557	3.5554	3.5550	3.5547	3.5543
3.5540	3.5536	3.5533	3.5529	3.5526	3.5522	3.5519	3.5516	3.5512	3.5509	3.5506	3.5502	3.5499	3.5496	3.5493	3.5489	3.5486	3.5483	3.5480	3.5477
3.5474	3.5470	3.5467	3.5464	3.5461	3.5458	3.5455	3.5452	3.5449	3.5446	3.5443	3.5440	3.5437	3.5435	3.5432	3.5429	3.5426	3.5423	3.5420	3.5418
3.5415	3.5412	3.5409	3.5407	3.5404	3.5401	3.5399	3.5396	3.5393	3.5391	3.5388	3.5386	3.5383	3.5381	3.5378	3.5376	3.5373	3.5371	3.5368	3.5366
3.5363	3.5361	3.5359	3.5356	3.5354	3.5352	3.5349	3.5347	3.5345	3.5343	3.5341	3.5338	3.5336	3.5334	3.5332	3.5330	3.5328	3.5326	3.5323	3.5321
3.5319	3.5317	3.5315	3.5313	3.5311	3.5309	3.5308	3.5306	3.5304	3.5302	3.5300	3.5298	3.5296	3.5295	3.5293	3.5291	3.5289	3.5288	3.5286	3.5284
3.5282	3.5281	3.5279	3.5277	3.5276	3.5274	3.5273	3.5271	3.5269	3.5268	3.5266	3.5265	3.5263	3.5262	3.5260	3.5259	3.5257	3.5256	3.5254	3.5253
3.5252	3.5250	3.5249	3.5247	3.5246	3.5245	3.5243	3.5242	3.5241	3.5239	3.5238	3.5237	3.5235	3.5234	3.5233	3.5231	3.5230	3.5229	3.5227	3.5226
3.5225	3.5224	3.5222	3.5221	3.5220	3.5219	3.5217	3.5216	3.5215	3.5214	3.5212	3.5211	3.5210	3.5209	3.5207	3.5206	3.5205	3.5204	3.5202	3.5201
3.5200	3.5199	3.5198	3.5196	3.5195	3.5194	3.5193	3.5191	3.5190	3.5189	3.5188	3.5186	3.5185	3.5184	3.5183	3.5182	3.5180	3.5179	3.5178	3.5177
3.5175	3.5174	3.5173	3.5172	3.5170	3.5169	3.5168	3.5167	3.5165	3.5164	3.5163	3.5162	3.5160	3.5159	3.5158	3.5157	3.5156	3.5154	3.5153	3.5152
3.5151	3.5149	3.5148	3.5147	3.5146	3.5144	3.5143	3.5142	3.5141	3.5139	3.5138	3.5137	3.5136	3.5134	3.5133	3.5132	3.5131	3.5129	3.5128	3.5127
3.5126	3.5124	3.5123	3.5122	3.5121	3.5119	3.5118	3.5117	3.5116	3.5114	3.5113	3.5112	3.5111	3.5109	3.5108	3.5107	3.5106	3.5104	3.5103	3.5102
3.5101	3.5099	3.5098	3.5097	3.5096	3.5094	3.5093	3.5092	3.5091	3.5089	3.5088	3.5087	3.5086	3.5084	3.5083	3.5082	3.5081	3.5079	3.5078	3.5077
3.5076	3.5074	3.5073	3.5072	3.5071	3.5069	3.5068	3.5067	3.5066	3.5065	3.5063	3.5062	3.5061	3.5060	3.5058	3.5057	3.5056	3.5055	3.5053	3.5052
3.5051	3.5050	3.5048	3.5047	3.5046	3.5045	3.5043	3.5042	3.5041	3.5040	3.5038	3.5037	3.5036	3.5035	3.5033	3.5032	3.5031	3.5030	3.5028	3.5027
3.5026	3.5025	3.5023	3.5022	3.5021	3.5020	3.5018	3.5017	3.5016	3.5015	3.5013	3.5012	3.5011	3.5010	3.5009	3.5007	3.5006	3.5005	3.5004	3.5002
3.5001	3.5000	3.4999	3.4997	3.4996	3.4995	3.4994	3.4992	3.4991	3.4990	3.4989	3.4988	3.4986	3.4985	3.4984	3.4983	3.4981	3.4980	3.4979	3.4978
3.4976	3.4975	3.4974	3.4973	3.4972	3.4970	3.4969	3.4968	3.4967	3.4965	3.4964	3.4963	3.4962	3.4961	3.4959	3.4958	3.4957	3.4956	3.4954	3.4953
3.4952	3.4951	3.4950	3.4948	3.4947	3.4946	3.4945	3.4943	3.4942	3.4941	3.4940	3.4939	3.4937	3.4936	3.4935	3.4934	3.4933	3.4931	3.4930	3.4929
3.4928	3.4926	3.4925	3.4924	3.4923	3.4922	3.4920	3.4919	3.4918	3.4917	3.4916	3.4914	3.4913	3.4912	3.4911	3.4910	3.4908	3.4907	3.4906	3.4905
3.4904	3.4903	3.4901	3.4900	3.4899	3.4898	3.4897	3.4895	3.4894	3.4893	3.4892	3.4891	3.4889	3.4888	3.4887	3.4886	3.4885	3.4884	3.4882	3.4881
3.4880	3.4879	3.4878	3.4876	3.4875	3.4874	3.4873	3.4872	3.4871	3.4869	3.4868	3.4867	3.4866	3.4865	3.4864	3.4862	3.4861	3.4860	3.4859	3.4858
3.4857	3.4855	3.4854	3.4853	3.4852	3.4851	3.4850	3.4849	3.4847	3.4846	3.4845	3.4844	3.4843	3.4842	3.4841	3.4839	3.4838	3.4837	3.4836	3.4835
3.4834	3.4833	3.4831	3.4830	3.4829	3.4828	3.4827	3.4826	3.4825	3.4823	3.4822	3.4821	3.4820	3.4819	3.4818	3.4817	3.4816	3.4814	3.4813	3.4812
3.4811	3.4810	3.4809	3.4808	3.4807	3.4806	3.4804	3.4803	3.4802	3.4801	3.4800	3.4799	3.4798	3.4797	3.4796	3.4794	3.4793	3.4792	3.4791	3.4790
3.4789	3.4788	3.4787	3.4786	3.4785	3.4784	3.4782	3.4781	3.4780	3.4779	3.4778	3.4777	3.4776	3.4775	3.4774	3.4773	3.4772	3.4771	3.4770	3.4768
3.4767	3.4766	3.4765	3.4764	3.4763	3.4762	3.4761	3.4760	3.4759	3.4758	3.4757	3.4756	3.4755	3.4754	3.4753	3.4752	3.4751	3.4749	3.4748	3.4747
3.4746	3.4745	3.4744	3.4743	3.4742	3.4741	3.4740	3.4739	3.4738	3.4737	3.4736	3.4735	3.4734	3.4733	3.4732	3.4731	3.4730	3.4729	3.4728	3.4727
3.4726	3.4725	3.4724	3.4723	3.4722	3.4721	3.4720	3.4719	3.4718	3.4717	3.4716	3.4715	3.4714	3.4713	3.4712	3.4711	3.4710	3.4709	3.4708	3.4707
3.4706	3.4705	3.4704	3.4703	3.4702	3.4701	3.4700	3.4699	3.4698	3.4697	3.4696	3.4695	3.4694	3.4693	3.4693	3.4692	3.4691	3.4690	3.4689	3.4688
3.4687	3.4686	3.4685	3.4684	3.4683	3.4682	3.4681	3.4680	3.4679	3.4678	3.4677	3.4677	3.4676	3.4675	3.4674	3.4673	3.4672	3.4671	3.4670	3.4669
3.4668	3.4667	3.4667	3.4666	3.4665	3.4664	3.4663	3.4662	3.4661	3.4660	3.4659	3.4658	3.4658	3.4657	3.4656	3.4655	3.4654	3.4653	3.4652	3.4651
3.4651	3.4650	3.4649	3.4648	3.4647	3.4646	3.4645	3.4645	3.4644	3.4643	3.4642	3.4641	3.4640	3.4639	3.4639	3.4638	3.4637	3.4636	3.4635	3.4634
3.4634	3.4633	3.4632	3.4631	3.4630	3.4629	3.4629	3.4628	3.4627	3.4626	3.4625	3.4625	3.4624	3.4623	3.4622	3.4621	3.4621	3.4620	3.4619	3.4618
3.4617	3.4617	3.4616	3.4615	3.4614	3.4614	3.4613	3.4612	3.4611	3.4610	3.4610	3.4609	3.4608	3.4607	3.4607	3.4606	3.4605	3.4604	3.4604	3.4603
3.4602	3.4601	3.4601	3.4600	3.4599	3.4598	3.4598	3.4597	3.4596	3.4596	3.4595	3.4594	3.4593	3.4593	3.4592	3.4591	3.4591	3.4590	3.4589	3.4588
3.4588	3.4587	3.4586	3.4586	3.4585	3.4584	3.4584	3.4583	3.4582	3.4582	3.4581	3.4580	3.4580	3.4579	3.4578	3.4578	3.4577	3.4576	3.4576	3.4575
3.4574	3.4574	3.4573	3.4572	3.4572	3.4571	3.4570	3.4570	3.4569	3.4569	3.4568	3.4567	3.4567	3.4566	3.4565	3.4565	3.4564	3.4564	3.4563	3.4562
3.4562	3.4561	3.4561	3.4560	3.4559	3.4559	3.4558	3.4558	3.4557	3.4557	3.4556	3.4555	3.4555	3.4554	3.4554	3.4553	3.4553	3.4552	3.4552	3.4551
3.4550	3.4550	3.4549	3.4549	3.4548	3.4548	3.4547	3.4547	3.4546	3.4546	3.4545	3.4545	3.4544	3.4544	3.4543	3.4543	3.4542	3.4542	3.4541	3.4541
3.4540	3.4540	3.4539	3.4539	3.4538	3.4538	3.4537	3.4537	3.4536	3.4536	3.4535	3.4535	3.4534	3.4534	3.4533	3.4533	3.4533	3.4532	3.4532	3.4531
3.4531	3.4530	3.4530	3.4529	3.4529	3.4529	3.4528	3.4528	3.4527	3.4527	3.4527	3.4526	3.4526	3.4525	3.4525	3.4525	3.4524	3.4524	3.4523	3.4523
3.4523	3.4522	3.4522	3.4521	3.4521	3.4521	3.4520	3.4520	3.4520	3.4519	3.4519	3.4519	3.4518	3.4518	3.4518	3.4517	3.4517	3.4517	3.4516	3.4516
3.4516	3.4515	3.4515	3.4515	3.4514	3.4514	3.4514	3.4514	3.4513	3.4513	3.4513	3.4512	3.4512	3.4512	3.4512	3.4511	3.4511	3.4511	3.4510	3.4510
3.4510	3.4510	3.4509	3.4509	3.4509	3.4509	3.4508	3.4508	3.4508	3.4508	3.4508	3.4507	3.4507	3.4507	3.4507	3.4506	3.4506	3.4506	3.4506	3.4506
3.4505	3.4505	3.4505	3.4505	3.4505	3.4505	3.4504	3.4504	3.4504	3.4504	3.4504	3.4504	3.4503	3.4503	3.4503	3.4503	3.4503	3.4503	3.4503	3.4502
3.4502	3.4502	3.4502	3.4502	3.4502	3.4502	3.4502	3.4501	3.4501	3.4501	3.4501	3.4501	3.4501	3.4501	3.4501	3.4501	3.4501	3.4501	3.4501	3.4501
3.4500	3.4500	3.4500	3.4500	3.4500	3.4500	3.4500	3.4500	3.4500	3.4500	3.4500	3.4500	3.4500	3.4500	3.4500	3.4500	3.4500	3.4500	3.4500	3.4500
3.4500																			

```
% Make a vector containing all the values from the chart and name it “si_n_1nm”. For a finer step size, run
interpolation commands:
wav=400:1:2000; % in nm; wavelength vector with 1 nm step size
stepSize=0.2;
finer_wav = 400:stepSize:2000; % in nm; wavelength vector with a finer step size
si_n_finer = interp1(wav,si_n_1nm,finer_wav,’spline’); % interpolate

% Define common constants
n0=1; % refractive index of surrounnding medium. 1 for air
n1=si_n_finer; % refractive index of dielectric
theta=degtorad(90); % incident angle; 90=normal; 0=end-on
wav=finer_wav; % wavelength in nm. Length must match with that of refractive index

% Input parameters
diameter=150; % in nm
R=diameter/2*10^-9; % radius of cylinder
nu=0:2; % angular number range; can choose a single channel

% Choose polarization
pol = questdlg(‘Polarization’, ‘Polarization’, ‘TM’,‘TE’,‘TM’); % choose polarization
    switch pol

%%%%%%%%%%%%%%%%%%%% TM %%%%%%%%%%%%%%%%%%%%
    case ‘TM’
        % Calculate aI_n, bI_n & Qsca
        for l=1:length(nu)
            for k=1:length(wav)
                beta0(k)=2*pi*n0/(wav(k)*10^-9);
                x0(k)=beta0(k)*R;
                xi(k)=x0(k)*sin(theta);
                eta(k)=x0(k)*sqrt(n1(k)^2-(cos(theta))^2);
```

```
            Dn(k)=nu(l)*cos(theta)*eta(k)*besselj(nu(l),eta(k))*besselh(nu(l),1,xi(k))*
                (xi(k)^2/eta(k)^2-1);
            Bn(k)=xi(k)*(n1(k)^2*xi(k)*besselj_derivative(nu(l),eta(k))*
                besselj(nu(l),xi(k))-eta(k)*besselj(nu(l),eta(k))*
                besselj_derivative(nu(l),xi(k)));
            Cn(k)=nu(l)*cos(theta)*eta(k)*besselj(nu(l),eta(k))*besselj(nu(l),xi(k))*
                (xi(k)^2/eta(k)^2-1);
            Vn(k)=xi(k)*(n1(k)^2*xi(k)*besselj_derivative(nu(l),eta(k))*
                besselh(nu(l),1,xi(k))-eta(k)*besselj(nu(l),eta(k))*
                besselh_derivative(nu(l),1,xi(k)));
            Wn(k)=i*xi(k)*(eta(k)*besselj(nu(l),eta(k))*besselh_derivative(nu(l),1,xi(k))
                -xi(k)*besselj_derivative(nu(l),eta(k))*besselh(nu(l),1,xi(k)));

            aI_NUMERATOR(k) = Cn(k)*Vn(k)-Bn(k)*Dn(k);
            aI_DENOMINATOR(k) = Wn(k)*Vn(k)+i*Dn(k)^2;
            aI_n(l,k) = aI_NUMERATOR(k)/aI_DENOMINATOR(k);

            bI_NUMERATOR(k) = Wn(k)*Bn(k)+i*Dn(k)*Cn(k);
            bI_DENOMINATOR(k) = Wn(k)*Vn(k)+i*Dn(k)^2;
            bI_n(l,k) = bI_NUMERATOR(k)/bI_DENOMINATOR(k);

            if nu(l)==0
                Mie_TM_Qsca(l,k)=2/x0(k)*abs(bI_n(l,k))^2;
            else
                Mie_TM_Qsca(l,k)=4/x0(k)*(abs(aI_n(l,k))^2+abs(bI_n(l,k))^2);
            end
        end
    end

    % Calculate QscaTot
    for k=1:length(wav)
        Mie_TM_QscaTot(k)=0;
```

```
        end
        for l=1:length(nu)
            for k=1:length(wav)
                Mie_TM_QscaTot(k)=Mie_TM_QscaTot(k)+Mie_TM_Qsca(l,k);
            end
        end
        % Plot
        figure
        hold on
        plot(wav,Mie_TM_Qsca)
        plot(wav,Mie_TM_QscaTot)

%%%%%%%%%%%%%%%%%%%%%%% TE %%%%%%%%%%%%%%%%%%%%%%%
    case 'TE'
        % Calculate aII_n, bII_n & Qsca
        for l=1:length(nu)
            for k=1:length(wav)
                beta0(k)=2*pi*n0/(wav(k)*10^-9);
                x0(k)=beta0(k)*R;
                xi(k)=x0(k)*sin(theta);
                eta(k)=x0(k)*sqrt(n1(k)^2-(cos(theta))^2);

                Dn(k)=nu(l)*cos(theta)*eta(k)*besselj(nu(l),eta(k))*
                    besselh(nu(l),1,xi(k))*(xi(k)^2/eta(k)^2-1);
                Bn(k)=xi(k)*(n1(k)^2*xi(k)*besselj_derivative(nu(l),eta(k))*
                    besselj(nu(l),xi(k))-eta(k)*besselj(nu(l),eta(k))*
                    besselj_derivative(nu(l),xi(k)));
                Cn(k)=nu(l)*cos(theta)*eta(k)*besselj(nu(l),eta(k))*
                    besselj(nu(l),xi(k))*(xi(k)^2/eta(k)^2-1);
                Vn(k)=xi(k)*(n1(k)^2*xi(k)*besselj_derivative(nu(l),eta(k))*
                    besselh(nu(l),1,xi(k))-eta(k)*besselj(nu(l),eta(k))*
```

```
            besselh_derivative(nu(l),1,xi(k)));
        Wn(k)=i*xi(k)*(eta(k)*besselj(nu(l),eta(k))*besselh_derivative(nu(l),1,xi(k))-
            xi(k)*besselj_derivative(nu(l),eta(k))*besselh(nu(l),1,xi(k)));
        An(k)=i*xi(k)*(xi(k)*besselj_derivative(nu(l),eta(k))*besselj(nu(l),xi(k))-
            eta(k)*besselj(nu(l),eta(k))*besselj_derivative(nu(l),xi(k)));

        aII_NUMERATOR(k) = -(An(k)*Vn(k)-i*Cn(k)*Dn(k));
        aII_DENOMINATOR(k) = Wn(k)*Vn(k)+i*Dn(k)^2;
        aII_n(l,k) = aII_NUMERATOR(k)/aII_DENOMINATOR(k);

        bII_NUMERATOR(k) = -i*(Cn(k)*Wn(k)+An(k)*Dn(k));
        bII_DENOMINATOR(k) = Wn(k)*Vn(k)+i*Dn(k)^2;
        bII_n(l,k) = bII_NUMERATOR(k)/bII_DENOMINATOR(k);

        if nu(l)==0
            Mie_TE_Qsca(l,k)=2/x0(k)*abs(aII_n(l,k))^2;
        else
            Mie_TE_Qsca(l,k)=4/x0(k)*(abs(aII_n(l,k))^2+abs(bII_n(l,k))^2);
        end
    end
end

% Calculate QscaTot
for k=1:length(wav)
    Mie_TE_QscaTot(k)=0;
end
for l=1:length(nu)
    for k=1:length(wav)
        Mie_TE_QscaTot(k)=Mie_TE_QscaTot(k)+Mie_TE_Qsca(l,k);
    end
end
% Plot
```

```
            figure
            hold on
            plot(wav,Mie_TE_Qsca)
            plot(wav,Mie_TE_QscaTot)
        end
% Define additional functions
function J = besselj_derivative(nu,x)
        J = 0.5*(besselj(nu-1,x)-besselj(nu+1,x));
end

function H = besselh_derivative(nu,K,x)
        if (K ~= 1&&K ~= 2)
            error('Improper kind of Hankel function');
        end
        H = 0.5*(besselh(nu-1,K,x)-besselh(nu+1,K,x));
end
```

APPENDIX 2: MATLAB CODE FOR TEMPORAL COUPLED MODE THEORY

This section shows the MATLAB code for temporal coupled-mode theory. In order to run this code, proper aI_n and bI_n (for TM) or aII_n and bII_n (for TE) must be obtained from Appendix 1 prior to this calculation. Fit parameters used in this example are for p = 260 nm of Fig. 5.3(b).

```
% Input variables
lam_0=617.6; % in nm. Position of 0th order Fano peak
lam_1=701.2; % in nm. Position of 1st order Fano peak

% Control parameters
% Here, division factors are taken as input parameters that will determine ω_m^c's (coupling strengths) and γ_m
's (decay rates of Fano peaks) for each m-th order channel in TCMT.
fw0c = 500; will determine w0c below: coupling strength of 0th mode
fw1c = 5000; will determine w0c below: coupling strength of 1st mode
fg0 = 130000; will determine g0 below: decay rate of 0th mode
fg1 = 6950000; will determine g1 below: decay rate of 1st mode

% Common variables
Q0=5; % Q-factor of 0-th order Mie resonance
Q1=10; % Q-factor of 1-th order Mie resonance
Q2=10; % Q-factor of 2-th order Mie resonance

% Convert Parameters
c = 299792458;
w0 = 2*pi*c/(lam_0*10^-9); frequency of 0th Fano peak
w1 = 2*pi*c/(lam_1*10^-9); frequency of 1st Fano peak
w0c = w0/fw0c; coupling strength of 0th Fano peak
w1c = w1/fw1c; coupling strength of 1st Fano peak
g0 = w0/fg0; decay rate of 0th Fano peak
g1 = w1/fg1 decay rate of 1st Fano peak;
k0 = sqrt(2*g0);
```

```
k1 = sqrt(2*g1);

% Calculate
wav = 400:0.2:2000; % length of wavelength must match that of a_n and b_n

clear i
for j=1:length(wav)
        w(j)=2*pi*c/(wav(j)*10^-9);
        x(j)=2*pi/(wav(j)*10^-9)*(diameter*10^-9)/2;

        a_n0(j)=aII_n(1,j);
        a_n1(j)=aII_n(2,j);
        a_n2(j)=aII_n(3,j);

        w_m0(j)=i*a_n0(j)*w(j)/(i*a_n0(j)+(a_n0(j)-1)/(2*Q0));
        w_m1(j)=i*a_n1(j)*w(j)/(i*a_n1(j)+(a_n1(j)-1)/(2*Q1));
        w_m2(j)=i*a_n2(j)*w(j)/(i*a_n2(j)+(a_n2(j)-1)/(2*Q2));

        gm0(j)=w_m0(j)/(2*Q0);
        gm1(j)=w_m1(j)/(2*Q1);
        gm2(j)=w_m2(j)/(2*Q2);

        km0=sqrt(2*gm0(j));
        km1=sqrt(2*gm1(j));
        km2=sqrt(2*gm2(j));

        M0=[i*(w_m0(j)-w(j))+gm0(j) i*w0c; i*w0c i*(w0-w(j))+g0];
        M1=[i*(w_m1(j)-w(j))+gm1(j) i*w1c; i*w1c i*(w1-w(j))+g1];
        M2= i*(w_m2(j)-w(j))+gm2(j);

        A0_S=M0\[km0;k0];
        A1_S=M1\[km1;k1];
        A2_S=M2\km2;
```

```
        R0(j)=1+conj(km0)*A0_S(1,1)+k0*A0_S(2,1);
        R1(j)=1+conj(km1)*A1_S(1,1)+k1*A1_S(2,1);
        R2(j)=1+conj(km2)*A2_S(1,1);

        S0(j)=(1-R0(j))/2;
        S1(j)=(1-R1(j))/2;
        S2(j)=(1-R2(j))/2;

        TCMT_Qsca(1,j)=2/x(j)*(abs(S0(j)).^2);
        TCMT_Qsca(2,j)=4/x(j)*(abs(S1(j)).^2);
        TCMT_Qsca(3,j)=4/x(j)*(abs(S2(j)).^2);
        TCMT_QscaTot(1,j)=TCMT_Qsca(1,j)+TCMT_Qsca(2,j)+TCMT_Qsca(3,j);
end

figure
hold on
plot(wav,TCMT_Qsca,'.-')
plot(wav,TCMT_QscaTot,'.-')
```

REFERENCES

[1] Adachi, S. *Properties of Group-IV, III-V and II-VI Semiconductors*; John Wiley & Sons, Ltd: Hoboken, 2005.

[2] Shirasaki, Y.; Supran, G. J.; Bawendi, M. G.; Bulović, V. *Nature Photonics* **2012**, *7*, 13.

[3] Steckel, J. S.; Coe-Sullivan, S.; Bulović, V.; Bawendi, M. G. *Advanced Materials* **2003**, *15*, 1862–1866.

[4] H. Sargent, E. *Advanced Materials* **2005**, *17*, 515–522.

[5] Dohnalova, K.; Poddubny, A. N.; Prokofiev, A. A.; de Boer, W. D. A. M.; Umesh, C. P.; Paulusse, J. M. J.; Zuilhof, H.; Gregorkiewicz, T. *Light-Science & Applications* **2013**, *2*, e47.

[6] Bohren, C. F.; Huffman, D. R. *Absorption and Scattering of Light by Small Particles*; 1998.

[7] Wagner, R. S.; Ellis, W. C. *Applied Physics Letters* **1964**, *4*, 89–90.

[8] Schmidt, V.; Wittemann, J. V.; Gösele, U. *Chemical Reviews* **2010**, *110*, 361–388.

[9] Jafari Jam, R.; Heurlin, M.; Jain, V.; Kvennefors, A.; Graczyk, M.; Maximov, I.; Borgstrom, M. T.; Pettersson, H.; Samuelson, L. *Nano Letters* **2015**, *15*, 134–138.

[10] Mårtensson, T.; Carlberg, P.; Borgström, M.; Montelius, L.; Seifert, W.; Samuelson, L. *Nano Letters* **2004**, *4*, 699–702.

[11] Meyers, J. K.; Kim, S.; Hill, D. J.; Cating, E. E. M.; Williams, L. J.; Kumbhar, A. S.; McBride, J. R.; Papanikolas, J. M.; Cahoon, J. F. *Nano Letters* **2017**, *17*, 7561–7568.

[12] Gudiksen, M. S.; Lauhon, L. J.; Wang, J.; Smith, D. C.; Lieber, C. M. *Nature* **2002**, *415*, 617–620.

[13] Lauhon, L. J.; Gudiksen, M. S.; Lieber, C. M. *Philosophical Transactions. Series A, Mathematical, Physical, and Engineering Sciences* **2004**, *362*, 1247–1260.

[14] Kempa, T. J.; Cahoon, J. F.; Kim, S.-K.; Day, R. W.; Bell, D. C.; Park, H.-G.; Lieber, C. M. *Proceedings of the National Academy of Sciences of the United States of America* **2012**, *109*, 1407–1412.

[15] Tian, B.; Zheng, X.; Kempa, T. J.; Fang, Y.; Yu, N.; Yu, G.; Huang, J.; Lieber, C. M. *Nature* **2007**, *449*, 885–889.

[16] Qian, F.; Li, Y.; Gradecak, S.; Park, H.-G.; Dong, Y.; Ding, Y.; Wang, Z. L.; Lieber, C. M. *Nat Mater* **2008**, *7*, 701–706.

[17] Stettner, T.; Thurn, A.; Döblinger, M.; Hill, M. O.; Bissinger, J.; Schmiedeke, P.; Matich, S.; Kostenbader, T.; Ruhstorfer, D.; Riedl, H.; Kaniber, M.; Lauhon, L. J.; Finley, J. J.; Koblmüller, G. *Nano Letters* **2018**, *18*, 6292–6300.

[18] Ben-Ishai, M.; Patolsky, F. *Nano Letters* **2012**, *12*, 1121–1128.

[19] Wen, C.-Y.; Reuter, M. C.; Bruley, J.; Tersoff, J.; Kodambaka, S.; Stach, E. A.; Ross, F. M. *Science* **2009**, *326*, 1247–1250.

[20] Scarpellini, D.; Somaschini, C.; Fedorov, A.; Bietti, S.; Frigeri, C.; Grillo, V.; Esposito, L.; Salvalaglio, M.; Marzegalli, A.; Montalenti, F.; Bonera, E.; Medaglia, P. G.; Sanguinetti, S. *Nano Letters* **2015**, *15*, 3677–3683.

[21] Ren, D.; Ahtapodov, L.; Nilsen, J. S.; Yang, J.; Gustafsson, A.; Huh, J.; Conibeer, G. J.; van Helvoort, A. T. J.; Fimland, B.-O.; Weman, H. *Nano Letters* **2018**, *18*, 2304–2310.

[22] Christesen, J. D.; Pinion, C. W.; Grumstrup, E. M.; Papanikolas, J. M.; Cahoon, J. F. *Nano Letters* **2013**, *13*, 6281–6286.

[23] Hill, D. J.; Teitsworth, T. S.; Kim, S.; Christesen, J. D.; Cahoon, J. F. *ACS Applied Materials & Interfaces* **2017**, *9*, 37105–37111.

[24] Algra, R. E.; Verheijen, M. A.; Borgstrom, M. T.; Feiner, L. F.; Immink, G.; van Enckevort, W. J.; Vlieg, E.; Bakkers, E. P. *Nature* **2008**, *456*, 369–372.

[25] Assali, S.; Gagliano, L.; Oliveira, D. S.; Verheijen, M. A.; Plissard, S. R.; Feiner, L. F.; Bakkers, E. P. *Nano Letters* **2015**, *15*, 8062–8069.

[26] Burgess, T.; Breuer, S.; Caroff, P.; Wong-Leung, J.; Gao, Q.; Hoe Tan, H.; Jagadish, C. *ACS Nano* **2013**, *7*, 8105–8114.

[27] Musin, I. R.; Boyuk, D. S.; Filler, M. A. *Journal of Vacuum Science & Technology B: Microelectronics and Nanometer Structures* **2013**, *31*, 20603–20605.

[28] Musin, I. R.; Shin, N.; Filler, M. A. *Journal of Materials Chemistry C* **2014**, *2*, 3285–3291.

[29] Christesen, J. D.; Pinion, C. W.; Hill, D. J.; Kim, S.; Cahoon, J. F. *The Journal of Physical Chemistry Letters* **2016**, 685–692.

[30] Day, R. W.; Mankin, M. N.; Gao, R.; No, Y.-S.; Kim, S.-K.; Bell, D. C.; Park, H.-G.; Lieber, C. M. *Nature Nanotechnology* **2015**, *10*, 345–352.

[31] Kuznetsov, A. I.; Miroshnichenko, A. E.; Brongersma, M. L.; Kivshar, Y. S.; Luk'yanchuk, B. *Science* **2016**, *354*.

[32] Kim, S.-K.; Zhang, X.; Hill, D. J.; Song, K.-D.; Park, J.-S.; Park, H.-G.; Cahoon, J. F. *Nano Letters* **2015**, *15*, 753–758.

[33] Cao, L.; Fan, P.; Barnard, E. S.; Brown, A. M.; Brongersma, M. L. *Nano Letters* **2010**, *10*, 2649–2654.

[34] Brönstrup, G.; Jahr, N.; Leiterer, C.; Csáki, A.; Fritzsche, W.; Christiansen, S. *ACS Nano* **2010**, *4*, 7113–7122.

[35] Hill, D. J.; Pinion, C. W.; Christesen, J. D.; Cahoon, J. F. *ACS Photonics* **2014**, *1*, 725–731.

[36] Seo, K.; Wober, M.; Steinvurzel, P.; Schonbrun, E.; Dan, Y.; Ellenbogen, T.; Crozier, K. B. *Nano Letters* **2011**, *11*, 1851–1856.

[37] Ee, H.-S.; Kang, J.-H.; Brongersma, M. L.; Seo, M.-K. *Nano Letters* **2015**, *15*, 1759–1765.

[38] Holsteen, A. L.; Raza, S.; Fan, P.; Kik, P. G.; Brongersma, M. L. *Science* **2017**, *358*, 1407–1410.

[39] van de Groep, J.; Brongersma, M. L. *Nano Letters* **2018**, *18*, 3857–3864.

[40] Cao, L.; Fan, P.; Brongersma, M. L. *Nano Letters* **2011**, *11*, 1463–1468.

[41] Fan, P.; Chettiar, U. K.; Cao, L.; Afshinmanesh, F.; Engheta, N.; Brongersma, M. L. *Nature Photonics* **2012**, *6*, 380–385.

[42] Hyun, J. K.; Kang, T.; Baek, H.; Kim, D.-s.; Yi, G.-c. *Nano Letters* **2015**, *15*, 5938–5943.

[43] Kim, K.-H.; No, Y.-S.; Chang, S.; Choi, J.-H.; Park, H.-G. *Scientific Reports* **2015**, *5*, 16027.

[44] Cho, C.-H.; Aspetti, C. O.; Turk, M. E.; Kikkawa, J. M.; Nam, S.-W.; Agarwal, R. *Nature Materials* **2011**, *10*, 669–675.

[45] Cho, C. H.; Aspetti, C. O.; Park, J.; Agarwal, R. *Nature Photonics* **2013**, *7*, 285–289.

[46] Glassner, S.; Keshmiri, H.; Hill, D. J.; Cahoon, J. F.; Fernandez, B.; den Hertog, M. I.; Lugstein, A. *Nano Letters* **2018**, *18*, 7230–7237.

[47] Cao, L.; White, J. S.; Park, J.-S.; Schuller, J. A.; Clemens, B. M.; Brongersma, M. L. *Nature Materials* **2009**, *8*, 643–647.

[48] Abujetas, D. R.; Paniagua-Dominguez, R.; Sanchez-Gil, J. A. *ACS Photonics* **2015**, *2*, 921–929.

[49] Fountaine, K. T.; Whitney, W. S.; Atwater, H. A. *Journal of Applied Physics* **2014**, *116*, 153106.

[50] Law, M.; Sirbuly, D. J.; Johnson, J. C.; Goldberger, J.; Saykally, R. J.; Yang, P. *Science* **2004**, *305*, 1269–1273.

[51] No, Y.-S.; Xu, L.; Mankin, M. N.; Park, H.-G. *ACS Photonics* **2016**,

[52] Dobrovolsky, A.; Stehr, J. E.; Sukrittanon, S.; Kuang, Y.; Tu, C. W.; Chen, W. M.; Buyanova, I. A. *Small* **2015**, n/a–n/a.

[53] Zhang, D.; Eaton, S. W.; Yu, Y.; Dou, L.; Yang, P. *Journal of the American Chemical Society* **2015**, *137*, 9230–9233.

[54] Fu, Y.; Zhu, H.; Schrader, A. W.; Liang, D.; Ding, Q.; Joshi, P.; Hwang, L.; Zhu, X. Y.; Jin, S. *Nano Letters* **2016**, *16*, 1000–1008.

[55] Zhu, H.; Fu, Y.; Meng, F.; Wu, X.; Gong, Z.; Ding, Q.; Gustafsson, M. V.; Trinh, M. T.; Jin, S.; Zhu, X. Y. *Nature Materials* **2015**, *14*, 636–642.

[56] Xing, J.; Liu, X. F.; Zhang, Q.; Ha, S. T.; Yuan, Y. W.; Shen, C.; Sum, T. C.; Xiong, Q. *Nano Letters* **2015**, *15*, 4571–4577.

[57] Chen, J.; Fu, Y.; Samad, L.; Dang, L.; Zhao, Y.; Shen, S.; Guo, L.; Jin, S. *Nano Letters* **2017**, *17*, 460–466.

[58] Wei, H.; Li, Z.; Tian, X.; Wang, Z.; Cong, F.; Liu, N.; Zhang, S.; Nordlander, P.; Halas, N. J.; Xu, H. *Nano Letters* **2011**, *11*, 471–475.

[59] Wei, H.; Wang, Z.; Tian, X.; Käll, M.; Xu, H. *Nature Communications* **2011**, *2*, 387.

[60] Piccione, B.; Cho, C. H.; van Vugt, L. K.; Agarwal, R. *Nature Nanotechnology* **2012**, *7*, 640–645.

[61] Fu, A.; Gao, H.; Petrov, P.; Yang, P. *Nano Letters* **2015**,

[62] Rybin, M. V.; Filonov, D. S.; Samusev, K. B.; Belov, P. A.; Kivshar, Y. S.; Limonov, M. F. *Nature Communications* **2015**, *6*, 10102.

[63] Chiang, C.-K.; Chung, Y.-C.; Cheng, P.-J.; Wu, C.-W.; Chang, S.-W.; Lin, T.-R. High Q/Vm hybrid photonic-plasmonic crystal nanowire cavity at telecommunication wavelengths. 2015; pp 93571J–93571J–6.

[64] Bulgakov, E. N.; Sadreev, A. F. *Physical Review A* **2017**, *96*, 13841.

[65] Deotare, P. B.; McCutcheon, M. W.; Frank, I. W.; Khan, M.; Lončar, M. *Applied Physics Letters* **2009**, *94*, 121106.

[66] Foresi, J. S.; Villeneuve, P. R.; Ferrera, J.; Thoen, E. R.; Steinmeyer, G.; Fan, S.; Joannopoulos, J. D.; Kimerling, L. C.; Smith, H. I.; Ippen, E. P. *Nature* **1997**, *390*, 143–145.

[67] Christesen, J. D.; Pinion, C. W.; Zhang, X.; McBride, J. R.; Cahoon, J. F. *ACS Nano* **2014**, *8*, 11790–11798.

[68] Pinion, C. W.; Nenon, D. P.; Christesen, J. D.; Cahoon, J. F. *ACS Nano* **2014**, *8*, 6081–6088.

[69] Zhang, A.; Zheng, G.; Lieber, C. *Nanowires: Building Blocks for Nanoscience and Nanotechnology*; Springer International Publishing, 2016.

[70] Lu, W.; Xiang, J. In *Semiconductor Nanowires: From Next-Generation Electronics to Sustainable Energy*; Lu, W., Xiang, J., Eds.; The Royal Society of Chemistry, 2015.

[71] Luo, Z.; Jiang, Y.; Myers, B. D.; Isheim, D.; Wu, J.; Zimmerman, J. F.; Wang, Z.; Li, Q.; Wang, Y.; Chen, X.; Dravid, V. P.; Seidman, D. N.; Tian, B. *Science* **2015**, *348*, 1451–1455.

[72] Zhang, X.; Ma, Z.; Luo, R.; Gu, Y.; Meng, C.; Wu, X.; Gong, Q.; Tong, L. *Nanotechnology* **2012**, *23*, 225202.

[73] Yalamanchili, S.; Emmer, H. S.; Fountaine, K. T.; Chen, C. T.; Lewis, N. S.; Atwater, H. A. *ACS Photonics* **2016**,

[74] Kelzenberg, M. D.; Boettcher, S. W.; Petykiewicz, J. A.; Turner-Evans, D. B.; Putnam, M. C.; Warren, E. L.; Spurgeon, J. M.; Briggs, R. M.; Lewis, N. S.; Atwater, H. A. *Nature Materials* **2010**, *9*, 239–244.

[75] Garnett, E.; Yang, P. D. *Nano Letters* **2010**, *10*, 1082–1087.

[76] Garnett, E. C.; Brongersma, M. L.; Cui, Y.; McGehee, M. D. In *Annual Review of Materials Research, Vol 41*; Clarke, D. R., Fratzl, P., Eds.; Annual Reviews: Palo Alto, 2011; Vol. 41; pp 269–295.

[77] Wallentin, J.; Anttu, N.; Asoli, D.; Huffman, M.; Åberg, I.; Magnusson, M. H.; Siefer, G.; Fuss-Kailuweit, P.; Dimroth, F.; Witzigmann, B.; Xu, H. Q.; Samuelson, L.; Deppert, K.; Borgström, M. T. *Science* **2013**, *339*, 1057–1060.

[78] Hochbaum, A. I.; Yang, P. D. *Chemical Reviews* **2010**, *110*, 527–546.

[79] Boettcher, S. W.; Spurgeon, J. M.; Putnam, M. C.; Warren, E. L.; Turner-Evans, D. B.; Kelzenberg, M. D.; Maiolo, J. R.; Atwater, H. A.; Lewis, N. S. *Science* **2010**, *327*, 185–187.

[80] Christesen, J. D.; Zhang, X.; Pinion, C. W.; Celano, T. A.; Flynn, C. J.; Cahoon, J. F. *Nano Letters* **2012**, *12*, 6024–6029.

[81] Shalek, A. K.; Robinson, J. T.; Karp, E. S.; Lee, J. S.; Ahn, D. R.; Yoon, M. H.; Sutton, A.; Jorgolli, M.; Gertner, R. S.; Gujral, T. S.; MacBeath, G.; Yang, E. G.; Park, H. *Proceedings of the National Academy of Sciences of the United States of America* **2010**, *107*, 1870–1875.

[82] Chiappini, C.; De Rosa, E.; Martinez, J. O.; Liu, X.; Steele, J.; Stevens, M. M.; Tasciotti, E. *Nature Materials* **2015**, *14*, 532–539.

[83] Hanson, L.; Zhao, W.; Lou, H.-Y.; Lin, Z. C.; Lee, S. W.; Chowdary, P.; Cui, Y.; Cui, B. *Nature Nanotechnology* **2015**, *10*, 554–562.

[84] Claudon, J.; Bleuse, J.; Malik, N. S.; Bazin, M.; Jaffrennou, P.; Gregersen, N.; Sauvan, C.; Lalanne, P.; Gerard, J.-M. *Nature Photonics* **2010**, *4*, 174–177.

[85] Kim, H.; Farrell, A. C.; Senanayake, P.; Lee, W.-J.; Huffaker, D. L. *Nano Letters* **2016**,

[86] Madras, P.; Dailey, E.; Drucker, J. *Nano Letters* **2009**, *9*, 3826–3830.

[87] Dailey, E.; Madras, P.; Drucker, J. *Journal of Applied Physics* **2010**, *108*, 64320.

[88] Madras, P.; Dailey, E.; Drucker, J. *Nano Letters* **2010**, *10*, 1759–1763.

[89] Lugstein, A.; Steinmair, M.; Hyun, Y. J.; Hauer, G.; Pongratz, P.; Bertagnolli, E. *Nano Letters* **2008**, *8*, 2310–2314.

[90] Kawashima, T.; Mizutani, T.; Nakagawa, T.; Torii, H.; Saitoh, T.; Komori, K.; Fujii, M. *Nano Letters* **2008**, *8*, 362–368.

[91] Shin, N.; Filler, M. A. *Nano Letters* **2012**, *12*, 2865–2870.

[92] den Hertog, M. I.; Rouviere, J.-L.; Dhalluin, F.; Desré, P. J.; Gentile, P.; Ferret, P.; Oehler, F.; Baron, T. *Nano Letters* **2008**, *8*, 1544–1550.

[93] Hochbaum, A. I.; Fan, R.; He, R.; Yang, P. *Nano Letters* **2005**, *5*, 457–460.

[94] Kayes, B. M.; Filler, M. A.; Putnam, M. C.; Kelzenberg, M. D.; Lewis, N. S.; Atwater, H. A. *Applied Physics Letters* **2007**, *91*, 103110.

[95] Oehler, F.; Gentile, P.; Baron, T.; Ferret, P.; Hertog, M. D.; Rouviere, J. *Nano Letters* **2010**, *10*, 2335–2341.

[96] Gao, Q.; Cheng, C. C.; Chen, P. J.; Choyke, W. J.; Yates, J. T. *Thin Solid Films* **1993**, *225*, 140–144.

[97] Li, Z.; Kamins, T. I.; Li, X.; Williams, R. S. *Surface Science* **2004**, *554*, L81–L86.

[98] Oehler, F.; Gentile, P.; Baron, T.; Ferret, P. *Nanotechnology* **2009**, *20*, 475307.

[99] Gentile, P.; Solanki, A.; Pauc, N.; Oehler, F.; Salem, B.; Rosaz, G.; Baron, T.; Den Hertog, M.; Calvo, V. *Nanotechnology* **2012**, *23*, 215702.

[100] Pinion, C. W.; Hill, D. J.; Christesen, J. D.; McBride, J. R.; Cahoon, J. F. *The Journal of Physical Chemistry Letters* **2016**, 4236–4242.

[101] Huang, Z.; Geyer, N.; Werner, P.; de Boor, J.; Gosele, U. *Advanced Materials* **2011**, *23*, 285–308.

[102] Kolasinski, K. W. *Nanoscale Research Letters* **2014**, *9*, 1–8.

[103] Liu, L.; Lin, F.; Heinrich, M.; Aberle, A. G.; Hoex, B. *ECS Journal of Solid State Science and Technology* **2013**, *2*, P380–P383.

[104] Jehng, W.-D.; Lin, J.-C.; Lee, S.-L. *Journal of The Electrochemical Society* **2005**, *152*, C124.

[105] Newman, C. G.; O'Neal, H. E.; Ring, M. A.; Leska, F.; Shipley, N. *International Journal of Chemical Kinetics* **1979**, *11*, 1167–1182.

[106] Lee, H. H. *Journal of Crystal Growth* **1984**, *69*, 82–90.

[107] Pauling, L. *The Nature of the Chemical Bond*, 3rd ed.; Cornell University Press: Ithaca, United States, 1960.

[108] Sivaram, S. V.; Hui, H. Y.; de la Mata, M.; Arbiol, J.; Filler, M. A. *Nano Letters* **2016**, *16*, 6717–6723.

[109] Amit, I.; Jeon, N.; Lauhon, L. J.; Rosenwaks, Y. *ACS Applied Materials & Interfaces* **2016**, *8*, 128–134.

[110] Sysoev, S. E.; Potapenko, D. V.; Ermakov, A. V.; Hinch, B. J.; Strongin, D. R.; Wright, A. P.; Kuivila, C. *The Journal of Physical Chemistry B* **2002**, *106*, 2018–2025.

[111] Gupta, P.; Coon, P. A.; Koehler, B. G.; George, S. M. *Surface Science* **1991**, *249*, 92–104.

[112] Atwater, H. A. *ACS Photonics* **2016**, *3*, 155–157.

[113] Vlasov, Y.; Green, W. M. J.; Xia, F. *Nature Photonics* **2008**, *2*, 242–246.

[114] Sun, C. et al. *Nature* **2015**, *528*, 534–538.

[115] Rios, C.; Stegmaier, M.; Hosseini, P.; Wang, D.; Scherer, T.; Wright, C. D.; Bhaskaran, H.; Pernice, W. H. P. *Nature Photonics* **2015**, *9*, 725–732.

[116] Chen, L.; Lu, W.; Lieber, C. M. *Semiconductor Nanowires: From Next-Generation Electronics to Sustainable Energy*; The Royal Society of Chemistry, 2015; pp 1–53.

[117] Voss, T.; Svacha, G. T.; Mazur, E.; Müller, S.; Ronning, C.; Konjhodzic, D.; Marlow, F. *Nano Letters* **2007**, *7*, 3675–3680.

[118] Hsu, C. W.; Zhen, B.; Stone, A. D.; Joannopoulos, J. D.; Soljačić, M. *Nature Reviews Materials* **2016**, *1*, 16048.

[119] Limonov, M. F.; Rybin, M. V.; Poddubny, A. N.; Kivshar, Y. S. *Nature Photonics* **2017**, *11*, 543–554.

[120] Fan, P.; Yu, Z.; Fan, S.; Brongersma, M. L. *Nature Materials* **2014**, *13*, 471–475.

[121] Fedotov, V. A.; Rose, M.; Prosvirnin, S. L.; Papasimakis, N.; Zheludev, N. I. *Physical Review Letters* **2007**, *99*, 147401.

[122] Hsu, C. W.; DeLacy, B. G.; Johnson, S. G.; Joannopoulos, J. D.; Soljačić, M. *Nano Letters* **2014**, *14*, 2783–2788.

[123] Alaee, R.; Lehr, D.; Filter, R.; Lederer, F.; Kley, E. B.; Rockstuhl, C.; Tunnermann, A. *ACS Photonics* **2015**, *2*, 1085–1090.

[124] Miroshnichenko, A. E.; Kivshar, Y. S. *Nano Letters* **2012**, *12*, 6459–6463.

[125] Miroshnichenko, A. E.; Luk'yanchuk, B.; Maier, S. A.; Kivshar, Y. S. *ACS Nano* **2012**, *6*, 837–842.

[126] Liu, N.; Langguth, L.; Weiss, T.; Kastel, J.; Fleischhauer, M.; Pfau, T.; Giessen, H. *Nature Materials* **2009**, *8*, 758–762.

[127] Adato, R.; Artar, A.; Erramilli, S.; Altug, H. *Nano Letters* **2013**, *13*, 2584–2591.

[128] Lassiter, J. B.; Sobhani, H.; Knight, M. W.; Mielczarek, W. S.; Nordlander, P.; Halas, N. J. *Nano Letters* **2012**, *12*, 1058–1062.

[129] Verellen, N.; Sonnefraud, Y.; Sobhani, H.; Hao, F.; Moshchalkov, V. V.; Van Dorpe, P.; Nordlander, P.; Maier, S. A. *Nano Letters* **2009**, *9*, 1663–1667.

[130] Wang, H.; Wu, Y.; Lassiter, B.; Nehl, C. L.; Hafner, J. H.; Nordlander, P.; Halas, N. J. *Proceedings of the National Academy of Sciences of the United States of America* **2006**, *103*, 10856–10860.

[131] Suh, W.; Wang, Z.; Fan, S. *IEEE Journal of Quantum Electronics* **2004**, *40*, 1511–1518.

[132] Lim, S. K.; Crawford, S.; Haberfehlner, G.; Gradečak, S. *Nano Letters* **2013**, *13*, 331–336.

[133] Kim, S.; Hill, D. J.; Pinion, C. W.; Christesen, J. D.; McBride, J. R.; Cahoon, J. F. *ACS Nano* **2017**, *11*, 4453–4462.

[134] Yang, Y.; Kravchenko, I. I.; Briggs, D. P.; Valentine, J. *Nature Communications* **2014**, *5*, 5753.

[135] Fedotov, V. A.; Papasimakis, N.; Plum, E.; Bitzer, A.; Walther, M.; Kuo, P.; Tsai, D. P.; Zheludev, N. I. *Physical Review Letters* **2010**, *104*, 223901.

[136] Soref, R. A.; Bennett, B. R. *IEEE Journal of Quantum Electronics* **1987**, *23*, 123–129.

[137] Xu, Q.; Schmidt, B.; Pradhan, S.; Lipson, M. *Nature* **2005**, *435*, 325–327.

[138] Feigenbaum, E.; Diest, K.; Atwater, H. A. *Nano Letters* **2010**, *10*, 2111–2116.

[139] Ma, Z.; Li, Z.; Liu, K.; Ye, C.; Sorger Volker, J. *Nanophotonics* **2015**, *4*, 198.

[140] Wilson, W. M.; Stewart, J. W.; Mikkelsen, M. H. *Nano Letters* **2018**, *18*, 853–858.

[141] Gramotnev, D. K.; Bozhevolnyi, S. I. *Nature Photonics* **2010**, *4*, 83–91.

[142] Koenderink, A. F.; Alu, A.; Polman, A. *Science* **2015**, *348*, 516–521.

[143] Kodigala, A.; Lepetit, T.; Gu, Q.; Bahari, B.; Fainman, Y.; Kanté, B. *Nature* **2017**, *541*, 196–199.

[144] Ha, S. T.; Fu, Y. H.; Emani, N. K.; Pan, Z.; Bakker, R. M.; Paniagua-Dominguez, R.; Kuznetsov, A. I. *Nature Nanotechnology* **2018**,

[145] Huang, K. C. Y.; Seo, M.-K.; Sarmiento, T.; Huo, Y.; Harris, J. S.; Brongersma, M. L. *Nature Photonics* **2014**, *8*, 244–249.

[146] Sadrieva, Z. F.; Bogdanov, A. A. *Journal of Physics: Conference Series* **2016**, *741*, 12122.

[147] Plotnik, Y.; Peleg, O.; Dreisow, F.; Heinrich, M.; Nolte, S.; Szameit, A.; Segev, M. *Physical Review Letters* **2011**, *107*, 183901.

[148] Weimann, S.; Xu, Y.; Keil, R.; Miroshnichenko, A. E.; Tünnermann, A.; Nolte, S.; Sukhorukov, A. A.; Szameit, A.; Kivshar, Y. S. *Physical Review Letters* **2013**, *111*, 240403.

[149] Hsu, C. W.; Zhen, B.; Lee, J.; Chua, S. L.; Johnson, S. G.; Joannopoulos, J. D.; Soljacic, M. *Nature* **2013**, *499*, 188–191.

[150] Lee, J.; Zhen, B.; Chua, S.-L.; Qiu, W.; Joannopoulos, J. D.; Soljačić, M.; Shapira, O. *Physical Review Letters* **2012**, *109*, 67401.

[151] Bulgakov, E. N.; Sadreev, A. F. *Physical Review A* **2015**, *92*, 23816.

[152] Bulgakov, E. N.; Maksimov, D. N. *Physical Review Letters* **2017**, *118*, 267401.

[153] Bulgakov, E. N.; Sadreev, A. F. *Physical Review A* **2018**, *97*, 63856.

[154] Rybin, M. V.; Koshelev, K. L.; Sadrieva, Z. F.; Samusev, K. B.; Bogdanov, A. A.; Limonov, M. F.; Kivshar, Y. S. *Physical Review Letters* **2017**, *119*, 243901.

[155] Koshelev, K.; Bogdanov, A.; Kivshar, Y. *Science Bulletin (In press)* **2018**,

[156] Belyakov, M. A.; Balezin, M. A.; Sadrieva, Z. F.; Kapitanova, P. V.; Nenasheva, E. A.; Sadreev, A. F.; Bogdanov, A. A. Experimental observation of symmetry protected bound state in the continuum in a chain of dielectric disks. 2018.

[157] Kim, S.; Kim, K. H.; Hill, D. J.; Park, H. G.; Cahoon, J. F. *Nature Communications* **2018**, *9*, 2781.

[158] Fan, S. H.; Joannopoulos, J. D. *Physical Review B* **2002**, *65*, 235112.

[159] Fan, S.; Suh, W.; Joannopoulos, J. D. *Journal of the Optical Society of America A, Optics, Image Science, and Vision* **2003**, *20*, 569–572.

[160] Hamam, R. E.; Karalis, A.; Joannopoulos, J. D.; Soljacic, M. *Physical Review A* **2007**, *75*, 53801.

[161] Ruan, Z.; Fan, S. *The Journal of Physical Chemistry C* **2010**, *114*, 7324–7329.

[162] Ruan, Z.; Fan, S. *Physical Review Letters* **2010**, *105*, 13901.

[163] Sadrieva, Z. F.; Sinev, I. S.; Koshelev, K. L.; Samusev, A.; Iorsh, I. V.; Takayama, O.; Malureanu, R.; Bogdanov, A. A.; Lavrinenko, A. V. *ACS Photonics* **2017**, *4*, 723–727.

[164] Knoedler, M.; Bologna, N.; Schmid, H.; Borg, M.; Moselund, K. E.; Wirths, S.; Rossell, M. D.; Riel, H. *Crystal Growth & Design* **2017**, *17*, 6297–6302.